UNIVERSIDADE ESTADUAL DE CAMPINAS

Faculdade de Engenharia Mecânica

JOSÉ LUIS DÁVILA SÁNCHEZ

Rheological studies and 3D extrusion-based printing of nanocomposite hydrogels

Estudos reológicos e impressão 3D baseada em extrusão de hidrogéis nanocompósitos

CAMPINAS
2018

JOSÉ LUIS DÁVILA SÁNCHEZ

Rheological studies and 3D extrusion-based printing of nanocomposite hydrogels

Estudos reológicos e impressão 3D baseada em extrusão de hidrogéis nanocompósitos

Thesis presented to the School of Mechanical Engineering of the University of Campinas in partial fulfillment of the requirements for the degree of Doctor in Mechanical Engineering in the area of Materials and Fabrication Processes.

Tese apresentada à Faculdade de Engenharia Mecânica da Universidade Estadual de Campinas como parte dos requisitos exigidos para a obtenção do título de Doutor em Engenharia Mecânica, na Área de Materiais e Processos de Fabricação.

Supervisor: Prof. Dr. Marcos Akira d'Ávila

ESTE EXEMPLAR CORRESPONDE À VERSÃO FINAL DA TESE DEFENDIDA PELO ALUNO JOSÉ LUIS DÁVILA SÁNCHEZ, E ORIENTADO PELO PROF. DR. MARCOS AKIRA d'ÁVILA

.....
ASSINATURA DO ORIENTADOR

CAMPINAS
2018

Agência(s) de fomento e nº(s) de processo(s): SENESCYT, AR2Q-8590
ORCID: http://orcid.org/0000-0003-0502-5963

Ficha catalográfica
Universidade Estadual de Campinas
Biblioteca da Área de Engenharia e Arquitetura
Rose Meire da Silva - CRB 8/5974

D289r

Dávila Sánchez, José Luis, 1986-
Rheological studies and 3D extrusion-based printing of nanocomposite hydrogels / José Luis Dávila Sánchez. – Campinas, SP : [s.n.], 2018.

Orientador: Marcos Akira d'Ávila.
Tese (doutorado) – Universidade Estadual de Campinas, Faculdade de Engenharia Mecânica.

1. Reologia. 2. Hidrogel. 3. Impressão tridimensional. 4. Alginato. I. d'Ávila, Marcos Akira, 1972-. II. Universidade Estadual de Campinas. Faculdade de Engenharia Mecânica. III. Título.

Informações para Biblioteca Digital

Título em outro idioma: Estudos reológicos e impressão 3D baseada em extrusão de hidrogéis nanocompósitos
Palavras-chave em inglês:
Rheology
Hydrogel
3D printing
Alginate
Área de concentração: Materiais e Processos de Fabricação
Titulação: Doutor em Engenharia Mecânica
Banca examinadora:
Marcos Akira d'Ávila [Orientador]
Rosário Elida Suman Bretas
Jorge Vicente Lopes da Silva
Maria Helena Andrade Santana
Eliana Aparecida de Rezende Duek
Data de defesa: 13-12-2018
Programa de Pós-Graduação: Engenharia Mecânica

UNIVERSIDADE ESTADUAL DE CAMPINAS

FACULDADE DE ENGENHARIA MECÂNICA

COMISSÃO DE PÓS-GRADUAÇÃO EM ENGENHARIA MECÂNICA

DEPARTAMENTO DE ENGENHARIA DE MANUFATURA E MATERIAIS

TESE DE DOUTORADO

Rheological studies and 3D extrusion-based printing of nanocomposite hydrogels

Estudos reológicos e impressão 3D baseada em extrusão de hidrogéis nanocompósitos

Autor: José Luis Dávila Sánchez
Orientador: Marcos Akira d'Ávila

A Banca Examinadora composta pelos membros abaixo aprovou esta Tese:

Prof. Dr. Marcos Akira d'Ávila
DEMM/FEM/UNICAMP

Profª. Drª. Rosário Elida Suman Bretas
DEMa/UFSCar

Prof. Dr. Jorge Vicente Lopes da Silva
NT3D/CTI

Profª. Drª. Maria Helena Andrade Santana
DEMbio/FEQ/UNICAMP

Profª. Drª. Eliana Aparecida de Rezende Duek
DEMM/FEM/UNICAMP

A ata da defesa com as respectivas assinaturas dos membros encontra-se no processo de vida acadêmica do aluno.

Campinas, 13 de Dezembro de 2018.

Dedication

To my dear parents, Miguel Ángel and María Elena, who taught me never to give up.
To my sisters, Marthy and Silvi, for their love and support at all times.
To my nephews, Gabriel and Daniel, the little men who motivate me to be better every day.
To Bruna, who came to my life with love and happiness,

José Luis

Acknowledgments

I would like to express my sincere gratitude to all the people and institutions who have contributed to the completion of this thesis:

To my parents, Miguel Ángel and María Elena, and to my sisters, Marthy and Silvi, for affection, continuous support, and motivation throughout my life.

To Prof. Dr. Marcos Akira d'Ávila, for the guidance and contributions to this research.

To *Secretaría de Educación Superior, Ciencia, Tecnología e Innovación* (SENESCYT-Ecuador) for the Ph.D. scholarship N°AR2Q-8590.

To *Conselho Nacional de Desenvolvimento Científico e Tecnológico* (CNPq-Brazil) for the financial support from the projects N°401297/2014-4 and N°421745/2016-9.

To *Coordenação de Aperfeiçoamento de Pessoal de Nível Superior* (CAPES-Brazil) and to *Fundo de Apoio ao Ensino, à Pesquisa e Extensão* (FAEPEX-Brazil) for the financial support for the divulgation of this research.

To *Agência de Inovação* INOVA-Unicamp for its support in depositing the patent INPI BR 10 2017 025903 0.

To Prof. Dr. Jorge Vicente Lopes da Silva and Paulo Inforçatti Neto from the Nucleus of Three-Dimensional Technologies (NT3D) of the CTI Renato Archer, I am grateful for all the knowledge that I acquired as a result of our partnership.

To Prof. Dr. Maria Helena Andrade Santana and Carla França, for making available the use of the Zetasizer equipment, the lyophilizer, and the texture analyzer of the *Laboratório de Desenvolvimento de Processos Biotecnológicos*.

To my uncles, aunts, and cousins. Principally, I would like to thank my cousin Marcelo for being like a brother to me.

To Bruna, Mrs. Marimil, and Malu, thanks for the affection and support.

To Carlos Alvarez for his friendship and support at all times.

To my friends and labmates Nicolao, Rosemeire, Gabriel, Eronildo, Ana Flávia, Jéssica, Taís, Geraldine, Vicente, Peterson and Hernandes, for the discussions and their valuable suggestions and criticisms.

To the laboratory technicians Claudenete Vieira Leal and José Luis Lisboa.

πάντα ῥεῖ
"Everything flows"

Heraclitus

"I can do all things through Christ who strengthens me"

Philippians 4:13

Abstract

Hydrogels are natural or synthetic polymeric materials that maintain a three-dimensional structure. They can absorb and retain large amounts of water, making them suitable for several applications. Together with additive manufacturing (AM), the field of applications is broad. Hence, the evaluation of the rheological properties of ink and bio-inks plays an important role in defining their composition and establishing the parameters of the process. In this research, the rheological properties of ink for 3D extrusion-based printing were studied. Initially, alginate aqueous solutions were analyzed. The Cross viscosity model successfully described the steady-state shear behavior of this polysaccharide. Moreover, the scaling behavior was analyzed for the entangled regime and is in good agreement with polyelectrolyte solutions ($G_e \sim c_p^{3/2}$). Next, mixtures Laponite/alginate were analyzed as a case study. Laponite is a synthetic hydrophilic nanosilicate used as a rheology modifier of waterborne solutions. When dispersed in water, it takes the form of disk-like particles with negative charges in the faces and positive in the rims if the $pH \leq 11$. Then, electrostatic interactions between Laponite and the anionic alginate significantly influence the rheological behavior. Higher alginate concentrations hindered the rheology modifier effect of Laponite. Soft physical gels were obtained at low alginate concentrations. After that, the printability was evaluated in a second case study and a suitable concentration for 3D printing defined. A strong shear-thinning behavior described by the Ostwald-de Waele power-law model was obtained for higher Laponite concentrations. The viscosity recovery test demonstrated an instantaneous structure recovery, which did not present shear rate dependence. Amplitude and frequency sweep tests demonstrated that the optimal ink behaves as a solid-like. 3D printing tests were performed in a piston-driven system that was developed to be compatible with open source 3D printers. The optimal ink was successfully dispensed, and 3D printed gels were crosslinked to obtain single (SN) and double network (DN) hydrogels through ionic and ionic-covalent crosslinking, respectively. The set of characterizations performed constitutes a protocol that can be applied to evaluate the printability of inks and bio-inks.

Keywords: Rheology, hydrogel, 3D printing, alginate, Laponite.

Resumo

Hidrogéis são materiais poliméricos naturais ou sintéticos que mantêm uma estrutura tridimensional. Eles podem absorver e reter grandes quantidades de água, tornando-os adequados para uma grande variedade de aplicações. Aliado aos processos de manufatura aditiva, o campo de aplicações é amplo. Assim, a avaliação das propriedades reológicas de tintas e biotintas desempenha um papel importante para definir sua composição e estabelecer os parâmetros do processo. Nesta pesquisa, elas foram estudadas para impressão 3D baseada em extrusão. Inicialmente, soluções aquosas de alginato foram analisadas. O modelo de viscosidade de Cross descreveu adequadamente o comportamento de cisalhamento no estado estacionário deste polissacarídeo. Além disso, os resultados obtidos estão em concordância com o comportamento de soluções de polieletrólitos ($G_e \sim c_p^{3/2}$). Em seguida, as misturas Laponite/alginato foram analisadas como um estudo de caso. Laponite é um nanosilicato hidrofílico sintético usado como um modificador reológico de soluções à base de água. Quando disperso em água, assume a forma nanodiscos com cargas negativas nas faces e positivas nas bordas se o $pH \leq 11$. Portanto, interações eletrostáticas entre o Laponite e o alginato aniônico influenciam significativamente o comportamento reológico. Concentrações mais elevadas de alginato impediram o efeito modificador de reologia do Laponite. Géis reticulados fisicamente foram obtidos em baixas concentrações de alginato. Seguidamente, em um segundo estudo de caso, foi avaliada a capacidade de impressão e definida a concentração adequada. Um comportamento pseudoplástico descrito pelo modelo de lei das potências de Ostwald-de Waele foi obtido para as maiores concentrações de Laponite. O teste de recuperação da viscosidade demonstrou recuperação instantânea da estrutura, que não apresentou dependência da taxa de cisalhamento. Testes de varredura da amplitude e da frequência demonstraram que a tinta ótima tem um comportamento *solid-like*. Os testes de impressão 3D foram realizados em um sistema acionado por pistão, que foi desenvolvido para ser compatível com impressoras 3D de projeto aberto. A tinta ótima foi depositada com sucesso. Os géis impressos em 3D foram reticulados para obter hidrogéis de rede simples (SN) e dupla (DN) através de reticulação iônica e iônica-covalente respectivamente. O conjunto de caracterizações realizadas constitui um protocolo para avaliar a capacidade de impressão de tintas e biotintas.

Palavras-chave: Reologia, hidrogel, impressão 3D, alginato, Laponite.

Illustrations List

Table List

List of Symbols, Acronyms and Abbreviations

Mathematical symbols, variables and parameters

a	Transition parameter
a_x	Horizontal shift factor
a_y	Vertical shift factor
c_L	Laponite concentration
c_p	Polymer concentration
d	Nominal diameter of the threaded shaft
d_m	Mean diameter of the threaded shaft
F	Load force
G_e	Plateau modulus
G'	Storage modulus
G''	Loss modulus
$G(t)$	Relaxation modulus
I_{MAX}	Current limit
k_2	Rate constant of sorption
L_T	Thread lead
L	Nozzle tip length
m	Consistency index
m_d	Mass of the dry sample
m_s	Mass of the swollen sample
M_v	Viscosity-average molar mass
n	Power-law index
n_s	Number of thread starts
p	Thread pitch
Q	Flow rate
Q_e	Swelling ratio at the equilibrium
Q_t	Swelling ratio
R	Nozzle tip radius
R_{CS}	Current sense resistance
r_0	Initial rate of swelling

S	Gel strength
t	Time
T_R	Raising torque
t_w	Waiting time
$\underline{v}$	Vector velocity
v_e	Extrusion speed
v_p	Printing speed
v_{ps}	Piston speed
V_{REF}	Reference voltage
v_z	z-Velocity
$wt.\%$	Percentage by weight
$\%wt./vol$	Weight/volume percentage
α, K	Mark-Houwink-Sakurada parameters
α_F	Flank angle
α_m	Normalized flank angle
β	Thread geometry parameter
γ	Strain
γ_{LVE}	Strain amplitude for the LVE range
γ_0	Constant strain amplitude for SAOS
$\Gamma()$	Gamma function
$\dot{\gamma}$	Shear rate
$\dot{\gamma}_c$	Critical shear rate
$\dot{\gamma}_0$	Constant amplitude of the shear rate for SAOS
$\dot{\gamma}_w$	Wall shear rate
$tan(\delta)$	Damping factor
Δp	Pressure difference
η	Viscosity
$[\eta]$	Intrinsic viscosity
η_p	Printing viscosity
η_{sp}	Specific viscosity
η_{red}	Reduced viscosity
η_0	Zero-shear viscosity
η_∞	Infinite shear viscosity
η_s	Solvent viscosity
η_{rec}	Viscosity recovery percentage
$\eta_{t_{rec}}$	Viscosity at a recovery time t
η_i	Initial viscosity (rest interval)
λ	Relaxation time

λ_L	Lead angle
μ_t	Coefficient of thread friction
ω	Angular frequency
ω_x	Crossover angular frequency
τ	Shear stress
τ_0	Constant stress amplitude for SAOS
τ_f	Flow point
τ_y	Yield shear stress

Acronyms and Abbreviations

3D	Three-dimensional
AAm	Acrylamide
AM	Additive manufacturing
ANOVA	Analysis of variance
ASTM	American society for testing and materials
ATR	Attenuated total reflectance
$CaCl_2$	Calcium chloride
CAD	Computer-aided design
CNC	Nanocellulose crystals
CNF	Nanocellulose fibers
DN	Double network
ECM	Extracellular matrix
FDA	Food and drug administration
FDM	Fused deposition modeling
HA	Hyaluronic acid
INPI	National institute of industrial property
ISO	International organization for standardization
FTIR	Fourier transform infrared spectroscopy
G	α-L-guluronate
LVE	Linear viscoelasticity
M	$(1-4)$-linked β-D-mannuronate
MBAA	N,N'-methylenebisacrylamide
MRD	Mean relative deviation
$NaCl$	Sodium chloride

PAAm	Polyacrylamide
PEG	Polyethylene glycol
pH	Potential of hydrogen
RAMPS	RepRap arduino mega pololu shield
SAOS	Small amplitude oscillatory shear
SN	Single network
TE	Tissue engineering
TEMED	N,N,N',N' tetramethylethylendiamine
UV	Ultraviolet

CONTENTS

1 INTRODUCTION

In the introductory chapter, is presented a general overview of the rheological properties of hydrogels, mainly oriented to applications through additive manufacturing. Subsequently, the objectives of this research were defined. Finally, the thesis outline is shown to depict the research scope.

1.1 Overview of the rheological properties associated with the additive manufacturing (AM) of hydrogels

Hydrogels are natural or synthetic polymeric materials that maintain a three-dimensional structure. They can absorb and retain large quantities of water due to hydrophilic groups in the polymer chains (Barbucci, 2009; Gulrez *et al.*, 2011). Hydrogels have been extensively studied for biomedical applications, drug delivery, separation technology, biosensors, agriculture, contact lenses, food packaging, cosmetics, enhanced oil recovery, among others (Ullah *et al.*, 2015).

Together with additive manufacturing (AM) processes, hydrogels are attractive for biofabrication and biomedical applications. The 3D printing by robotic dispensing is commonly used to deposit inks or bio-inks in layers to obtain a 3D object. A variation of this AM technique is the 3D extrusion-based process, where the material flow is generated by a pneumatic system, a piston or a screw. The limitations of the process are mainly related to the properties of the material being printed (Highley *et al.*, 2015). Concretely, the rheological properties are of relevance and have a fundamental role to obtain a good resolution and printing fidelity (Malda *et al.*, 2013).

Different approaches have been used to print soft materials like hydrogels. They can be tailored to overcome the associated limitations. A soft material must have a gel-like behavior or must be gelled/crosslinked in situ during the 3D printing process to prevent its collapse due to its own weight (Hinton *et al.*, 2015; Highley *et al.*, 2015). In the 3D extrusion-based process, the material is extruded through nozzle tips. During extrusion, filaments should be formed instead

of drops (Schuurman *et al.*, 2013). Consequently, the viscosity of the material is a fundamental property for the process.

Low viscosity enables efficiently dispensing the material through the nozzle tip. Nevertheless, once deposited, the material spreads and collapses. On the other hand, with high viscosity, the material can retain its shape, which makes it difficult to dispense, requiring higher pressures. Hence, the shear-thinning behavior is attractive for this kind of application (Guvendiren *et al.*, 2012; Schmieg *et al.*, 2018). High viscosity is desirable at low shear rates and low viscosity at high shear rates. The latter is generated in the walls of the nozzle tips. Therefore, low viscosity will lead to the easy deposition of the material. Subsequently, viscosity recovery will generate the capability to retain the shape, taking into account that the deposited material should maintain its structural integrity over the lifetime of the printed object (Ouyang *et al.*, 2016; Echalier *et al.*, 2017).

During the 3D printing process, flow initiation also plays an essential role (Paxton *et al.*, 2017). The yield stress defines it; a printable material should behave as solid-like under the yield point and as liquid-like above it. Concentrated polymer samples commonly exhibit yield stress due to their chains interactions. When a shear load is applied, the chains tend to align, and the material flows. Contrariwise, the material experiences a recovery when the shear load is removed. This recovery is also associated with a thixotropic behavior, through which the structure can be recovered several times after a shear load application (Bretas & d'Ávila, 2005). Thixotropy constitutes an attractive behavior for 3D printing, taking into account that the material is submitted to shear load conditions during the process.

Different hydrogel systems have been studied to enhance rheological properties. Rheology modifiers, such as ethylene glycol, nanosilicates, nanocellulose crystals (CNC), nanocellulose fibers (CNF), among others, tailor the viscosity profile and other rheological properties for 3D printing (Bakarich *et al.*, 2013; Peak *et al.*, 2017; Shin *et al.*, 2017; Siqueira *et al.*, 2017). Moreover, other approaches include pre-crosslinked hydrogels, UV crosslinking between layers, thermoreversible crosslinking, and thermoreversible support baths (Chung *et al.*, 2013; He *et al.*, 2016; Hinton *et al.*, 2015; Yang *et al.*, 2017).

As established, the evaluation of the rheological properties of inks and bio-inks is crucial to defining their compositions and to setting the parameters of the process. However, according to Malda *et al.* (2013), the importance of rheology in this field is commonly underestimated. As observed in different research studies, printability is usually analyzed only as a function of viscosity, where a shear-thinning behavior is desirable. Therefore, a clear correlation between the rheological properties and the process is lacking. Taking into account that printability depends on a set of properties, this research proposes to apply different rheological characterizations as a tool to obtain inks with suitable properties from their conception to their use in 3D extrusion-based printing.

1.2 Objectives

After identifying the scenario in which the 3D printing of hydrogels is being carried out, this research focuses on developing appropriated protocols to evaluate the printability of inks. Hence, associating the rheological properties involved in each stage of the process will allow obtaining optimal ink formulations for 3D extrusion-based printing, where crosslinking methods may be applied after printing to obtain hydrogels. Specifically, this thesis proposes the following objectives:

1.2.1 General objective

Establish a methodology to evaluate the printability of inks through rheological studies and to develop a dispositive to print them using the 3D extrusion-based process to obtain nanocomposite hydrogels subsequently.

1.2.2 Specific objectives

- Analyze the rheological behavior of sodium alginate solutions and mixtures, including the nanosilicate Laponite XLG as a rheology modifier.

- Evaluate the interactions between the Laponite disk-like particles and the alginate chains, and examine how their concentrations influence their shear-thinning and the solid-like/liquid-like behaviors.
- Establish a methodology to test inks, in which each stage of the 3D extrusion-based process is related to the rheological behavior of the ink.
- Validate the methods defined by obtaining and testing an optimal printable ink.
- Develop and test a modular 3D extrusion-based printing head compatible with open source (firmware/hardware/software) 3D printers.
- Crosslink the deposited ink after printing by ionic and ionic-covalent bonds and characterize the obtained single (SN) and double network (DN) hydrogels.

1.3 Outline of the thesis

This thesis is structured in five chapters. Initially, **Chapter 1**, showed a general introduction to hydrogels, their applications, and the limitations of their use for 3D printing through the extrusion-based process. **Chapter 2** exposed a literature review deepening the details of the additive manufacturing process and the rheological properties associated. Moreover, **Chapter 2** presented the fundamentals of hydrogels and crosslinking mechanisms. Details of the materials used throughout this work are also shown. **Chapter 3** presented a rheological study of the system Laponite/alginate, in which the physical gelation and the aging evolution were analyzed. **Chapter 4** explained the rheological evaluation of Laponite/alginate inks to define the methodology to investigate their printability. Jointly, the details of the development of a modular printing head are described. Then, printing tests were performed. Ionic and ionic-covalent crosslinking were carried out to obtain single (SN) and double network (DN) hydrogels. Finally, the general conclusion of this research is shown in **Chapter 5**. Figure 1 illustrates the thesis outline.

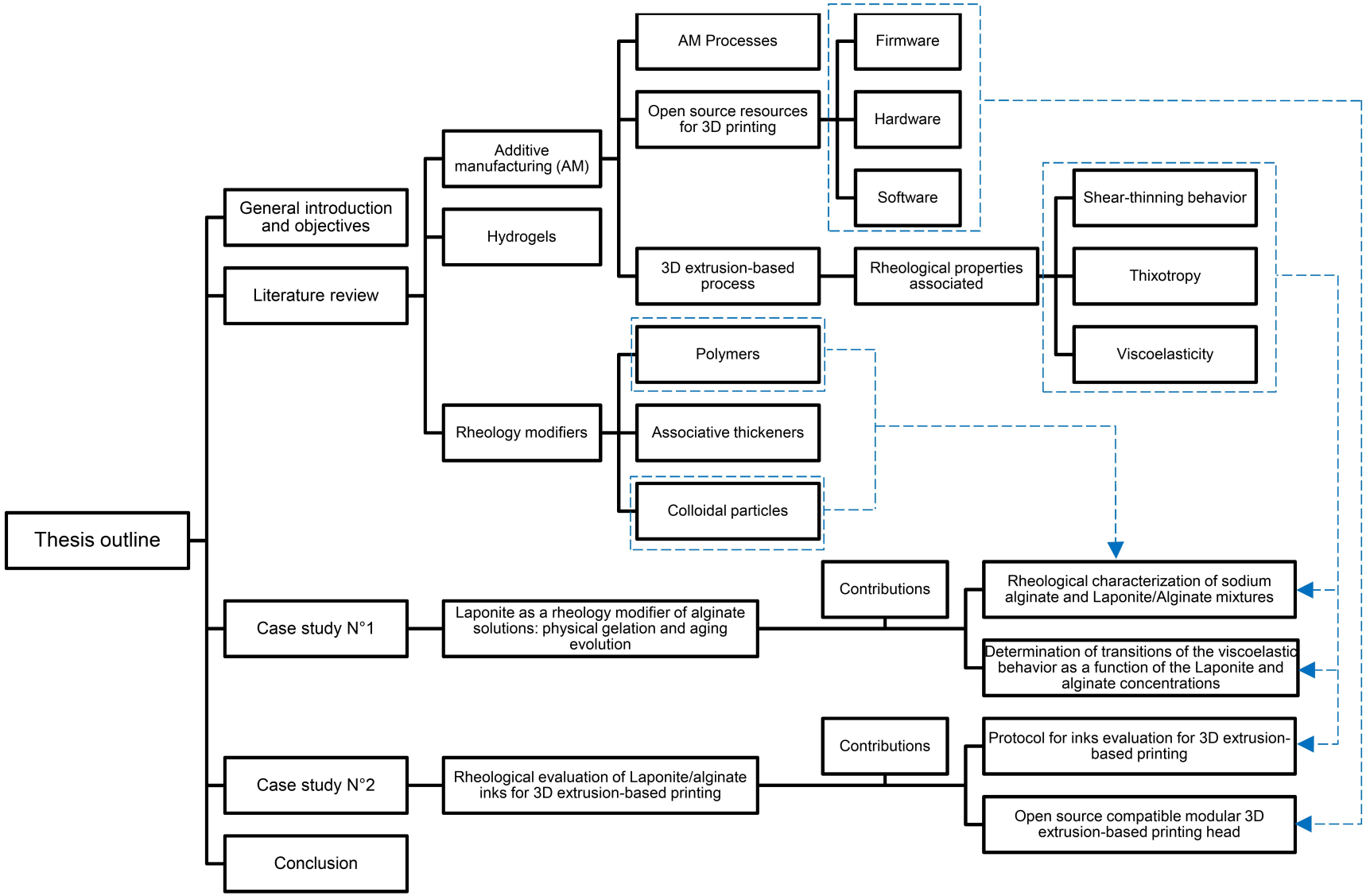

Fig. 1.1: Pictorial diagram of the thesis outline.

2 LITERATURE REVIEW

This chapter presents the additive manufacturing processes. The 3D extrusion-based process and the rheological properties associated are mainly addressed. Furthermore, the fundamentals of hydrogels and the crosslinking mechanisms are described. Finally, the polymers used in this work and the rheology modifier (Laponite XLG) are presented in more detail.

2.1 Additive manufacturing (AM)

Additive manufacturing, frequently denominated 3D printing is defined as the set of processes of joining materials to make objects from 3D model data, layer upon layer. The standardized AM process categories are presented in Fig. 2.1 (ISO/ASTM 52900, 2015; Conner *et al.*, 2014).

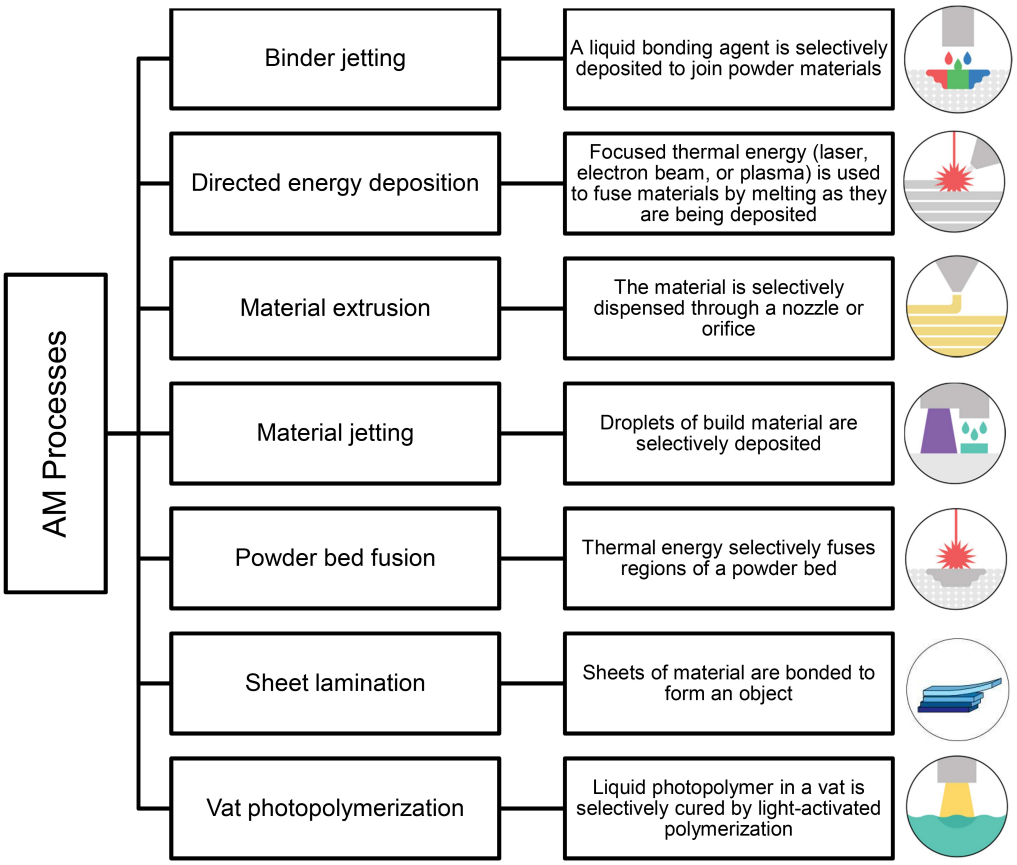

Fig. 2.1: AM process categories.
AM illustrations were obtained from https://www.3dhubs.com.

These processes allow fabricating complex objects with different types of materials. In the case of biomaterials, AM has been widely used to obtain biomedical devices, substitutes, and scaffolds for tissue engineering (Chia & Wu, 2015). Open source projects as RepRap and Fab@Home have been made possible to expand the applications in this field, mainly through material extrusion processes. The RepRap 3D printer, observed in Fig. 2.2a, arises as a self-replicating machine that uses Fused Deposition Modeling (FDM) (Mueller, 2012). On the other hand, the Fab@Home 3D printer was initially developed to print cold-cure materials (Malone & Lipson, 2007). Taking into account that these projects are hardware and firmware open source, they have been modified over time. The modifications are generally focused on the 3D printing head, where the design mainly depends on features as the material, its form, its properties, among others. Fig. 2.2b shows the evolution of the RepRap project; the 3DCloner Lab printer was the RepRap-based printer used in this research. Furthermore, it is proper to highlight that these 3D printers and its components are low-cost systems.

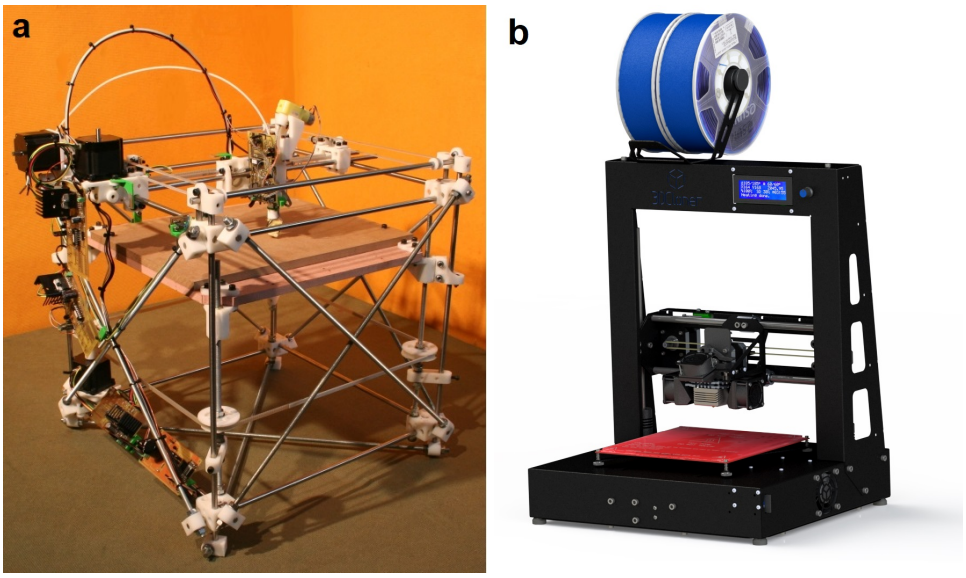

Fig. 2.2: (a) First version of the project RepRap; Darwin model and (b) the RepRap-based 3D printer 3DCloner Lab. The photos a and b were obtained from (Malone & Lipson, 2007) and http://3dcloner.ind.br respectively.

The firmware is a program embedded on the motherboard of a 3D printer. Marlin is a recent open source firmware to control 3D printers. It was created in 2011 and has some advantages as the efficient movements of the extruder, which results in a higher precision for the material deposition. Moreover, it allows a better temperature control for the extruder and the heatbed (Evans, 2012). Since the RepRap project was released, many people around the world have worked to improve the firmware, hardware, and software.

The control system of a 3D printer is composed of two parts: (i) the firmware, which is used to send the signals to the components of the 3D printer and (ii) the software, which is a program installed in a computer (Wijnen *et al.*, 2016). This latter sends the instructions (g-code) to the firmware. The g-code is a file containing the operations and the printing path; it can be generated by a slicing software or a path generator. In Fig. 2.3 is observed a pictorial scheme of the software-firmware-hardware interaction and some examples of these elements. As observed, there is an extensive quantity of tools for 3D printing available. Hence, the process can be adapted according to the application.

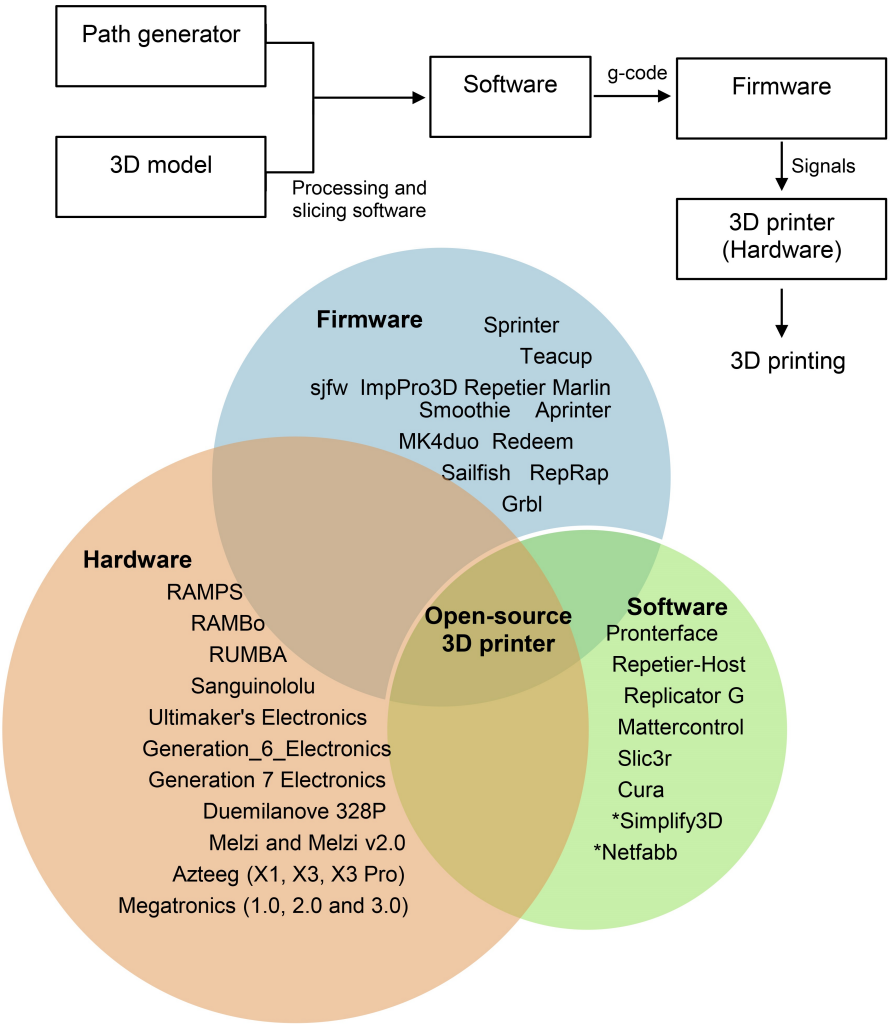

Fig. 2.3: Current electronics, firmware, and software for open-source 3D printers.
(*This software requires a commercial license.) Sources: https://reprap.org and (Wijnen *et al.*, 2016)

The most common electronics of a 3D printer usually combines an Arduino MEGA 2650 and the RepRap shield denominated RAMPS (RepRap Arduino Mega Pololu Shield). The RAMPS shield is plugged on the top of the Arduino microcontroller. This shield is specifi-

cally designed for 3D robotic systems and allows switching up to five stepper motors, three thermistors, and six end-stop connections. It has three high-power switched loads fused at $5\ A$ and $11\ A$ for the extruders and the printing platform (heatbed). Moreover, a Pololu stepper driver is frequently used to control each stepper motor (Evans, 2012). In Fig. 2.4 is illustrated a 3D printer electronics scheme. The stepper motors are used to generate the movement in the X, Y, Z axes and to deposit the material from the extruder. It is necessary at least one end-stop by axis to define the homing position of the 3D printer. The thermistors are used to sense the temperature of the extruder and the heatbed.

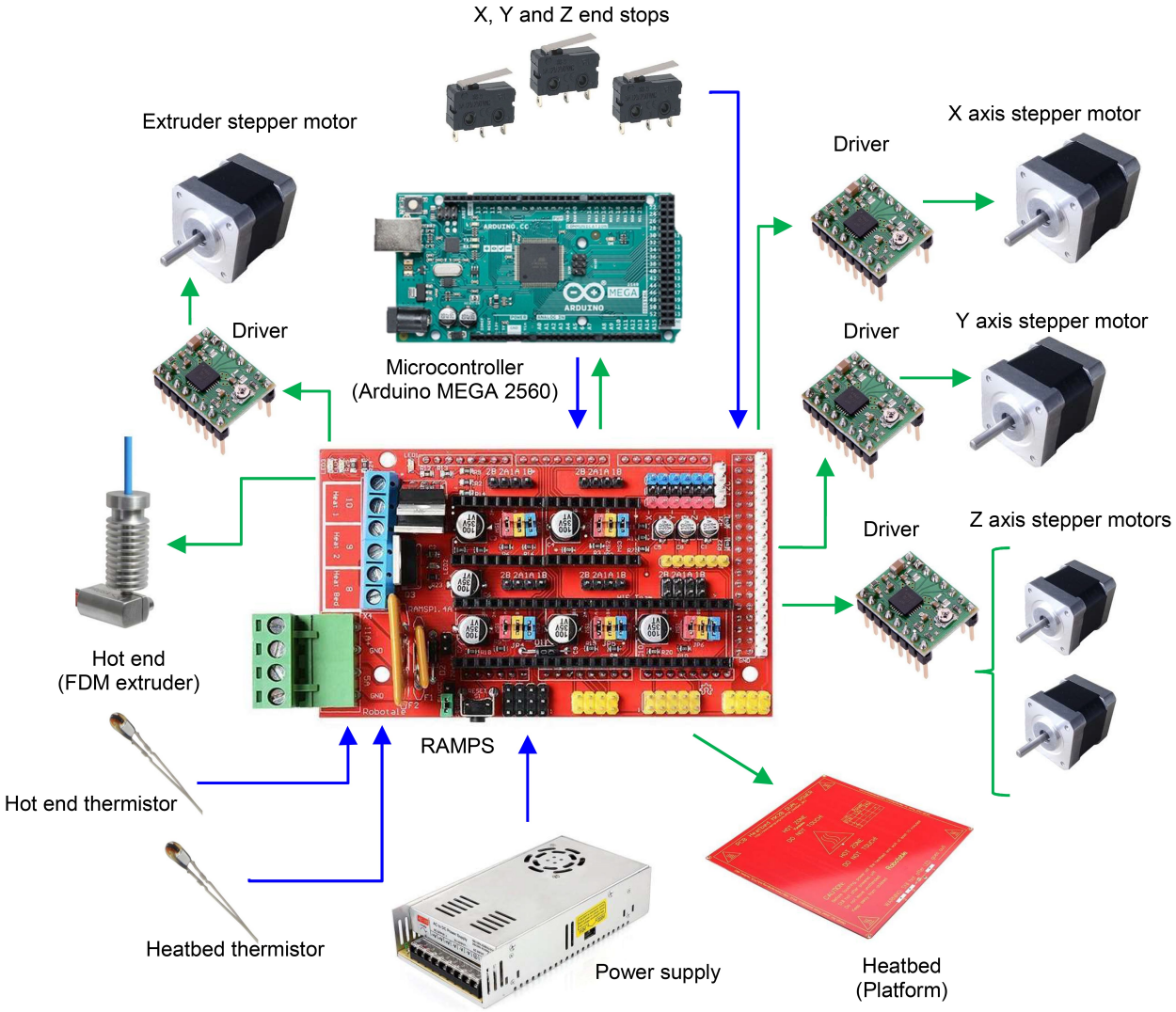

Fig. 2.4: 3D printer electronics map - Arduino/RAMPS.

The Polulu stepper driver A4988 observed in Fig. 2.4 can be configured to define the step and microstep size. Higher resolutions can be obtained allowing intermediate steps, which can

be achieved by energizing the coils of the motor with intermediate current levels. The RAMPS shield has three resolution selector inputs: MS1, MS2, and MS3. The MS1 and MS3 have $100\ k\Omega$ pull-down resistors and the MS2 a $50\ k\Omega$ pull-down resistor. The full step mode is obtained leaving disconnected the three selector inputs. In Table 2.1 are shown the configurations of the selector inputs to obtain different microstepping resolutions.

Table. 2.1: Step and microstep configuration for the A4988 stepper driver.

MS1	**MS2**	**MS3**	**Microstep resolution**
Low	Low	Low	Full step
High	Low	Low	Half step
Low	High	Low	Quarter step
High	High	Low	Eighth step
High	High	High	Sixteenth step

Low (disconnected selector); High (connected selector)
Source: https://www.pololu.com

The current limit of the stepper driver should be correctly defined to avoid the skip of microsteps. For the A4988 driver, the current limit can be calculated by

$$I_{MAX} = \frac{V_{REF}}{8R_{CS}} \tag{2.1}$$

where V_{REF} is the reference voltage and R_{CS} the current sense resistance of the driver. The current limit can be set using the trimmer potentiometer of the driver. The full step mode should be used, and the current through one of the motor coils measured by plugging the ammeter in series with one of the motor wires. Pulses should not be sent to the stepper motor during the measurement. When the motor is standby, the board reduces the current to 70%. Hence, the measured current will be 70% of the desired limit. This fact should be taken into account to do not exceed the current limit of the stepper motor. For microstepping modes, it is not necessary to limit the current (Allegro, 2018).

Recent researches are focused in the 3D printing of inks and bio-inks through material extrusion processes, which are compatible with a wide range of materials, including biocompa-

tible polymers, gels, cell-laden spheroids, and cell-laden hydrogels (Habib *et al.*, 2018; Murphy *et al.*, 2018). Inks 3D printing based on the deposition of colloidal, nanoparticle or organic-based materials. The direct-write assembly technique includes the droplet jetting and the filament writing (Lewis & Gratson, 2004; Barry *et al.*, 2009). This latter is well known as 3D extrusion-based process (Highley *et al.*, 2015; Bakarich *et al.*, 2013; Kirchmajer *et al.*, 2015), which according to the standardized terminology for AM is included in the material extrusion category (ISO/ASTM 52900, 2015).

The 3D extrusion-based process variations are illustrated in Fig. 2.5. As shown, the material is selectively dispensed from a reservoir (generally a syringe), where the flow is controlled by a pneumatic system, a piston or a screw. The material flows through a nozzle tip and should form a continuous filament, jointly, a 3D robotic system controls the deposition path. In pneumatic systems, there is a compressed gas volume delay. Contrariwise, piston-driven systems allow direct control over the material flow. Screw systems are commonly used to dispense highly viscous materials (Malda *et al.*, 2013).

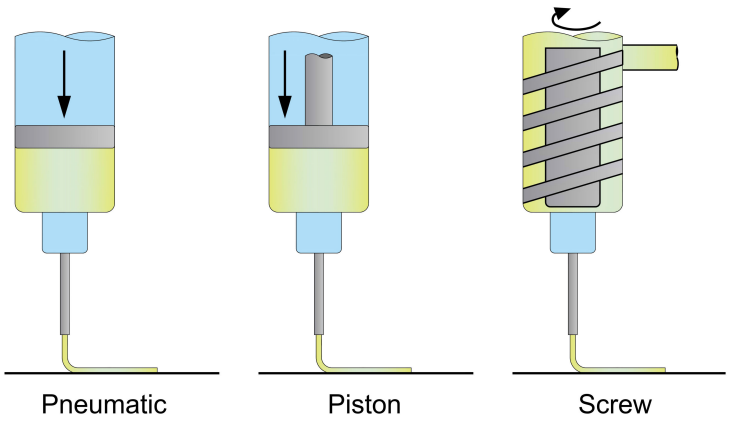

Fig. 2.5: Graphical illustration of the dispensing systems for 3D extrusion-based printing.

The rheological properties are fundamental to develop inks with suitable characteristics for 3D printing. As illustrated in Fig. 2.6, and proposed in this thesis, the rheological behavior can be analyzed in three stages:

- (i) Before printing - rest and flow initiation.
- (ii) During printing - high shear rate in the nozzle tip walls.

- (iii) After printing - viscosity recovery.

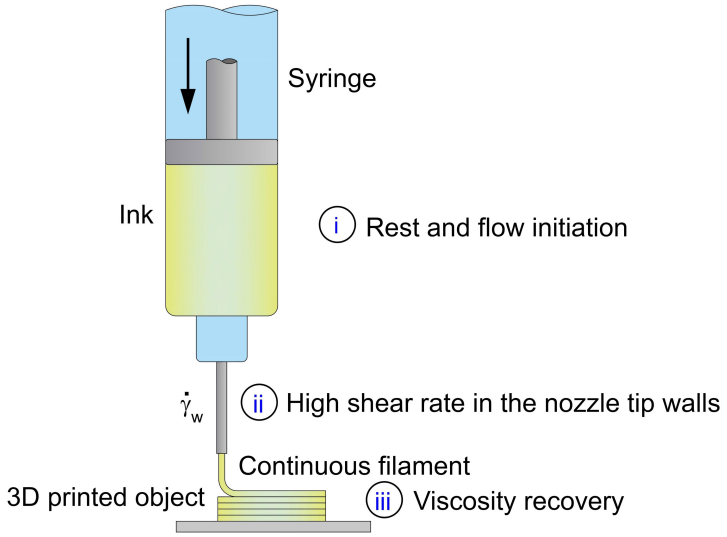

Fig. 2.6: Graphical illustration of the 3D extrusion-based process stages ($\dot{\gamma}_w$-wall shear rate).

The fundamentals of the required rheological behaviors for each stage of the process are presented in greater detail in the next section.

2.2 Rheological behavior

2.2.1 Shear-thinning behavior

The shear-thinning behavior is a nonlinear phenomenon that commonly occurs in polymer melts, in concentrated polymer solutions, and in colloidal dispersions. As illustrated in Fig. 2.7, a dramatic viscosity decrease takes place as a result of a shear load increase (shear rate or shear stress). This phenomenon can be explained at a molecular level. During the shear process, the molecules are more or less oriented in the shear direction. Therefore, the resistance to flow decreases when the orientation is more significant. Polymers are macromolecules; when they are at rest, their chains are entangled (Bretas & d'Ávila, 2005). The shear load application disentangles the polymer chains, and at a high degree of orientation, the macromolecules are no longer in touch with each other. For colloidal dispersions, the shear load causes particles orientation in the flow direction. Moreover, a shear load can also disintegrate agglomerates or

change the particles form. These scenarios also result in less resistance to flow (Macosko, 1994; Mezger, 2006).

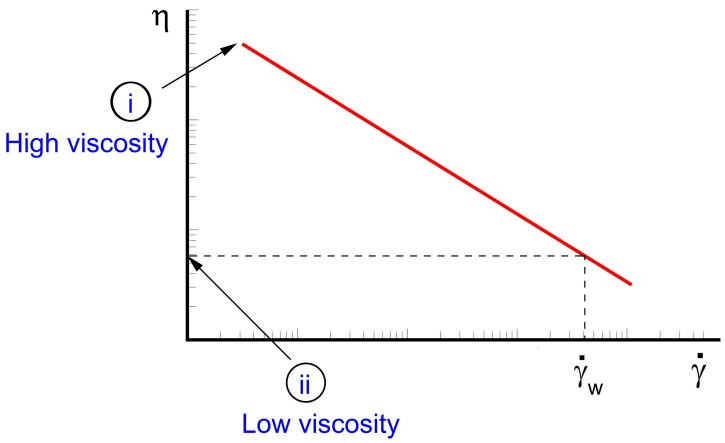

Fig. 2.7: Power-law-like viscosity curve showing a shear-thinning behavior (η-viscosity, $\dot{\gamma}$-shear rate and $\dot{\gamma}_w$-wall shear rate. The Roman numerals represent the stages of the 3D extrusion-based process: (i) rest and flow initiation and (ii) high shear rate in the nozzle tip walls).

In Table 2.2 different mathematical models widely used to describe viscosity curves showing a shear-thinning behavior are presented. For the 3D extrusion-based process, fluids that behave as described by the Ostwald-de Waele model are desirable; this power-law-like model is associated with a strong shear-thinning behavior that allows an easy deposition of the material.

Table. 2.2: Mathematical models for viscosity curves fitting.

Model	Equation	Reference	Parameters
Ostwald-de Waele	$\eta(\dot{\gamma}) = m\dot{\gamma}^{n-1}$	(Mezger, 2006)	m consistency index n power-law index
Carreau	$\frac{\eta(\dot{\gamma})-\eta_\infty}{\eta_0-\eta_\infty} = \left[1+(\lambda\dot{\gamma})^2\right]^{\frac{n-1}{2}}$	(Carreau, 1972)	η_0 zero-shear viscosity η_∞ infinite shear viscosity
Carreau-Yasuda	$\frac{\eta(\dot{\gamma})-\eta_\infty}{\eta_0-\eta_\infty} = \left[1+(\lambda\dot{\gamma})^a\right]^{\frac{n-1}{a}}$	(Yasuda *et al.*, 1981)	($\eta_\infty = 0$, simplified model) λ time constant of the fluid
Cross	$\frac{\eta(\dot{\gamma})-\eta_\infty}{\eta_0-\eta_\infty} = 1+(\lambda\dot{\gamma})^{-n}$	(Cross, 1965)	a transition parameter[1]

[1]Defines the curvature of the transition from a zero shear rate plateau to the power-law-like region.

2.2.2 Thixotropic behavior

The viscosity of a shear-thinning fluid may decrease as a function of the time when a shear load is applied. Hence, an equilibrium viscosity is reached. When the shear load is removed, the material viscosity increases also as a function of the time. This viscosity increase occurs as a result of the molecules and/or particles reorganization. This phenomenon is known as thixotropic behavior. A fluid is considered thixotropic if the initial structural strength is completely recovered. Contrariwise, when an incomplete recovery occurs, even after longs periods at rest, the appropriated term is partial regeneration, which is usually expressed as the ratio between the final and initial viscosities (Mezger, 2006; Dullaert & Mewis, 2005). In Fig. 2.8 it is observed the typical response of a thixotropic material submitted to the step test with three intervals. In the first interval, a very low shear rate is applied to simulate the behavior at rest. Then, in the second interval, a high shear load is suddenly applied to simulate the structural breakdown of the sample. In the case of the 3D extrusion-based process, this interval is related to the high shear rate produced in the nozzle tip walls. Next, in the third interval, the low shear rate is applied again by a higher period o time. In this latter, it is simulated the structural recovery at rest (Özkan *et al.*, 2017).

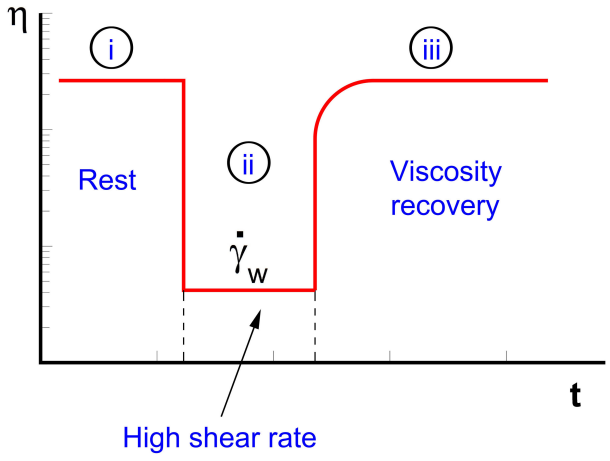

Fig. 2.8: Viscosity recovery test (η-viscosity, $\dot{\gamma}_w$-wall shear rate and t-time. The Roman numerals represent the stages of the 3D extrusion-based process: (i) rest and flow initiation, (ii) high shear rate in the nozzle tip walls and (iii) viscosity recovery).

2.2.3 Viscoelastic character

Oscillatory tests are useful to define the viscoelastic character of a soft material. The elastic behavior is associated with the storage modulus (G') and the viscous behavior with the loss modulus (G''). These material functions can be analyzed through amplitude and frequency sweep tests. In the amplitude sweep test, illustrated in Fig. 2.9, the angular frequency remains constant while the strain or stress amplitude increases as a function of the time. The strain and stress sweeps are defined as follows:

$$\gamma\left(t\right) = \gamma_A sin\left(\omega t\right) \tag{2.2a}$$

$$\tau\left(t\right) = \tau_A sin\left(\omega t\right) \tag{2.2b}$$

where γ and τ are the strain and stress respectively. The subscript "A" represents the amplitude, ω is the angular frequency and t the time.

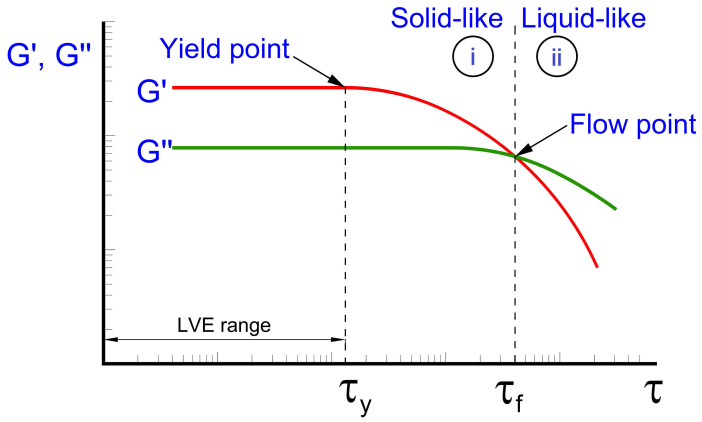

Fig. 2.9: Stress amplitude sweep plot illustrating the linear viscoelasticity range (LVE), the yield stress (τ_y) and the transition from the solid-like to the liquid-like behavior, which takes place at the flow point (τ_f). The Roman numerals represent the stages of the 3D extrusion-based process: (i) rest and flow initiation and (ii) high shear rate in the nozzle tip walls).

With the amplitude sweep test can be defined the linear viscoelasticity range (LVE), the yield stress (τ_y) and the flow point (τ_f). Within the LVE range $G'(\gamma)$ and $G''(\gamma)$ exhibit a constant plateau. The LVE range defines the region where the material can be tested without

destroying its structure. The limiting value of the LVE range is defined as the yield stress. Below this point, no significant structural changes are generated. The flow point can be obtained for a dominated solid character ($G' > G''$), which is better known as solid-like behavior. This crossover ($G' = G''$) defines the transition to the liquid dominated character or liquid-like behavior ($G'' > G'$).

The solid-like behavior is desirable before the flow initiation and after printing. The viscoelastic behavior can be analyzed through frequency sweep tests, specifically with the Small-Amplitude Oscillatory Shear (SAOS) test, which should be performed within the LVE range. As illustrated in Fig. 2.10, the flow is generated under shear conditions.

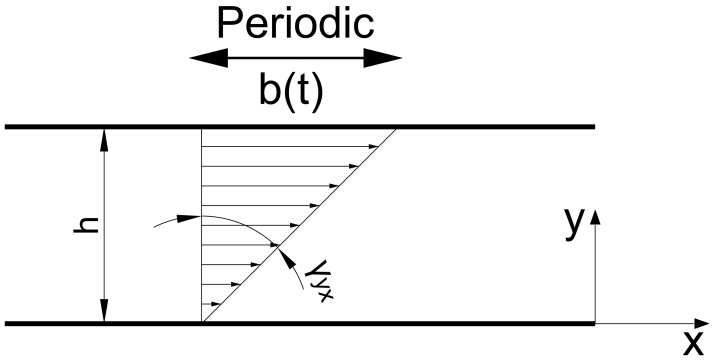

Fig. 2.10: Scheme of the oscillatory shear using parallel plates.
Source: based on Morrison (2001).

The shear rate is time-dependent ($\dot{\gamma}(t)$) and periodic. The kinematics for SAOS is defined as follows:

$$\underline{v} = \begin{pmatrix} \dot{\gamma}(t)y \\ 0 \\ 0 \end{pmatrix}_{xyz} \tag{2.3}$$

where $\underline{v}$ is the vector velocity and

$$\dot{\gamma}(t) = \dot{\gamma}_0 \, cos \, \omega t, \tag{2.4}$$

$\dot{\gamma}_0$ is the constant amplitude of the shear rate, and ω is the angular frequency. As shown in the scheme of Fig. 2.10, the displacement of the upper plate is time-dependent. Then, for small strains:

$$\gamma_{yx}(0,t) = \frac{b(t)}{h}, \tag{2.5}$$

and for a general shear flow:

$$\gamma_{yx}(0,t) = \int_0^t \dot{\gamma}_{yx}(t')dt' \tag{2.6a}$$

$$\gamma_{yx}(0,t) = \frac{\dot{\gamma}_0}{\omega}\, sin\, \omega t \tag{2.6b}$$

$$\gamma_{yx}(0,t) = \gamma_0\, sin\, \omega t \tag{2.6c}$$

Therefore, the motion of the upper plate is also a sine function, given by

$$b(t) = h\gamma_0\, sin\, \omega t, \tag{2.7}$$

where h is the gap between the parallel plates and γ_0 is the constant strain amplitude.

A linear velocity profile will be produced only for sufficiently low frequencies or high viscosities. In this scenario, the shear stress produced will be a sine wave of the same frequency as the input strain wave. Nonetheless, the shear stress is out of phase. The phase difference is represented by δ, and the shear stress is given by (Morrison, 2001)

$$-\tau_{yx}(t) = \tau_0\, sin(\omega t + \delta) \tag{2.8a}$$

$$-\tau_{yx}(t) = \tau_0(sin\, \omega t\, cos\, \delta + sin\, \delta\, cos\, \omega t) \tag{2.8b}$$

$$-\tau_{yx}(t) = (\tau_0\, cos\delta)\, sin\, \omega t + (\tau_0\, sin\delta)\, cos\, \omega t \tag{2.8c}$$

where τ_0 is the constant stress amplitude. As observed, a component of the stress is in phase with the strain ($sin\,\omega t$ - elastic behavior), and the other component is in phase with the strain rate ($cos\,\omega t$ - viscous behavior). Then, the material functions for SAOS are given by

$$\frac{-\tau_{yx}}{\gamma_0} = G'\,sin\,\omega t + G''\,cos\,\omega t \tag{2.9a}$$

$$G'(\omega) \equiv \frac{\tau_0}{\gamma_0} cos\,\delta \tag{2.9b}$$

$$G''(\omega) \equiv \frac{\tau_0}{\gamma_0} sin\,\delta \tag{2.9c}$$

$$tan(\delta) = \frac{G''}{G'} \tag{2.9d}$$

where G' is the storage modulus, G'' the loss modulus and $tan(\delta)$ the damping factor. The SAOS test provides important information of viscoelastic materials, which are defined as solid-like when $tan(\delta) < 1$ and liquid-like when $tan(\delta) > 1$. Polymer solutions, suspensions, and hydrogels usually present a viscoelastic behavior. In the next section, the fundamental details associated with hydrogels are presented.

2.3 Hydrogels

Hydrogels are water-swollen polymeric materials defined by a crosslinked three-dimensional network. Their structure is formed by hydrophilic groups present in the polymer chains. These materials can absorb and retain water, in some cases up to thousands of times their dry weight (Hoffman, 2012). In the literature, the terms gel and hydrogel are often used as synonymous. Nevertheless, they are physically distinct. Gels are semi-solid systems containing small amounts of solids in a large quantity of liquid. They have a solid-like behavior also called gel-like behavior (Gupta *et al.*, 2002). On the other hand, hydrogels, by being crosslinked have limited solubility in water as illustrated in Fig. 2.11. A hydrophilic polymer dissolved in an aqueous solution is also known as hydrosol before the crosslinking. Depending on the concentration, these materials behave as liquid-like or gel-like. They cannot retain the shape as hydrogels do, in which the polymer chains movement is restricted due to intermolecular cross-

links (Peppas, 2010). The crosslinked network results in a viscoelastic behavior that provides a degree of flexibility, which in some cases is similar to the natural tissues (Gulrez *et al.*, 2011).

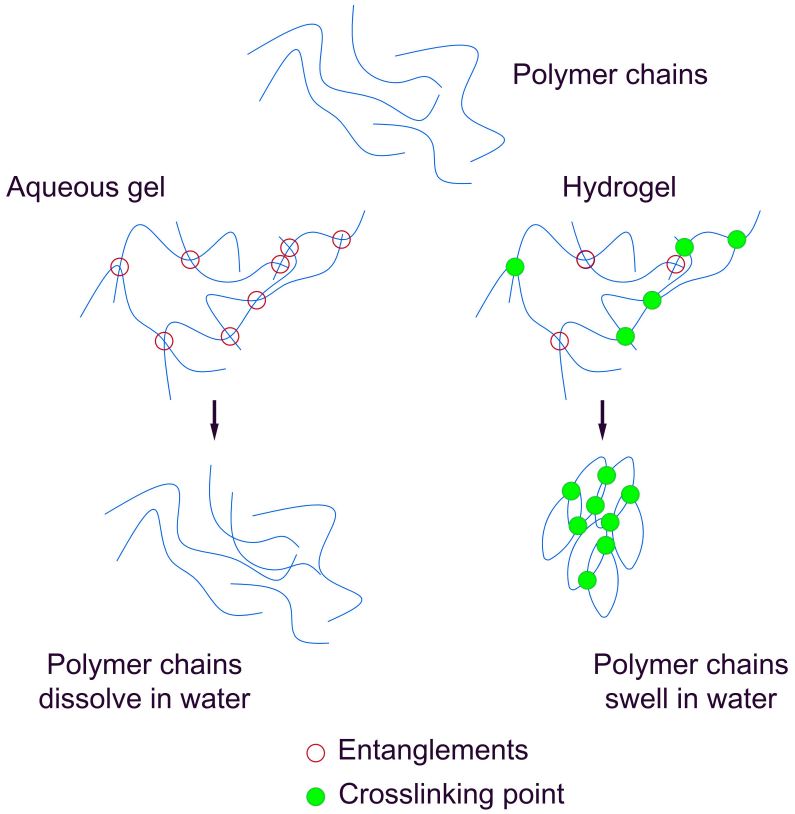

Fig. 2.11: Polymer chains forming a gel and a hydrogel.
Source: based on (Gupta *et al.*, 2002)

The physical gels easily degrade, disintegrate and dissolve. They are formed by molecular entanglements, and/or secondary forces. In these latter are included the ionic crosslinking, the hydrogen bonding or hydrophobic interactions. These gels can form hydrogels when the secondary forces restrict the polymer chains movement. Nonetheless, they are denominated reversible, because these interactions are weak and crosslinking points can be easily broken. On the other hand, chemical gels are formed by covalent crosslinking, which is stronger and stable.

Hydrogels can be obtained from synthetic or natural sources. The main advantage of synthetic hydrogels is related to their chemistry and properties, which can be easily controlled, tailored and reproduced. Alternatively, naturally derived materials such as agarose, alginate, chitosan, collagen, fibrin, gelatin, hyaluronic acid (HA), among others, are attractive for the biomedical field. They have suitable properties for this kind of applications, taking into account

that are similar to the natural extracellular matrix (ECM). Hyaluronic acid (HA) is found in several tissues. Similarly, collagens are the main ECM protein in mammalians. Linear polysaccharides, like HA, alginate, and chitosan are frequently used in Tissue Engineering (TE) because they promote tissue regeneration and interact properly *in vivo* (Barbucci, 2009; Shimojo *et al.*, 2015). Below are presented the characteristics and main details of alginate and poly(acrylamide) (PAAm), materials used throughout this research.

2.3.1 Alginate

Polysaccharides are carbohydrate macromolecules formed by monosaccharide units linked by glycosidic bonds (Radhakrishnan *et al.*, 2016). Among the naturally derived polysaccharides, alginate from brown seaweed is extensively used in biomedical applications. This material is approved by the Food and Drug Administration (FDA) agency for applications in the food industry and the medical field (Zilberman, 2011). As observed in Fig. 2.12, alginate is composed by guluronic (G) and mannuronic (M) acids. The M/G ratio influences the alginate properties. With high mannuronic acid content, hydrogels are softer and have more elasticity. On the other hand, with high guluronic acid content, hydrogels are strong but brittle (Farrés & Norton, 2014). The hydrogel stiffness is defined as follows: GG>MM>MG.

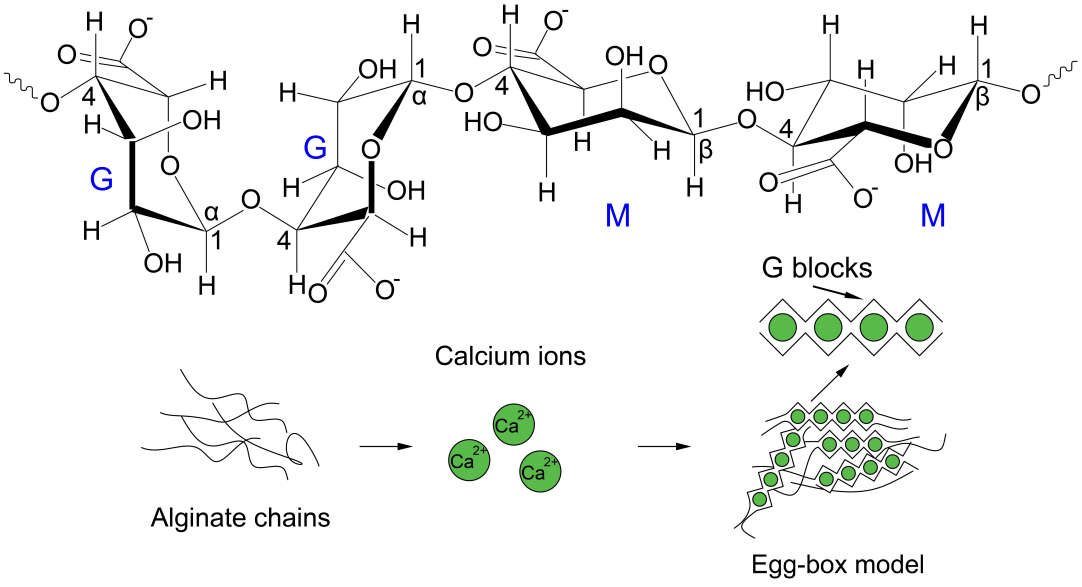

Fig. 2.12: Alginate structure and ionic crosslinking mechanism.
Source: based on Gacesa (1988); Zilberman (2011).

Physical and chemical properties of alginates depend on the composition and sequence of the polymer chain (Russo *et al.*, 2007). G blocks are linked diaxially, and M blocks have diequatorial links, for this reason, G blocks are stiffer than alternating blocks (Augst *et al.*, 2006). Alginate can be crosslinked physically by divalent or trivalent cations. As shown in Fig. 2.12, the egg-box structure is formed due to electrostatic interactions between the polyguluronate groups and the cations. Calcium ions from calcium chloride $(CaCl_2)$ aqueous solutions are commonly used to crosslink alginate due to the fast rate of crosslinking (Kuo & Ma, 2001).

2.3.2 Poly(acrylamide) (PAAm)

Poly(acrylamide) is a highly hydrophilic and bio-inert material. For these reasons, it is attractive for biomedical applications, contact lenses, sorbents, soil improvement agents, adhesives, paints, oil salvaging agents, among others (Fernández *et al.*, 2005; Darnell *et al.*, 2013). This material is formed by the polymerization of the acrylamide units, illustrated in Fig. 2.13

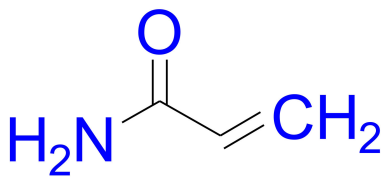

Fig. 2.13: Acrylamyde unit (AAm).
Source: Sigma-Aldrich datasheet.

Acrylamide is typically crosslinked using N,N'-methylenebisacrylamide (MBAA) to form hydrogels. One method to crosslink AAm is by a chemical reaction using ammonium persulfate as the initiator, MBAA as the crosslinker, and the accelerator N,N,N',N' tetramethylethylendiamine (TEMED) (Fernández *et al.*, 2005; Semwal *et al.*, 2016). On the other hand, AAm could be also crosslinked by photopolymerization. In this case, MBAA is also used as a crosslinker. The photoinitiator 2-hydroxy-4'-(2-hydroxyethoxy)-2-ethylpropiophenone (Irgacure D-2959) is used to start the crosslinking process in a UV light chamber of $365\ nm$ wavelength (Selen *et al.*, 2016; Kaastrup & Sikes, 2016).

2.4 Rheology modifiers

Rheology modifiers or rheological additives have been developed to tailor the flow behavior mainly of aqueous dispersions. Legislative restrictions associated with industrial products are oriented to the reduction of volatile organic compounds. Hence, aqueous dispersions together with rheology modifiers are attractive for different applications, including the food and pharmaceutical industries, cosmetic creams, lotions, cleaners, inks, paints, among others (Mezger, 2006; Braun & Rosen, 2013). These additives can be classified as shown below:

2.4.1 Polymers

Hydrophilic polymers are commonly used as rheology modifiers. The capability of polymers to influence the rheological behavior is associated with the formation of coils at rest. Depending on the concentration, a more or less entangled network is formed. Besides, physical interactions of anionic or cationic polymers or the formation of hydrogen bonds generate structures that contribute to the viscosity increase. The viscosity profile created is shear-thinning with a Newtonian plateau in the case of unlinked polymers. Contrariwise, for high concentrations, or when physical interactions link the polymer chains, the viscosity profile is defined by a strong shear-thinning behavior, and the material behaves as gel-like at rest (Glass *et al.*, 1991; Mezger, 2006).

2.4.2 Associative thickeners

Associative thickeners are water-soluble or water-dispersible polymers. They have hydrophilic and hydrophobic moieties within the same macromolecule. Hydrophobic molecular groups create connections between the polymer chains. These connections are non-permanent secondary bonds. Hence, at rest it is formed a non-permanent network maintained due to physical-chemical secondary forces. Moreover, hydrophobic segments are also capable of adsorbing on the surface of dispersed particles in the system. Then, at small shear rates, the viscosity can be tailored depending on the concentration of the components. This kind of rheology

modifiers is commonly used to obtain a moderate shear-thinning behavior (Braun & Rosen, 2013).

2.4.3 Colloidal particles

Colloidal particles are the disperse phase of a two-component system. They can be suspended in a fluid phase (continuous phase), and their size is commonly in the range from nanometers to several micrometers. They are small enough to be suspended, and their motion is affected by thermal forces (Lu & Weitz, 2013). Colloidal particles are used as rheology modifiers of liquids. The viscosity profile is directly influenced by the shape of the particle and their chemical structure. Colloidal platelets and rod-like particles are more efficient in the construction of a shear-thinning profile than spherical particles (Mewis & Wagner, 2012).

Cellulose nanocrystals (CNC) and cellulose nanofibers (CNF) are rod-like particles commonly used to tailor the rheology of aqueous solutions. They are obtained from cellulosic materials, wherein the dimensions of the rods depend mainly on the source (wood pulp, bacteria, hemp, among others) and the hydrolysis process (Liu *et al.*, 2011). The rheological behavior is influenced by transitions that are directly related to the concentration. In dilute suspensions, the rods are randomly oriented (isotropic phase). Then, when the concentration increases, a transition to an anisotropic phase occurs. At this point, the rods adopt a unidirectional self-orientation. Next, a transition to a chiral nematic anisotropic phase occurs. Stacked planes of rods are aligned along a vector, which is characteristic of liquid crystals. Highly concentrated suspensions can exhibit an arrested gel-like glassy behavior (Habibi *et al.*, 2010). Hence, the viscosity profile can be tailored from moderated shear-thinning to strong shear-thinning depending on the concentration. Similarly, the viscoelasticity is highly influenced; dilute suspensions behave as liquid-like, and a transition to solid-like takes place progressively.

Inorganic particles of clays have the form of thin platelets. At rest, these particles form a house of cards structure due to interactions between their surfaces and edges. The faces are negatively charged while the edges are positive depending on the pH of the suspension. If the clay is appropriately incorporated is obtained a strong-shear thinning profile and a gel-

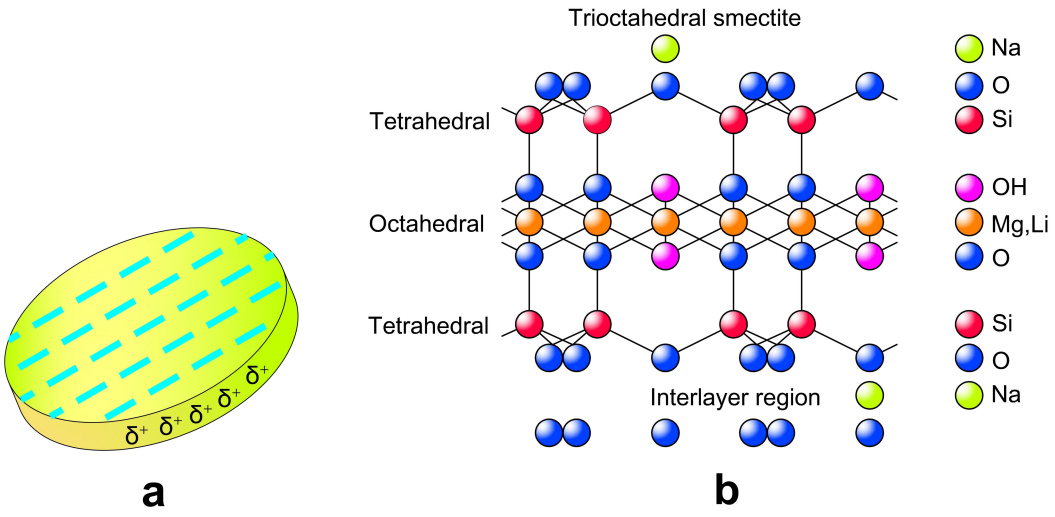

Fig. 2.14: (a) Laponite platelet ($\sim$ 0.92 nm in thickness and $\sim$ 25 nm in diameter) and (b) idealized structural formula of Laponite.
Source: based on Laponite datasheet (Technical Information B-RI 21).

like structure at rest. The yield stress is characteristic of this kind of suspensions. For high shear rates is exceeded the yield point, therefore, the house of cards structure collapses and the viscosity decreases. In Fig. 2.14 is illustrated a platelet (disk-like) of the clay Laponite and its structure. This additive is a layered silicate obtained from natural inorganic mineral sources. It is frequently used as a rheology modifier or as a film former. Laponite is available in sol and gel-forming grades. Sol grades form low viscosity colloidal dispersions while gel grades are used to produce high viscosity colloidal dispersions. These latter disperse readily in water, creating a clear colorless gel. The viscosity profile generated depends on the components concentration and the electrolyte content of the water used. Highly thixotropic gels are obtained with a concentration of at least 2 $wt.\%$. Laponite XLG, the nanosilicate used in this research has high purity, low heavy metal and microbiological content. Its applications include personal care products, cosmetics, lotions, creams, among others (Braun & Rosen, 2013).

3 LAPONITE AS A RHEOLOGY MODIFIER OF ALGINATE SOLUTIONS: PHYSICAL GELATION AND AGING EVOLUTION †

In this chapter, the rheological behavior of alginate and Laponite/alginate solutions was studied. It was observed that the Cross viscosity model successfully describes the steady-state shear behavior of this polysaccharide. The scaling behavior analyzed for the entangled regime is in good agreement with polyelectrolyte solutions $(G_e \sim c_p^{3/2})$*, with interactions generated between the alginate and the charged surfaces of the Laponite platelets. Therefore, the effect of Laponite as a rheology modifier is influenced by the alginate concentration. Higher alginate concentrations hindered the formation of the house of cards microstructure. Frequency sweep tests were performed to analyze the transition from solid-like to liquid-like behavior in a solid-like dominated domain. Soft physical gels were obtained at low alginate concentrations. The gel point was determined (*$1.65\ wt.\%$ *of alginate and* $2\ wt.\%$ *of Laponite) through the Kramers-Krönig damping factor, and time sweep tests revealed the evolution of the storage* (G') *and loss modulus* (G'') *as functions of the waiting time* (t_w)*. The growing elasticity revealed that Laponite/alginate solutions undergo aging.*

3.1 Introduction

Alginate is an anionic polysaccharide that can be extracted from macroalgae or bacterial cultures. It is a copolymer of $(1-4)$-linked β-D-mannuronate (M) and α-L-guluronate (G) residues (Gacesa, 1988; Percival, 1979). The ratio of guluronic to mannuronic acid depends on the source. Alginates are block polymers; they are linear unbranched copolymers containing similar or strictly alternating blocks: MM, GG or GM. M and G acids are covalently linked, forming different sequences or blocks. Two adjacent G blocks can be cross-linked with multivalent cations: divalent cations such as Ca^{2+}, Ba^{2+}, Fe^{2+} or Sr^{2+} or trivalent cations such as Al^{3+}. Hence, a gelling mechanism occurs when those cations take part in ionic binding zones between G blocks (Augst *et al.*, 2006; Rezende *et al.*, 2009). Thereby, a three-dimensional network is formed. Binding zones are often called "egg boxes" (Percival, 1979; Papajová *et al.*,

† The original publication is available at Carbohydrate Polymers https://doi.org/10.1016/j.carbpol.2016.09.057, (Dávila & d'Ávila, 2017)

2012; Venkatesan *et al.*, 2015; Larsen *et al.*, 2015).

Alginate is characterized by its hydrophilicity. It can easily form aqueous solutions in which the viscosity increases with the alginate content and its molar mass. Aqueous alginate solutions are non-Newtonian fluids, presenting shear-thinning behavior (Rezende *et al.*, 2009). Due to its biocompatibility, non-toxicity and gelling mechanism, alginate has been widely used in tissue engineering applications, cell encapsulation, drug and protein delivery, and as pharmaceutical excipients, among other functions (Rodríguez-Rivero *et al.*, 2014). Moreover, alginate is commonly used as a gelling agent in the food industry, textile/paper industry, and for dental impressions and wound dressings (Augst *et al.*, 2006; Fu *et al.*, 2011).

Laponite is a layered nanosilicate with the empirical formula $Na_{+0.7}\left[\left(Mg_{5.5}Li_{0.3}\right)Si_8O_{20}\left(OH\right)_4\right]^{-0.7}$ (Perkins *et al.*, 1974; Thompson & Butterworth, 1992; Xavier *et al.*, 2015). It is a synthetic material obtained from a combination of salts of sodium, magnesium and lithium with sodium silicate. One of the applications of Laponite is as a rheology modifier (Ruzicka & Zaccarelli, 2011). It is an additive that promotes shear-thinning and thixotropic behavior in waterborne products (Willenbacher, 1996). In recent studies, Laponite was used to reinforce hydrogels for biomedical applications (Shen *et al.*, 2014; Hong *et al.*, 2015). Moreover, as reported by Xavier *et al.* (2015), nanocomposites reinforced with Laponite can support cellular adhesion and enhance in vitro mineralization and physiological stability, which expands the applications in the tissue engineering (TE) field. Laponite platelets are nanoscale disk-like particles with an aspect ratio of $1 : 25$. They are formed in layers: two parallel sheets of tetrahedrally coordinated silica and a sheet of octahedrally coordinated magnesium oxide between them. Oxygen and OH^- groups are also present in the Laponite structure (Zulian *et al.*, 2008). Furthermore, some magnesium atoms are substituted by lithium atoms. Therefore, a negative charge is on the platelet surfaces, whereas positive charges are on the rim due to the interlayer cations. In this case, the sodium ions balance the charges (Ruzicka & Zaccarelli, 2011). Conversely, when Laponite is dispersed in water, sodium ions are released, and the charges are unbalanced. Thus, the platelets adopt a negative charge on their faces, while the rims can adopt a positive or negative charge depending on the pH of the solution (Sun *et al.*, 2012; Morariu *et al.*, 2014; Mongondry *et al.*, 2005; Tawari *et al.*, 2001; Joshi *et al.*, 2008; Kumar *et al.*, 2016).

Aqueous Laponite dispersions undergo physical aging because they are out of thermodynamic equilibrium. Hence, the microstructure of these dispersions progressively evolves to a lower level of energy (Shahin & Joshi, 2010; Jatav & Joshi, 2014). Thermal motion and particle aggregation due to the electrostatic forces between them influence physical aging (Jatav & Joshi, 2014; Labanda & Llorens, 2008), as do the Laponite concentration and the addition of polymers, salts or other components. It is reported in the literature that the intensity of the positive charges on the rims decreases as the pH increases; the rim is positively charged at $pH \leq 11$ (Shahin & Joshi, 2010; Sun *et al.*, 2012). With positive rims, a “house of cards"microstructure is formed by the platelets due to the electrostatic interactions between them and the faces (Mongondry *et al.*, 2005; Liu & Bhatia, 2015). This microstructure is also responsible for the viscosity increase and the shear-thinning effect of aqueous Laponite dispersions (Mongondry *et al.*, 2005). Under low shear rates, the house of cards structure is adopted, but it collapses at high shear rates. In this case, the platelets are oriented in the flow direction, and the viscosity decreases. Contrariwise, the negative charges on the rims have an influence on the elastic behavior of the dispersion due to the repulsion between platelets.

The electrostatic interaction between Laponite platelets and the mechanism of the formation of the microstructures are yet a matter of debate. The Laponite concentration plays an important role in the dispersion microstructure. Below a $2\ wt.\%$ Laponite concentration, the house of cards microstructure is suggested. Conversely, above this concentration, two proposals are suggested in the literature: (i) a house of cards or (ii) a Wigner repulsive glass microstructure. This latter takes into account the repulsion between Laponite platelets (Zulian *et al.*, 2008; Jatav & Joshi, 2014). These microstructures evolve due to aging and can be destroyed by applying a deformation onto the sample, in a process called rejuvenation. The applied deformation should generate a stress greater than the yield stress of the sample (Jatav & Joshi, 2014). To perform rejuvenation, pre-shear or shear melting processes are carried out before the rheological studies. Sun *et al.* (2012) studied the aging phenomena in aqueous Laponite dispersions containing polyethylene glycol (PEG) and $NaCl$. To rejuvenate the samples to set a reference initial condition for the tests, a uniform shear field was applied. As observed in the dynamic time sweep test, a reproducible liquid state was achieved. Nevertheless, it is observed that the aging is partially irreversible, as described by Jatav & Joshi (2014); a shear melting process was previously applied to the rheological characterization of aqueous Laponite dispersions. In this

case, an oscillatory shear stress was applied to rejuvenate the samples. As demonstrated, the shear melting rejuvenates the sample, although not completely; a slight difference is observed in comparison with a freshly prepared sample (Shahin & Joshi, 2010; Jatav & Joshi, 2014).

As previously described, the addition of salts and polymers modifies the aging of dispersions. Salt reduces the electrostatic repulsion between Laponite platelets, accelerating the aggregation for low concentrations of Laponite because the surface charge is screened (Sun *et al.*, 2013). The addition of salt also modifies the microstructure from glass-like to gel-like. The gel state has a fractal network, while the glass state does not have an ordered microstructure (Joshi *et al.*, 2008). Moreover, the pronounced shear-thinning and solid-like behaviors provide interesting results for additive manufacturing (AM) applications in tissue engineering. Solutions rheologically modified could easily flow through nozzle tips due to the shear rate generated along their walls. Once out of a nozzle, the material could maintain its shape as result of the high viscosity (Barry *et al.*, 2009; Hong *et al.*, 2015). Subsequently, a crosslinking process can be applied to form hydrogels, thereby improving the geometric accuracy. In this chapter, the rheological behavior of alginate aqueous solutions and Laponite/alginate solutions was studied. A steady-state shear master curve for alginate solutions was obtained. When Laponite was added to the alginate solutions, a pronounced shear-thinning behavior was observed in steady-state shear tests. Then, frequency sweep tests were performed to analyze the physical gelation due to the electrostatic interactions between the Laponite platelets and alginate chains. The damping factor of the solutions was analyzed as a function of the alginate concentration, where the gelation mechanism, which arises due to the dispersed Laponite platelets, was studied. Finally, time sweep tests were performed to analyze the aging evolution of the Laponite/alginate samples under the gel point concentration.

3.2 Experimental

3.2.1 Material and solution preparation

Medium-viscosity sodium alginate from brown algae was purchased from Sigma-Aldrich Corp., USA. Its molar mass ranges between $80{,}000$ and $120{,}000\ g\,mol^{-1}$, and it is composed of

approximately 61% mannuronic acid and 39% guluronic acid. Laponite XLG was obtained from Southern Clay Products, Inc., USA. Sodium chloride was purchased from Labsynth, Brazil. $0.1\ M\ NaCl$ was added to the dilute alginate solutions to determine the viscosity-average molar mass using the Mark-Houwink-Sakurada correlation, which is given by

$$[\eta] = K{M_v}^{\alpha} \tag{3.1}$$

where $[\eta]$ is the intrinsic viscosity, $K = 7.3 \times 10^{-3}\ g.ml^{-1}$ and $\alpha = 0.92$ for an M/G ratio of 1.56 (Thu *et al.*, 1996). The specific and reduced viscosities are given by Eq. (3.2) and Eq. (3.3), respectively,

$$\eta_{sp} = \frac{\eta_0 - \eta_s}{\eta_s} \tag{3.2}$$

$$\eta_{red} = \frac{\eta_{sp}}{c_p} \tag{3.3}$$

where η_0 is the zero shear viscosity, η_s the solvent viscosity ($\eta_s = 0.001003\ Pa.s$ at $20\ ^{\circ}\mathrm{C}$) and c_p the polymer concentration. The intrinsic viscosity is given by

$$[\eta] = \lim_{c_p \to 0} \left(\frac{\eta_{sp}}{c_p} \right) \tag{3.4}$$

All solutions were prepared using deionized water (Type II, conductivity $< 1\ \mu S\ cm^{-1}$) without added $NaCl$, except that to determine the viscosity-average molar mass. Alginate solutions and Laponite/alginate solutions were prepared using a magnetic stirrer for 6 hours with a plate temperature of $60\ ^{\circ}\mathrm{C}$ to ensure homogeneity. All samples were stored for 16 hours before the rheological tests. The Laponite/alginate solutions were prepared using $2\ wt.\%$ Laponite. The alginate concentration was varied in the range of 0.25 to $4\ wt.\%$ for the steady-state

shear and frequency sweep tests. For the time sweep tests, alginate concentrations with a solid-like behavior (0.25 to 1 $wt.\%$) were analyzed. To prepare the solutions, it was necessary to completely disperse and hydrate the Laponite before the addition of the alginate. Laponite was dispersed in deionized water using a vortex agitator. It was added gradually into the water over a period of 10 to 30 s to reduce the dispersion time, and a clear colorless solution was obtained in approximately 20 min. The pH of the solutions was measured using samples of approximately 10 ml in a Tecnal TEC-5 pH meter.

3.2.2 Rheological characterization

The rheological characterization of the solutions was performed using an Anton Paar MCR-102 Modular Compact Rheometer. Tests were conducted using a cone-plate geometry (CP50-1) with a 50 mm diameter, a cone angle of $0.9815°$ and a truncation of 0.97 μm. To determine the viscosity-average molar mass, steady-state shear tests were performed at 20 °C, while all the other experiments were performed at 25 °C. The rheological characterizations were carried out using a solvent trap to prevent water evaporation. Before each test, a constant pre-shear of 200 s^{-1} was applied for 300 s to avoid any memory effect and rejuvenate the samples. Measurements of the shear rate in the steady-state were performed in the range of 0.001 to 700 s^{-1}. Amplitude sweep tests were carried out at an angular frequency of 10 $rad\,s^{-1}$ to obtain the linear viscoelasticity (LVE) range ($\gamma_{LVE} = 1\%$ for all samples). Next, frequency sweep tests were conducted in the range of 0.1 to 200 $rad\,s^{-1}$. Finally, time sweep tests were performed to study the aging evolution. Each time sweep test was carried out for 1000 s, and the angular frequency was varied from 10 to 100 $rad\,s^{-1}$.

3.3 Results and discussion

3.3.1 Steady-state shear characterization

Initially, the intrinsic viscosity was obtained by a linear fit of the curve of reduced viscosity versus alginate concentration (Fig. 3.1). Then, using the Mark-Houwink-Sakurada cor-

relation, a viscosity-average molar mass of 99,986 $g\ mol^{-1}$ was calculated, which is inside the range of molar mass provided by the supplier (80,000 - 120,000 $g\ mol^{-1}$).

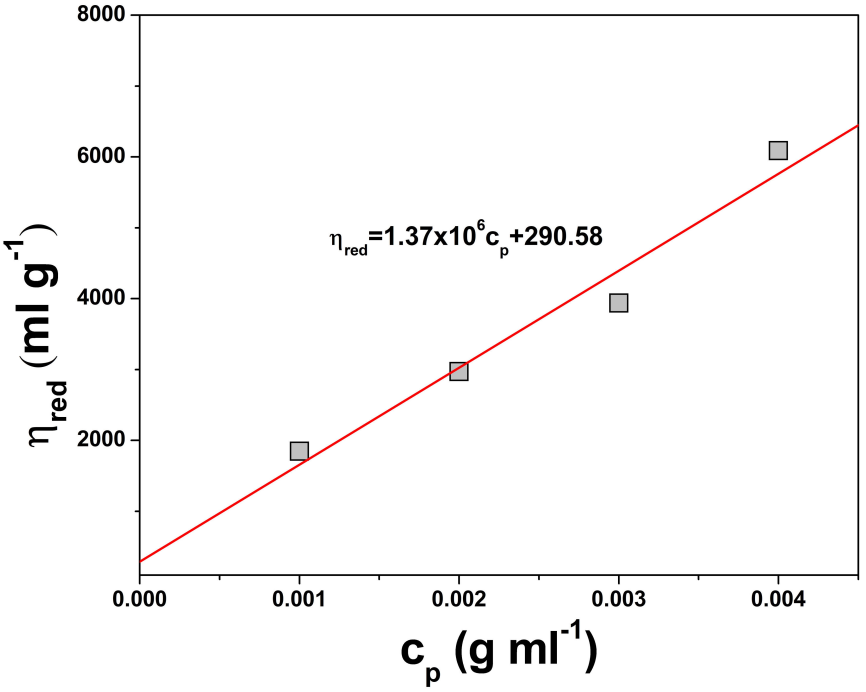

Fig. 3.1: Reduced viscosity (η_{red}) versus alginate concentration (c_p).

Next, different concentrations of alginate solutions were studied. As observed in Fig. 3.2a, when the alginate concentration increases, the viscosity of the solution also increases. Shear-thinning behavior can be observed for all cases, even in low-concentration solutions. In the range of shear rates studied, all compositions, except for the one with 4 wt.% of alginate, exhibit a Newtonian plateau. The shear-thinning is associated with an entangled network and is the typical behavior of polymer solutions (Yu *et al.*, 2014). Next, using the steady-state shear viscosity data obtained, a master curve was constructed. This method has been applied successfully in other polysaccharide solutions (Payet *et al.*, 2010; Gorret *et al.*, 2003). The vertical and horizontal shift factors were calculated using as references a 1 wt.% alginate concentration, the zero shear viscosity for the vertical axis and the initial point of shear-thinning behavior for the horizontal axis. As observed in Fig. 3.2b, the viscosity master curve shows that the superimposed data have a common mechanism that governs the alginate viscoelasticity. The shear-thinning behavior is generated due to the disentanglement of the polymer chains. These chains need time to relax, and then the transition from the Newtonian plateau to shear-thinning behavior occurs at a critical shear rate equal to the inverse of the relaxation time. In addition, Fig. 3.2b shows

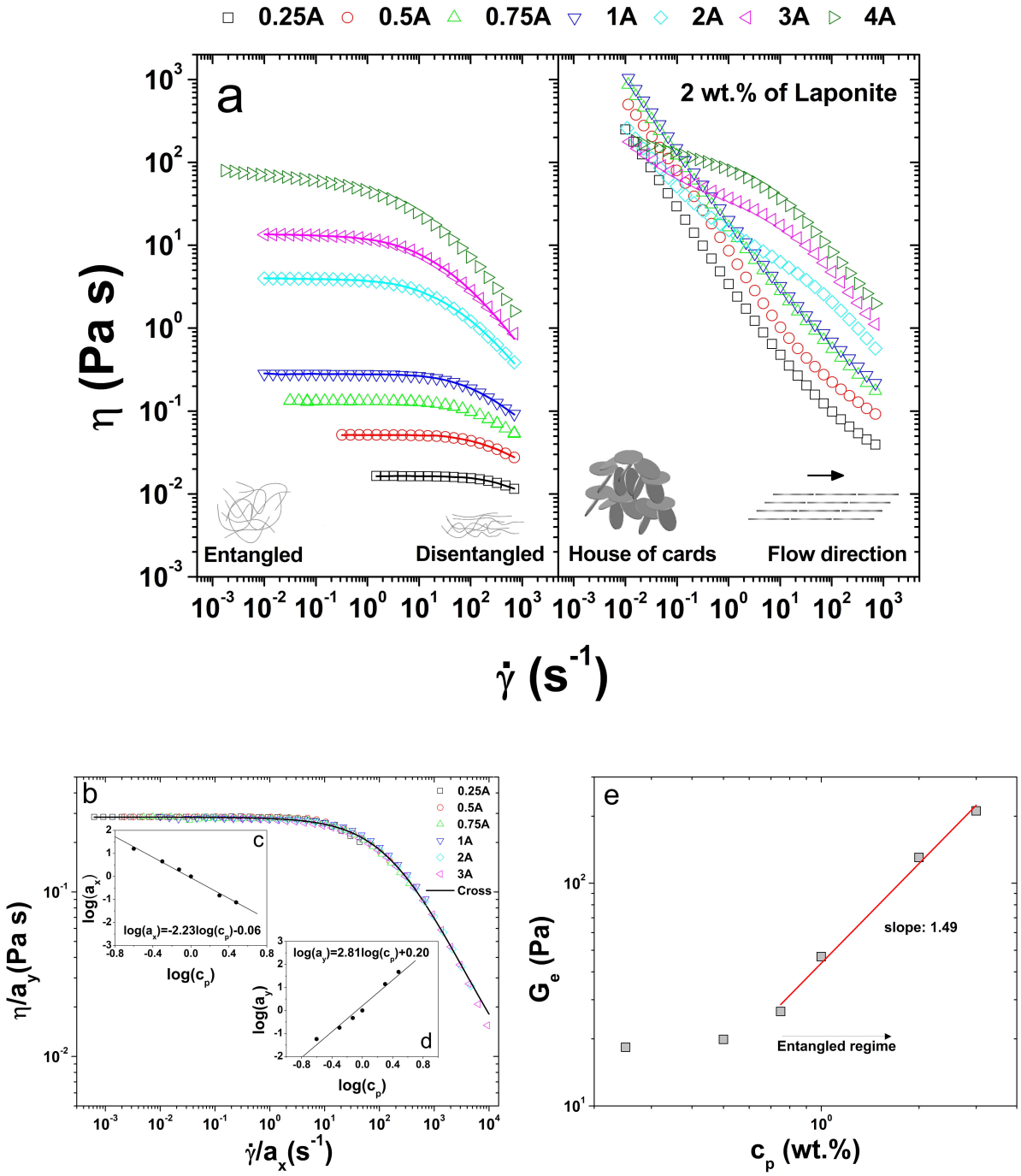

Fig. 3.2: (a) Viscosity (η) curves for aqueous alginate and Laponite/alginate solutions. Open symbols correspond to experimental data. Solid lines correspond to the Cross model fitting for alginate. Inset schemes describe the mechanisms that contribute to the shear-thinning behavior, (b) alginate viscosity master curve (reference concentration 1 wt.%), (c) and (d) horizontal (a_x) and vertical (a_y) shift factors vs. concentration and (e) plateau modulus (G_e) as a function of the alginate concentration (c_p) (results were scaled for the entangled regime). "A" represents the alginate concentration.

the fitted master curve using the Cross model, which successfully describes the shear-thinning behavior of polysaccharide solutions (Roger *et al.*, 2015). This model is given by

$$\eta(\dot{\gamma}) = \eta_\infty + \frac{\eta_0 - \eta_\infty}{1 + (\dot{\gamma}/\dot{\gamma}_c)^n} \tag{3.5}$$

where η_∞ is the infinite shear viscosity, η_0 the zero-shear viscosity, $\dot{\gamma}$ the shear rate, $\dot{\gamma}_c$ the critical shear rate, and n the power-law index. As observed in Fig. 3.2(b-d), the Cross model fits the experimental results quite well, especially for the lower shear rates. The Carreau model also describes the shear-thinning behavior, but as reported by Payet *et al.* (2010), the Cross model fits better, especially at high shear rates. Table 3.1 summarizes the experimental and fitting parameters and the mean relative deviations (MRD) of the fitted curves.

Table. 3.1: Shift factors for the experimental viscosity master curve and fitting parameters for the Cross model.

Experimental						
$c_p(wt.\%)$	0.25	0.5	0.75	1	2	3
a_x	16	4.5	2	1	0.15	0.075
a_y	0.0574	0.178	0.473	1	14.072	47.607
Fit						
$c_p(wt.\%)$	$\eta_\infty\,(Pa\ s)$	$\eta_0\,(Pa\ s)$	$\dot{\gamma}_c\,(s^{-1})$	n	$MRD(\%)$	
0.25	0.0039	0.0165	1111.1	0.9999	0.4	
0.5	0.0143	0.0517	384.6	0.9999	0.6	
0.75	0.0319	0.1327	200.0	0.9998	0.8	
1	0.0413	0.2806	166.7	0.9164	0.5	
2	0.0169	3.9892	32.7	0.7415	0.5	
3	0	13.5352	15.6	0.7094	1.5	
Master curve	0.0036	0.2847	204.08	0.7484	1.9	

The scaling behavior of the plateau modulus, which describes the chain entanglement effects (Yu *et al.*, 2014) in the alginate solutions, was determined by rheological data. This modulus can be calculated by

$$G_e = \frac{\eta_0}{\lambda} \tag{3.6}$$

where λ is the relaxation time, calculated as the inverse of the shear rate at which the transition from Newtonian to shear-thinning behavior occurs. In Fig. 3.2e are shown the scaled results for entangled solutions. As observed, they are consistent with the scaling law for polyelectrolyte solutions $(G_e \sim c_p^{3/2})$ (Yu *et al.*, 2014; Colby, 2010). Nevertheless, a recent study reported that the exponential value of the scaling behavior could be higher than $(3/2)$; an exponent between $2-3$ is suggested due to the monomers' dipolar interactions through counterions (Roger *et al.*, 2015). For high polymer concentrations, the electrostatic interactions of the polyelectrolytes can be neglected, and the behavior could be similar to that of a good solvent scaling exponent (2.25) (Dou & Colby, 2006).

Charged surfaces cause the adsorption of polyelectrolytes. Therefore, the anionic polyelectrolyte behavior of the alginate solutions generates interactions with the charged Laponite particles. As previously observed in Fig. 3.2a, the viscosity curves of Laponite/alginate solutions show the influence of Laponite on the rheological behavior. In all cases, the viscosity decreases when the shear rate increases. At low shear rates, a high viscosity is observed in comparison to that of the alginate solutions. Conversely, a low viscosity is observed for high shear rates. In Laponite/alginate solutions, the shear-thinning effect would be associated with the disentanglement of polymer chains and the Laponite platelet orientation in the flow direction (Aalaie, 2012). As a result, at high shear rates, these solutions exhibit little resistance to flow. When the shear rate is reduced, the alginate chains become entangled. Moreover, the Laponite platelets form a house of cards structure, considerably increasing the viscosity in comparison to that of alginate solutions. This structure is formed due to electrostatic interactions (Mongondry *et al.*, 2005). At low shear rates, a gel structure forms if Laponite is properly incorporated into the solution. Contrariwise, at high shear rates, the house of cards structure completely disappears due to shear forces. Hence, a pronounced shear-thinning behavior is observed. Additionally, as observed in Fig. 3.2a, higher alginate concentrations hinder the effect of Laponite as a rheology modifier due to polymer adsorption on the Laponite surfaces. This is associated with the polyelectrolyte behavior previously described. Therefore, in Laponite/alginate solutions, for high alginate concentrations, the viscosity curves differ slightly from those of alginate solutions.

3.3.2 Physical gelation

To analyze the physical gelation generated due to the interactions between Laponite and alginate, frequency sweep tests were performed. Fig. 3.3 shows the results for alginate solutions in the entangled regime. For all cases, a crossover point defines the transition from a liquid-like dominated domain $(G'' > G')$ to a solid-like dominated domain $(G' > G'')$. As shown, the crossover frequency (ω_x) is higher for lower alginate concentrations. This frequency is often associated with the longest relaxation time of the material, which is calculated as the inverse of the crossover frequency. Hence, the relaxation time increases as a function of the alginate concentration. This time defines the period in which the polymer chains can disentangle as a result of the oscillating shear applied. Longer chains cannot disentangle, which causes the transition from liquid-like to solid-like behavior (Yu *et al.*, 2014). Fig. 3.4 shows the damping factor $(tan(\delta) = G''/G')$ as a function of the alginate concentration. As shown, at high frequencies, the solid-like behavior is dominating $(tan(\delta) < 1)$. Moreover, the damping factor decreases when the alginate concentration increases. This is, larger amounts of polymer contribute to the solid-like behavior, thus decreasing $tan(\delta)$.

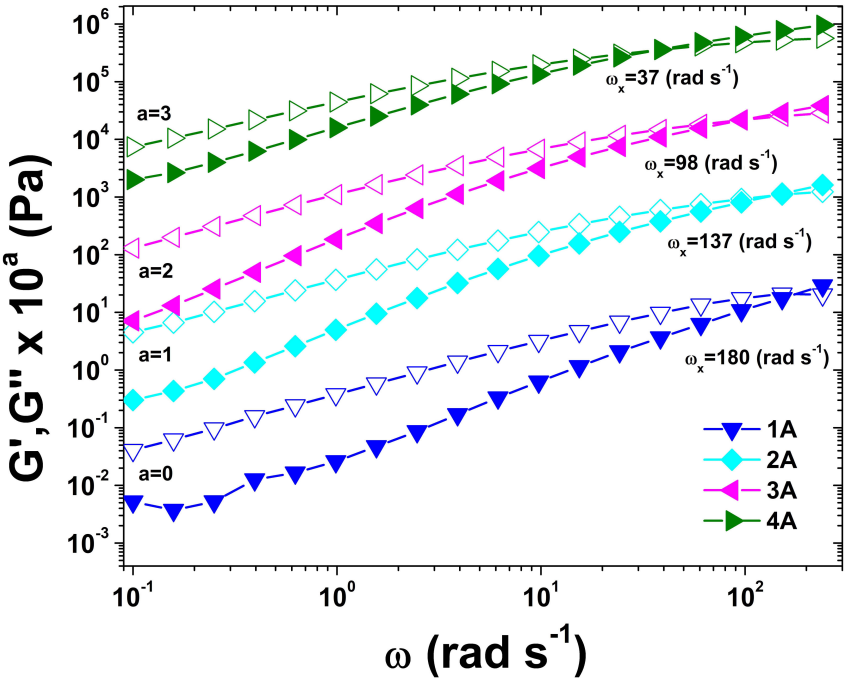

Fig. 3.3: Dependence of the storage modulus (G') (solid symbols) and the loss modulus (G'') (open symbols) on the angular frequency (ω) for alginate solutions in entangled regime. Data are vertically shifted to avoid overlapping, ω_x is the crossover frequency and "A" represents the alginate concentration (c_p).

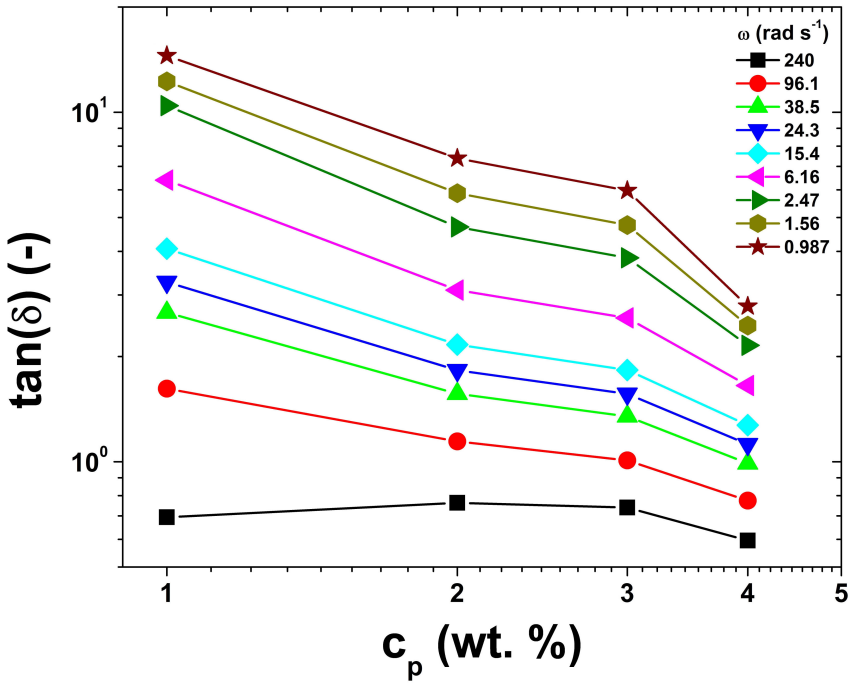

Fig. 3.4: Damping factor $(tan(\delta))$ plotted against the alginate concentration (c_p) for different angular frequencies (ω).

On the other hand, Fig. 3.5 shows the storage and loss moduli as functions of the angular frequency for Laponite/alginate solutions. As shown, soft gels were obtained at low alginate concentrations. Taking into account that aqueous alginate solutions are polyelectrolytes, alginate could adsorb on an oppositely charged surface, in this case, the charged surfaces of Laponite. Table 3.2 shows the pH values for alginate and Laponite/alginate solutions; as observed, $pH \leq 11$ for all cases. Hence, it is suggested that alginate, which is an anionic polymer, is being adsorbed on the positively charged surface of the Laponite, in this case, the rim of the platelets. As a result, when the alginate concentration increases, a transition from solid-like to liquid-like behavior is observed. At low alginate concentrations, physical gelation occurs as a result of Laponite-alginate interactions. Conversely, alginate adsorption on Laponite surfaces at higher alginate concentrations hinders the rheology modifier effect because the formation of the house of cards structure is difficult. Fig. 3.6a shows the damping factor plotted against the angular frequency. This curves were superimposed by horizontal and vertical shifting, as illustrated in Fig. 3.6b, revealing that the transition from a dominant solid-like behavior to a liquid-like behavior follows a similar route when the alginate concentration increases and the Laponite concentration is maintained fixed at $2\ wt.\%$.

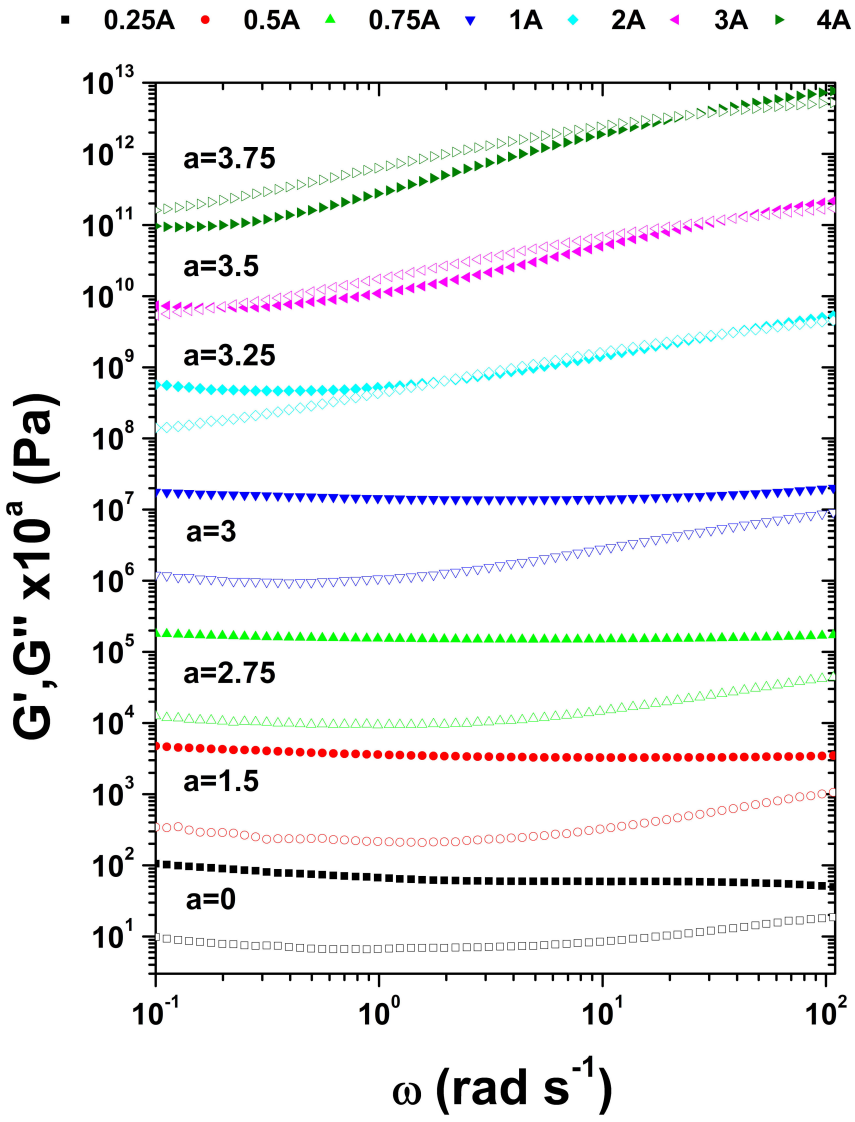

Fig. 3.5: Dependence of the storage modulus (G') (solid symbols) and the loss modulus (G'') (open symbols) on the angular frequency (ω) for 2 $wt.\%$ Laponite in the presence of different alginate concentrations ("A"). Data are vertically shifted to avoid overlapping.

Table. 3.2: pH values for Laponite/alginate solutions (c_L is the Laponite concentration and "A" represents the alginate concentration (c_p)).

$c_L(wt.\%)$	0.25A	0.5A	0.75A	1A	2A	3A	4A
0	6.86	6.85	6.87	7.51	7.34	7.52	7.94
2	9.99	9.82	9.63	9.74	9.51	9.18	9.12

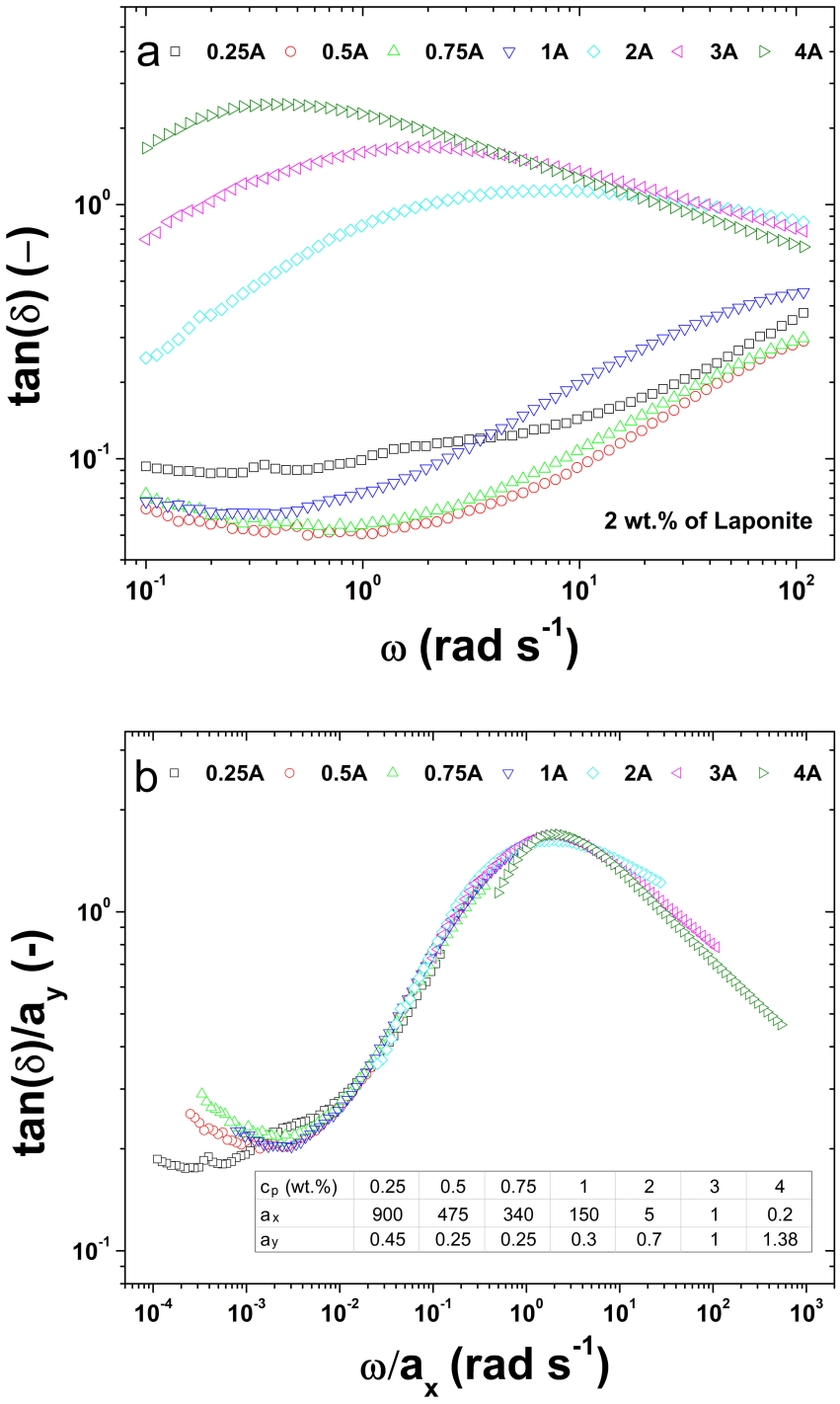

Fig. 3.6: (a) Damping factor $(tan(\delta))$ plotted against angular frequency (ω) and (b) damping factor superimposed curve for Laponite/alginate solutions (inset table shows the horizontal (a_x) and vertical (a_y) shift factors. Reference concentration: $3\ wt.\%$ alginate. "A" represents the alginate concentration (c_p)).

The transition from solid-like to liquid-like behavior can be analyzed through the damping factor. This transition is defined by the gel point. The damping factor from Kramers-Krönig is defined by Eq. (3.7) (Liu *et al.*, 2003), which has no dependence on the angular frequency at

the gel point:

$$tan\,(\delta) = \frac{G''}{G'} = tan\left(\frac{n\pi}{2}\right) \tag{3.7}$$

The gel point is defined by the relaxation modulus $G(t)$ of a critical gel. This modulus was proposed by Winter & Chambon (1986), as a power-law described by

$$G\,(t) = St^{-n} \tag{3.8}$$

where S is the gel strength and n the relaxation exponent $(0 < n < 1)$. The gel strength can be determined by Eq. (3.9) at the gel point (Jatav & Joshi, 2014),

$$G' = \frac{G''}{tan\left(\frac{n\pi}{2}\right)} = S\omega^n \Gamma\,(1-n)\,cos\left(\frac{n\pi}{2}\right) \tag{3.9}$$

where $\Gamma()$ is the gamma function. Therefore, the gel strength can be calculated by obtaining n from Eq. (3.7) and G' or G''.

Fig. 3.7 shows plots of the damping factor against the alginate concentration for different frequencies. Fig. 3.7a reveals that the solid-like behavior dominates at small frequencies for alginate concentrations under $1\ wt.\%$, while, Fig. 3.7b and c show no frequency dependence at $c_p = 2.61\ wt.\%$ and $c_p = 3.32\ wt.\%$. At these concentrations, transitions from solid-like to liquid-like behavior occur in a liquid-like dominated domain $(tan(\delta) > 1)$. Moreover, Fig. 3.7d shows no frequency dependence at $c_p = 1.65\ wt.\%$ and $tan(\delta) = 0.73$. At this concentration, a transition from solid-like to liquid-like behavior occurs in a solid-like dominated domain $(tan(\delta) < 1)$. Therefore, at this concentration, the gel point is defined, below which, soft gels were obtained. When the alginate concentration increases, a progressive increase in the damping factor is observed, suggesting a reduction in the elasticity. This fact explains the considerable reduction of the shear-thinning effect of Laponite when the alginate concentration increases.

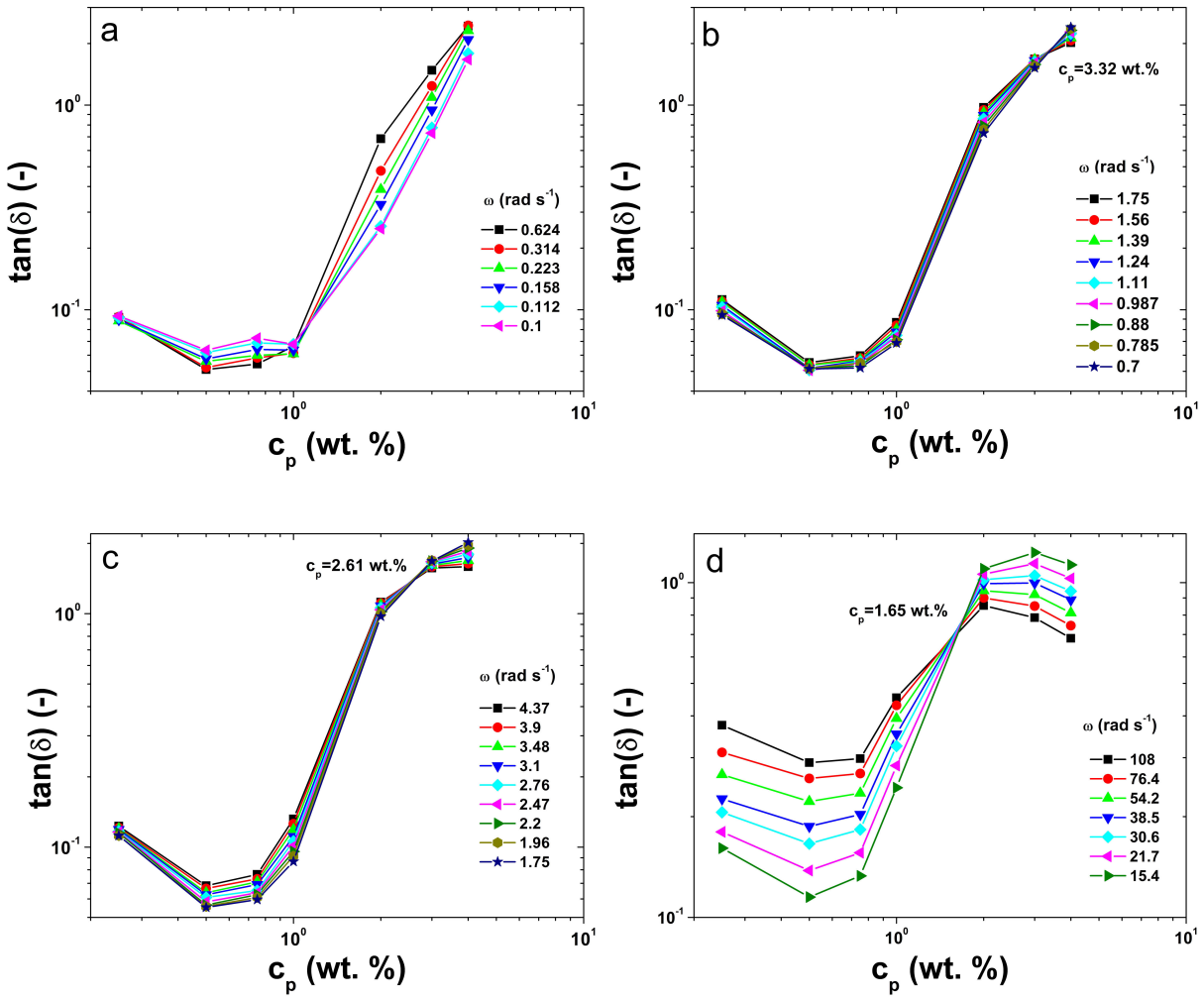

Fig. 3.7: Damping factor $(tan(\delta))$ plotted against the alginate concentration (c_p). The angular frequency (ω) increases from (a) to (d).

Furthermore, as observed in Fig. 3.7, the plotted data are mainly in the region $tan(\delta) < 1$. That is, the solid character of the material prevails over the viscous $(G' > G'')$. In contrast, the damping factor of alginate solutions previously shown in Fig. 3.4b shows that plotted data are mainly in the region $tan(\delta) > 1$. Moreover, when the alginate concentration increases, the elasticity also increases for the alginate solutions and decreases in the Laponite/alginate solutions. For this reason, soft gels are formed mainly at lower alginate concentrations.

3.3.3 Aging evolution

Fig. 3.8a shows the storage modulus (G') and the loss modulus (G'') obtained through time sweep tests carried out at different angular frequencies for the composition of 0.25 wt.$\%$

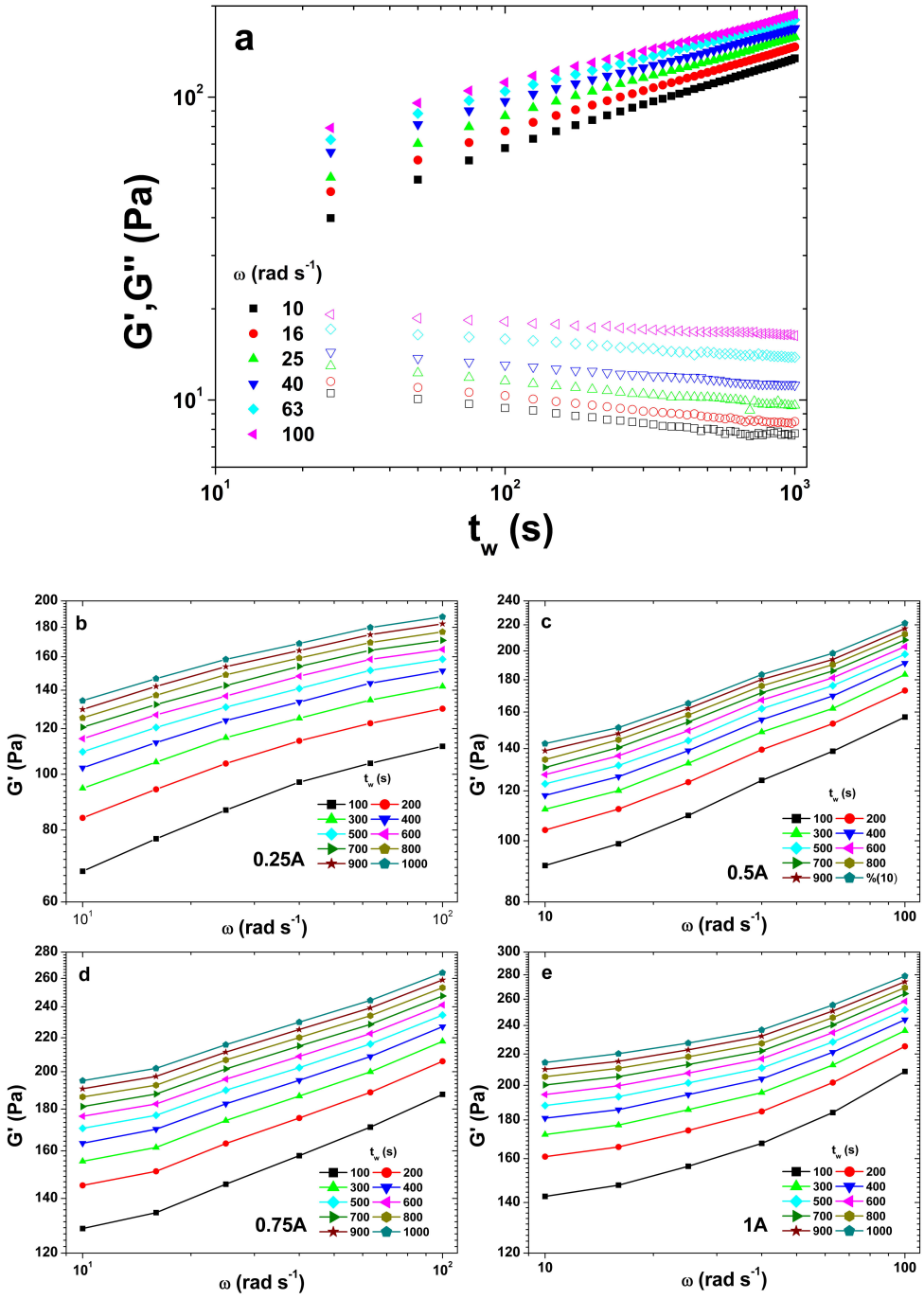

Fig. 3.8: Aging evolution: (a) dependence of the storage modulus (G') (solid symbols) and the loss modulus (G'') (open symbols) on the waiting time (t_w) for angular frequencies (ω) in the range of 10 to 100 $rad\ s^{-1}$ for the composition 0.25 wt.$\%$ alginate and 2 wt.$\%$ Laponite and (b-e) reconstructed frequency dependence of G' for different waiting times.

alginate and 2 wt.$\%$ Laponite. As observed, G' increases as a function of the waiting time (t_w) and the angular frequency (ω). Similar behavior was observed for the other compositions (for clarity, only one composition was depicted, while the other compositions are illustrated in the Appendix A). G'' also increases with the frequency, but slightly decreases at low waiting ti-

mes and remains constant at high waiting times. G' is higher than G'', corroborating a solid-like behavior when the aging was analyzed in compositions under the gelling point. Hence, the damping factor decreases with the waiting time, which demonstrates a growing Hookean elasticity (Sun *et al.*, 2012). Moreover, the frequency dependence of G' was reconstructed, which is depicted in Fig. 3.8(b-e) for different compositions and waiting times. In these curves, there can be clearly observed a growing elasticity as a function of the waiting time and frequency. The storage modulus also increases with the alginate concentration due to the structural interactions generated between the polymer chains and the Laponite platelets over time. Then, the evolution of the elastic behavior demonstrates that Laponite/alginate solutions undergo aging.

3.4 Summary

Rheological studies performed in alginate and Laponite/alginate solutions allowed the analysis of the mechanism that influences the transition from a shear-thinning behavior in alginate solutions to a pronounced shear-thinning behavior when Laponite is added. Electrostatic interactions between charged Laponite platelets generate a house of cards structure when the shear rate tends to zero. Therefore, at low shear rates, the entangled alginate chains and the house of cards structure contribute to increasing the viscosity considerably. In addition, a solid-like dominated behavior arises due to interactions between the alginate chains and Laponite platelets. As demonstrated, alginate solutions have a polyelectrolyte behavior ($G_e \sim c_p^{3/2}$). Therefore, taking into account that alginate is an anionic polysaccharide and the rim of the Laponite platelets is positively charged at $pH \leq 11$, it is suggested that the alginate adsorbs on the positive surfaces of Laponite, which hinders the increase in viscosity at high alginate concentrations. Frequency sweep tests revealed that Laponite produces physical gelation in alginate solutions. Moreover, the damping factor from Kramers-Krönig allowed the determination of the gel point. This last factor defines the transition from solid-like to liquid-like behavior, which follows a similar route, as revealed by a superimposed curve. As observed, at the gel point, the damping factor has no dependence on the frequency. Finally, time sweep tests revealed a growing elasticity as a function of the waiting time. Hence, Laponite/alginate solutions undergo aging. Furthermore, it is anticipated that Laponite/alginate solutions together with AM processes have potential for biomedical applications.

4 RHEOLOGICAL EVALUATION OF LAPONITE/ALGINATE INKS FOR 3D EXTRUSION-BASED PRINTING‡

The 3D printing of soft materials is challenging mainly due to their rheological behavior. The 3D extrusion-based printing was correlated with the rheological properties for each stage of the process. A protocol to obtain an optimal ink was defined and Laponite/alginate mixtures were analyzed. All mixtures exhibited a pronounced shear-thinning behavior. Higher alginate concentrations partially hindered the rheology modifier effect of Laponite. The filament formation during extrusion and good printability were observed for Laponite concentrations of at least $5\ wt.\%$*. The optimal ink was defined as a function of the viscosity profile, the filament formation ability, the flow-point and the solid-like/liquid-like behaviors. The viscosity recovery test demonstrated an instant structure recovery for the optimal ink, which did not present shear rate dependence. Jointly, an extrusion-based modular printer head was developed and tested to be compatible with open source 3D printers. Finally, the 3D printed gels were crosslinked to obtain single (SN) and double network (DN) hydrogels. In these latter, a second network precursor of poly(acrylamide) was used. As established, the rheological characterizations constitute a powerful tool to analyze the printability of soft materials.*

4.1 Introduction

Laponite is a nanosilicate commonly applied as a rheology modifier of waterborne products. It is a synthetic additive obtained from salts of sodium, magnesium, and lithium with sodium silicate. It has a layered structure, and when dispersed in water, it forms disk-like particles with approximately $1\ nm$ in thickness and $25\ nm$ in diameter. It is commonly used as a film-forming agent, emulsifier and gelling agent in surface coatings, cleaners, personal care products, inks, among others (Cummins, 2007; Perkins *et al.*, 1974). Laponite has high purity, it is non-toxic and enhances biological activities like cell adhesion and proliferation (Ghadiri *et al.*, 2013a). On the other hand, sodium alginate is a natural polysaccharide; specifically, it is an amorphous copolymer with a linear unbranched chain composed of mannuronic (M) and gulu-

‡ The original publication is available at The International Journal of Advanced Manufacturing Technology https://doi.org/10.1007/s00170-018-2876-y, (Dávila & d'Ávila, 2018)

ronic (G) acids. It is frequently used as a gel-former in different industrial applications (Ertesvåg & Valla, 1998; Fu *et al.*, 2011). The combination of these materials, starting from aqueous solutions, allows obtaining a pronounced shear-thinning behavior. This fact is of great interest in additive manufacturing applications. Moreover, the rheological behavior of these mixtures is strongly influenced by the alginate concentration. The interactions generated between the anionic alginate and the charged surfaces of the Laponite platelets hinder the effect of Laponite at high alginate concentrations (Dávila & d'Ávila, 2017). Then, the composition should be carefully defined in order to dispense the material accurately and to obtain a good printing fidelity.

Different approaches have been proposed to produce inks for AM. Then, rheological studies are fundamental in this field. A shear-thinning behavior is desirable because an inadequate viscosity hampers the formation of filaments and the deposition of the material. Therefore, the deposited structures can easily collapse, regarding that the printing accuracy increases as a function of the viscosity (Malda *et al.*, 2013). Barry *et al.* (2009) developed acrylamide-based inks to fabricate hydrogels by the direct-write assembly technique. The rheological properties of the inks were studied to obtain a satisfactory viscosity and to monitor the polymerization process. Duan *et al.* (2013) fabricated alginate/gelatin inks to encapsulate cells and to produce 3D bioprinted heart valves. Bakarich *et al.* (2013) obtained ionic-covalent hydrogels. The rheological behavior of the hydrogel precursor was evaluated to determine the suitability for extrusion printing. The inks with a low consistency index were not suitable for the additive manufacturing process due to unacceptable sagging and deposition of the material. Larsen *et al.* (2015) studied the rheological behavior of an injectable alginate system. An internal gelation method was applied to crosslink alginate chains. Boere *et al.* (2015) developed inks consisting of a thermoresponsive polymer and poly(ethylene glycol) or a hyaluronic acid crosslinker. In this case, the ink was partially crosslinked, which was completely crosslinked after the bioprinting process. Xavier *et al.* (2015) developed nanoengineered hydrogels using Laponite to obtain higher viscosities, which provides injectability to the ink. Ahlfeld *et al.* (2017) developed a bio-ink using alginate, methylcellulose, and Laponite to obtain scaffolds with good printing fidelity.

Other approaches to overcome the rheological limitations include the use of a soft material as a support, which also allows fabricating samples of complex shapes. Bhattacharjee *et al.*

(2015) developed a granular gel medium to provide additional support for the ink during the printing process. Gentle agitation can easily remove the support bath. Similarly, Hinton *et al.* (2015) used a thermoreversible support bath of gelatin microparticles, which can be removed by heating the printing media at $37\ ^{\circ}\mathrm{C}$. Furthermore, Markstedt *et al.* (2015) used nano-fibrillated cellulose with alginate to obtain a shear-thinning behavior to bioprint living soft tissue. Yang *et al.* (2017) fabricated 3D printed double network (DN) hydrogels with mechanical properties greater than those of cartilage. They used a two-step method in which UV light crosslinked each network.

As previously detailed, different approaches have allowed overcoming limitations related to the hydrogel precursor properties. Moreover, the crosslinking mechanisms can be controlled to guarantee a better accuracy of the morphology and to fabricate DN hydrogels. These latter emerge as an innovative choice to enhance the mechanical properties, which are improved due to the formation of interpenetrating networks. In this kind of materials, the first network is rigid and brittle and the second soft and ductile. As a result of the combination of these characteristics, DN hydrogels are stiff and ductile because the energy dissipation contributes to toughen the material (Nonoyama & Gong, 2015; Shin *et al.*, 2012).

This research describes the rheological evaluation of Laponite/alginate inks to define an appropriated methodology to characterize and obtain printable inks. A 3D extrusion-based printing head was developed and tested using the optimal Laponite/alginate composition. This latter was used as the first network of a DN system. The second network is poly(acrylamide) (PAAm), a non-resorbable bio-inert material widely used in biomedical applications. Then, Laponite/alginate-PAAm double network hydrogels were obtained through an ionic-covalent two-step method. The results here reported provide a viable route to define the region of printability and to crosslink the printed materials to obtain single and double network hydrogels.

4.2 Experimental

4.2.1 Material

Medium-viscosity sodium alginate from brown algae (the molar mass ranges between $80{,}000$ and $120{,}000$ $g\ mol^{-1}$ and the M/G ratio is 1.56), acrylamide (AAm), the crosslinker N,N'-methylenebisacrylamide (MBAA) and the photoinitiator 2-hydroxy-4'-(2-hydroxyethoxy)-2-methylpropiophenone (Irgacure D-2959) were purchased from Sigma-Aldrich Corp., USA. Laponite XLG was obtained from Southern Clay Products, Inc., USA. Anhydrous calcium chloride $(CaCl_2)$ was purchased from Inlab, Brazil.

4.2.2 Hydrogel precursors formulation

The first network precursor is a mixture of Laponite and alginate. Initially, Laponite was dispersed in deionized water (Type II, conductivity $< 1\ \mu S\ cm^{-1}$) using a vortex agitator. Next, alginate was added and dissolved using a magnetic stirrer with a plate temperature of $60\ ^{\circ}\mathrm{C}$. Then, mixtures were stirred in a vortex agitator to ensure homogeneity. The Laponite concentration was varied from 1 to $6\ wt.\%$ and the alginate concentration was fixed at $1\ wt.\%$. Afterward, the Laponite concentration was fixed at $6\ wt.\%$ and alginate varied from 0.5 to $2.5\ wt.\%$. The best composition was determined by rheological studies, the filament formation test by optical microscopy and printability tests. The second network precursor is an AAm solution containing calcium ions to crosslink the first network. Then, $20\ wt.\%$ of AAm was dissolved in a $0.1\ M$ $CaCl_2$ aqueous solution with 0.90 or $2.25\ mM$ MBAA. Finally $0.1\ wt.\%$ of photoinitiator was added and dissolved. All procedures for the second network were performed in the dark.

4.2.3 Rheological characterizations

The rheological characterizations were performed using an Anton Paar MCR-102 Modular Compact Rheometer. Tests were conducted at $25\ ^{\circ}\mathrm{C}$ using a plate-plate geometry (PP50-1)

with a $50\ mm$ diameter and a gap of $1\ mm$ unless stated otherwise. A solvent trap was used to prevent water evaporation. To evaluate the printability of the inks, the rheological properties, and the printing process were correlated in three stages: (i) before printing - rest and flow initiation, (ii) during printing - high shear rate in the nozzle tip walls and (iii) after printing - viscosity recovery. Before printing the material is resting. At this moment, high viscosity and a solid-like behavior guarantee that the flow will be generated only under the application of external forces. Hence, it is desirable a strong shear-thinning viscosity profile. During printing, the material should be capable to flow through the nozzle tip easily, a transition from the solid-like behavior to liquid-like should occur as a function of the strain magnitude. The flow point defines this transition. At this stage, the shear-thinning behavior allows reaching low viscosities when the material is being dispensed. After printing, the object should retain its shape. Therefore, a viscosity recovery is fundamental when the material is already deposited on the platform of the 3D printer. The thixotropic behavior is ideal for this case. Besides, a solid-like behavior is also desirable to avoid the material collapse.

Then, viscosity measurements were carried out in the range of 0.01 to $700\ s^{-1}$ after a constant pre-shear of $200\ s^{-1}$ applied for $300\ s$ followed by a rest period of $300\ s$. Amplitude sweep tests were performed at a constant angular frequency of $10\ rad\, s^{-1}$ with a shear strain in the range from 0.01 to 100%. With the results of this test was defined the linear viscoelasticity (LVE) range ($\gamma_0 = 1\%$ for the inks and $\gamma_0 = 0.5\%$ for the crosslinked hydrogels) and the flow point for the solid-like samples. This point is defined by the crossover where the storage (G') and loss (G'') moduli are equal. Next, frequency sweep tests were performed for the inks and in the crosslinked samples (disc shape hydrogels were 3D printed with $50\ mm$ in diameter and $2\ mm$ in thickness) in the range of 0.1 to $240\ rad\, s^{-1}$. Viscosity recovery tests were carried out to analyze the structure recovery after a shear load (Peak *et al.*, 2017). To simulate the 3D printing conditions, the viscosity recovery test was carried out using three intervals. In the rest interval a low shear rate $(1\ s^{-1})$ was applied for $25\ s$. Then, a constant high shear rate (50-$700\ s^{-1}$) was suddenly applied for $50\ s$. The regeneration interval was carried out with a shear rate of $1\ s^{-1}$ for $250\ s$. The viscosity recovery percentage is given by

$$\eta_{rec} = \frac{\eta_{t_{rec}}}{\eta_i} \times 100 \tag{4.1}$$

where $\eta_{t_{rec}}$ is the viscosity at a recovery time t and η_i is the initial viscosity at the rest interval. All rheological characterizations were triplicated. In Fig. 4.1 is shown the flowchart for the inks printability evaluation.

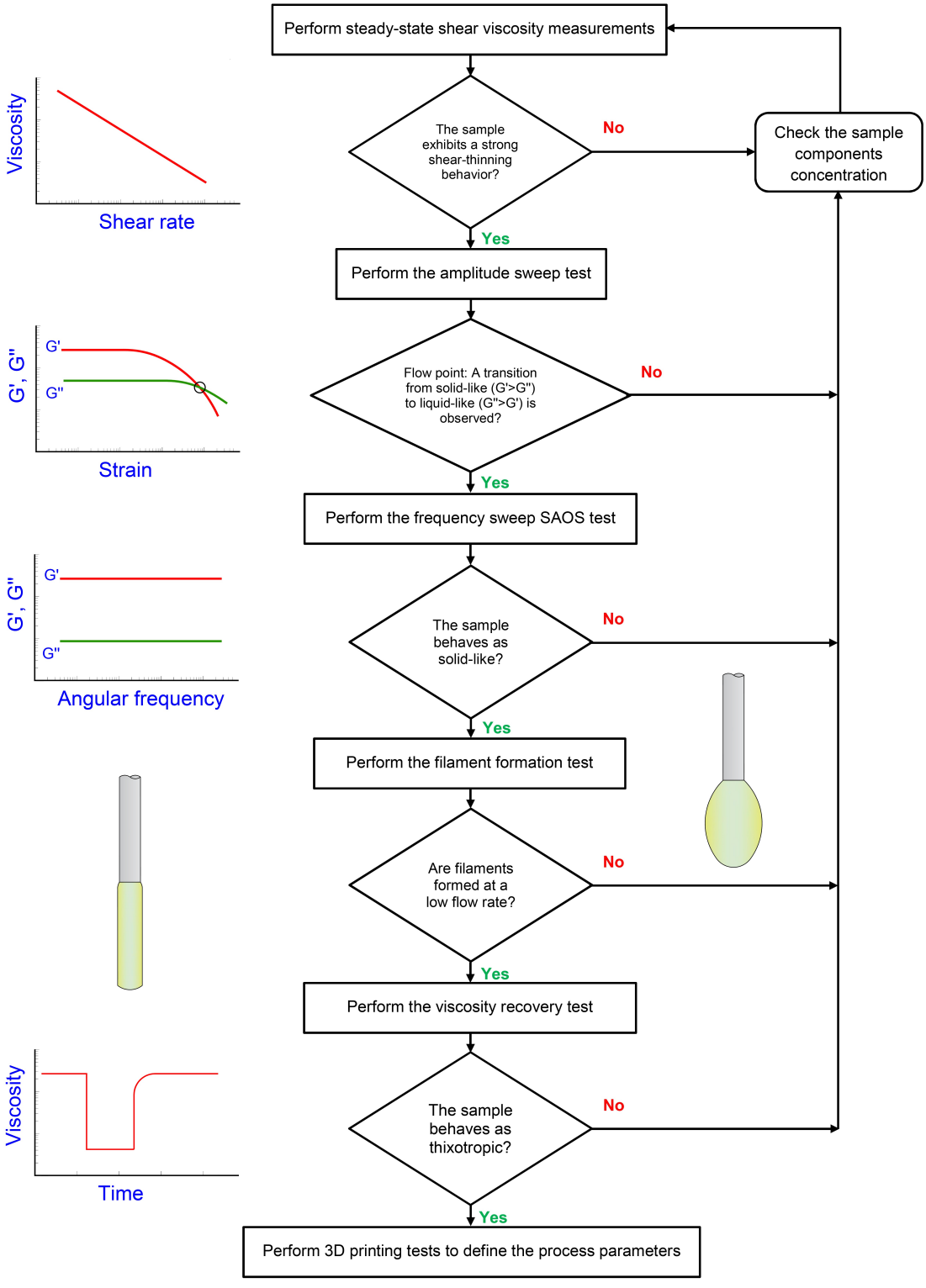

Fig. 4.1: Flowchart of the printability evaluation.

4.2.4 Zeta potential

The zeta potential was measured in a Malvern Zetasizer Nano series equipment. The samples were previously diluted and sonicated for 5 min. All measurements were done in triplicate.

4.2.5 Design of the extrusion-based modular 3D printing head*

The extrusion-based modular printer head is shown in Fig. 4.2. It was planned to be compatible with open source 3D printers controlled by the Marlin firmware working with RAMPS1.4/Arduino electronics.

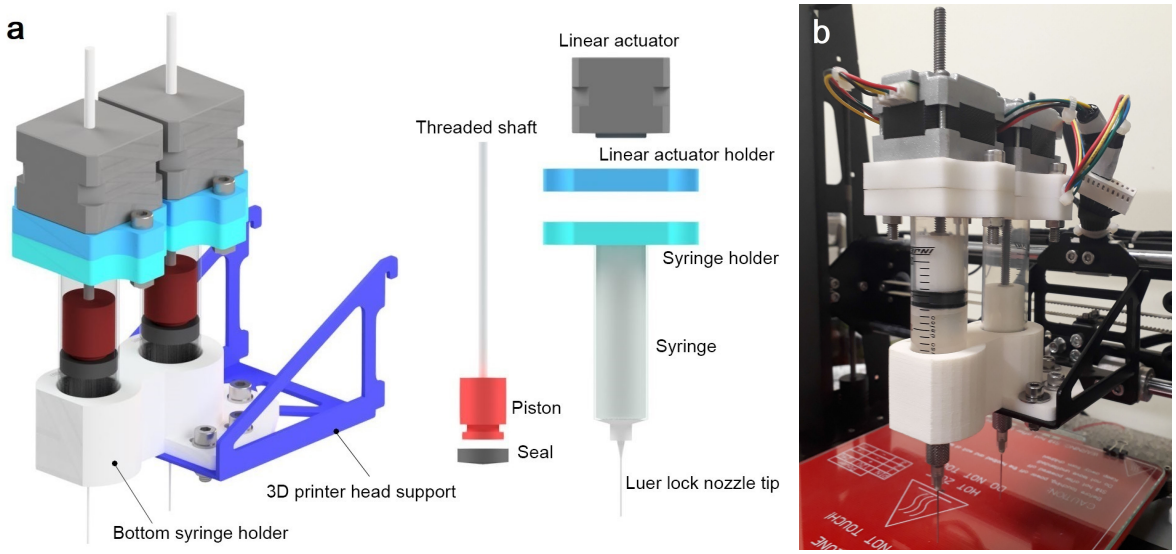

Fig. 4.2: Modular system for 3D extrusion-based printing: (a) computer-aided design (CAD) and (b) photo of the printer head mounted in the 3D printer.

The system uses a linear actuator stepper motor (per module) controlled by the A4988 stepper driver. The linear actuator resolution is $0.01\ mm\ step^{-1}$ with a $1.8°$ step angle. The microstepping resolution was defined to obtain sixteenth steps $(1/16)$. As a result, the system resolution is $1/1600\ mm\ step^{-1}$. The internal diameter of the disposable syringe used is $22\ mm$, therefore, the extruded volume resolution is $2.376 \times 10^{-4}\ ml\ step^{-1}$. The Marlin firmware was modified to allow two extruders and the system is compatible with open source

* Patent INPI BR 10 2017 025903 0, *Sistema modular para impressão 3D de géis*, (Dávila *et al.*, 2017)

software's as Repetier-Host, MatterControl, Cura, Slic3r, Pronterface, among others. In Appendix B are attached the results for the extrusion tests, which were performed to determine the force required to dispense the material.

4.2.6 Filament formation test

The filament formation was examined using an optical microscope coupled to the 3D printing head. The software Repetier-Host V2.1.3 was used to generate a piston speed of $0.526\ mm\ min^{-1}$ (flow rate of $0.2\ ml\ min^{-1}$). In this test, a small flow rate guarantee that the filament is formed due to the material properties and not due to a high flow rate. The extrusion was realized through a 22G nozzle tip of $25\ mm$ in length purchased from Injex, Brazil.

4.2.7 3D printing and hydrogels crosslinking

Initially, the 3D extrusion-based printing head was tested using the optimal Laponite/alginate ink. Piston speeds of 0.526, 1.052 and $1.578\ mm\ min^{-1}$ and printing speeds in the range from 10 to $30\ mm\ s^{-1}$ were tested using the software Repetier-Host V2.1.3. The g-code files containing the printing paths were generated using the software BioScaffoldsPG (Dávila *et al.*, 2016). All samples were centrifuged at $4000\ rpm$ for $5\ min$ in a Kasvi K14-4000 centrifuge to eliminate air bubbles before printing. Then, one layer of material was deposited (using a dosing distance of $0.24\ mm$) and subsequently observed in a stereo microscope Olympus SZ-CTV. The width of the deposited material was measured using the software ImageJ. Furthermore, samples with $1\ wt.\%$ of alginate and different concentrations of Laponite were tested to illustrate the effect of the composition over the process. A hollow hexagon was fabricated at a printing speed of $10\ mm\ s^{-1}$ and a piston speed of $0.526\ mm\ min^{-1}$. Additionally, scaffolds with the number of layers in the range from 10 to 100 were fabricated to validate the material and the printing head.

After 3D printing, the ionic and ionic-covalent crosslinking were performed for single (SN) and double (DN) network hydrogels respectively. The ionic crosslinking was realized

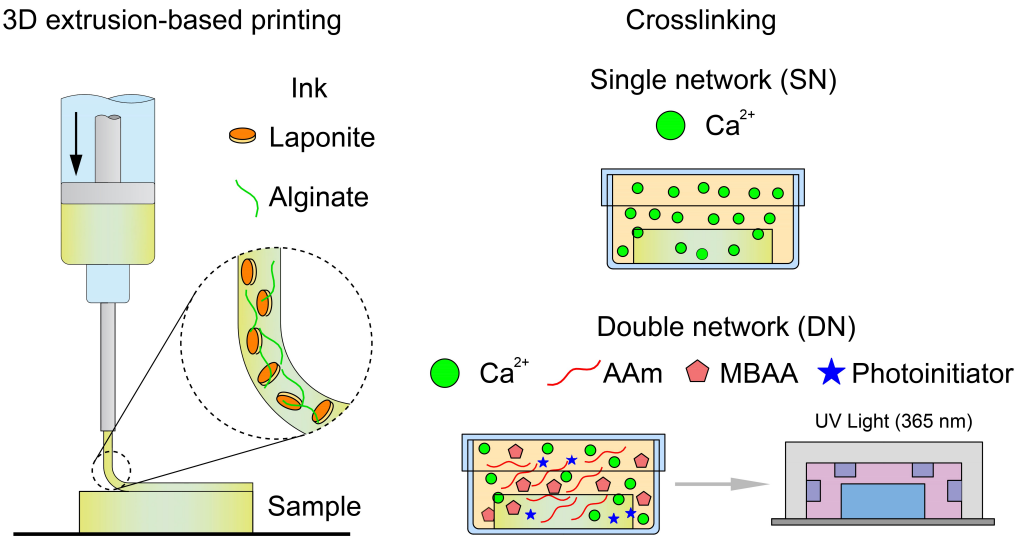

Fig. 4.3: Synthesis scheme of the 3D printed single (SN) and double network (DN) hydrogels.

immersing the printed samples in a $0.1\ M\ CaCl_2$ aqueous solution for $24\ h$. For the ionic-covalent crosslinking the samples were immersed in the second network precursor for $24\ h$. The schematic procedure is illustrated in Fig. 4.3. The calcium ions crosslink the G groups of alginate forming an egg-box structure. Moreover, in DN hydrogels the AAm monomer, the MBAA and the photoinitiator diffuse in the Laponite/alginate network. In this case, the sample was removed from the solution and washed in deionized water. The water excess was removed using a paper towel. The samples were crosslinked in a UV chamber of $365\ nm$ wavelength and $36\ W$ for $30\ min$. Hydrogels were soaked in deionized water for at least $72\ h$ to remove the unreacted photoinitiator for further characterizations. The deionized water was replaced once per day.

4.2.8 Fourier transform infrared spectroscopy (FTIR)

The chemical structure of alginate, Laponite and single and double network hydrogels was analyzed by FTIR. The attenuated total reflectance (ATR) mode was applied using an Agilent Cary 630 FTIR spectrometer. Hydrogels were lyophilized before tests. The transmittance was evaluated over the wavenumber range of 4000 - $450\ cm^{-1}$.

4.2.9 Mechanical characterization

The mechanical properties were analyzed by compression test using a universal testing machine MTS (Model 810-FlexTest 40) equipped with a $1500\ N$ load cell. A constant strain rate of $1\ mm\ min^{-1}$ was applied to five fully hydrated 3D printed samples of $10\ mm$ in diameter and $15\ mm$ in height. The test was performed up to 90% strain.

4.3 Results and discussion

4.3.1 Rheology and printability of the first network

In this chapter is presented the rheological optimization of Laponite/alginate inks for 3D extrusion-based printing. Previously, it was demonstrated that Laponite significantly enhances the shear-thinning behavior of aqueous alginate solutions (Dávila & d'Ávila, 2017). Laponite XLG is a gel grade layered silicate capable of forming low or high viscosity colloidal dispersions. The viscosity profile depends on the electrolyte content of the water used, pH changes and the addition of salts and/or polymers (Peak *et al.*, 2017). Laponite platelets develop electrostatic interactions with polymers; adsorption or desorption depend on the charged sections on the molecules of the polymer. In the system Laponite/alginate a bonding mechanism could be generated between the Laponite platelets and the anionic alginate. Therefore, by varying the components concentration it is possible to obtain custom rheological profiles. Higher alginate concentrations saturate the positive rims of Laponite platelets and affect the shear-thinning and solid-like behaviors (Dávila & d'Ávila, 2017).

The printability of the inks was initially evaluated through steady-state shear viscosity measurements. In Fig. 4.4a are shown viscosity curves for different mixtures and an alginate sample. As observed, the viscosity for the alginate sample exhibits a shear-thinning behavior after a Newtonian plateau. On the other hand, the mixtures containing Laponite platelets exhibit a strong shear-thinning behavior. This latter meet an important requirement for 3D extrusion-based printing: high viscosity at small shear rates and low viscosity at high shear rates. Ac-

cording to Malda *et al.* (2013), a high viscosity impedes the surface tension-driven droplet formation and the collapse of the printed object. In Fig. 4.4b is shown the viscosity at low shear rate ($\dot{\gamma} = 0.01\ s^{-1}$), which is defined by a power-law. As observed, the Laponite platelets significantly increase the viscosity.

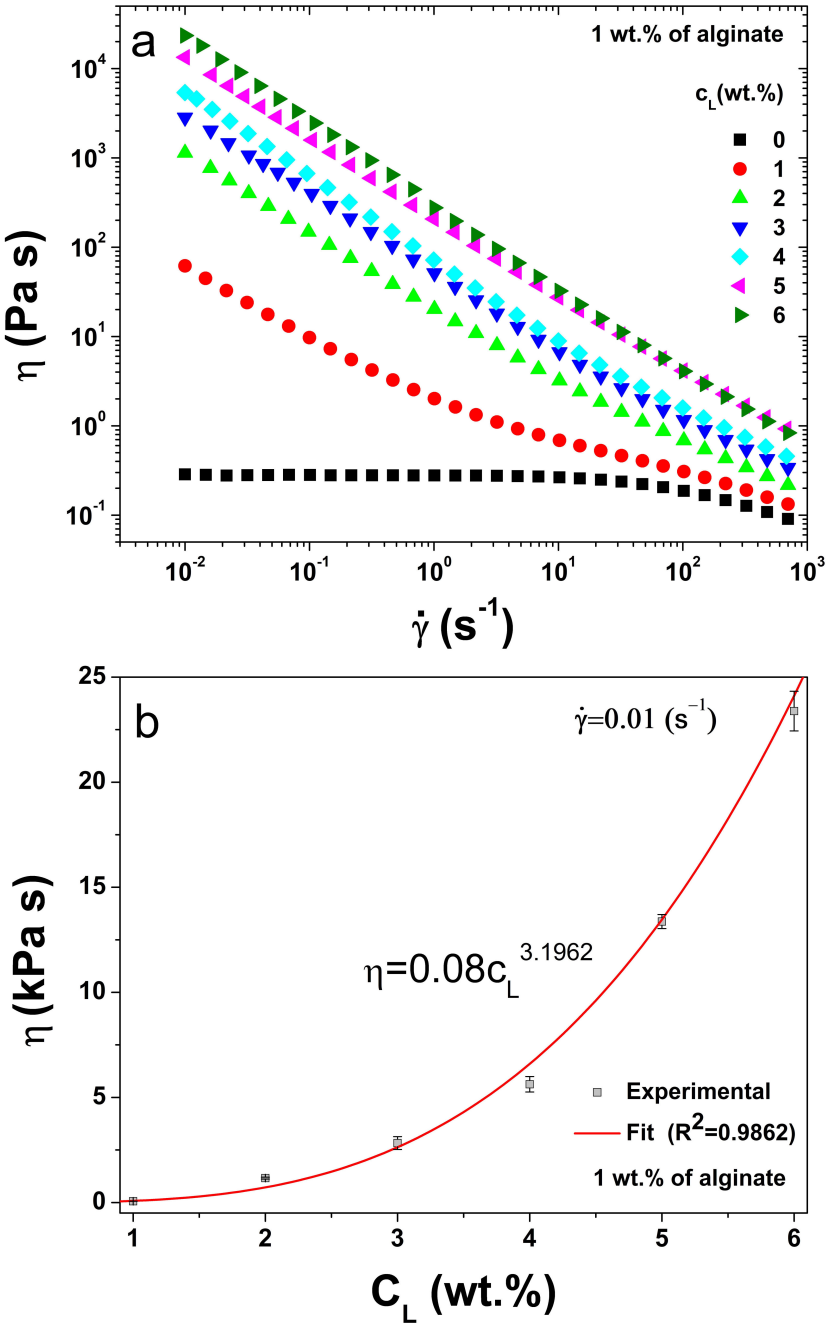

Fig. 4.4: (a) Viscosity (η) as a function of the shear rate ($\dot{\gamma}$) (c_L is the Laponite concentration and the alginate concentration is $1\ wt.\%$) and (b) low shear rate viscosity as a function of the Laponite concentration.

Next, oscillatory shear tests were performed to analyze the viscoelastic behavior of the inks. In Fig. 4.5a are shown the amplitude sweep results. At a constant angular frequency of

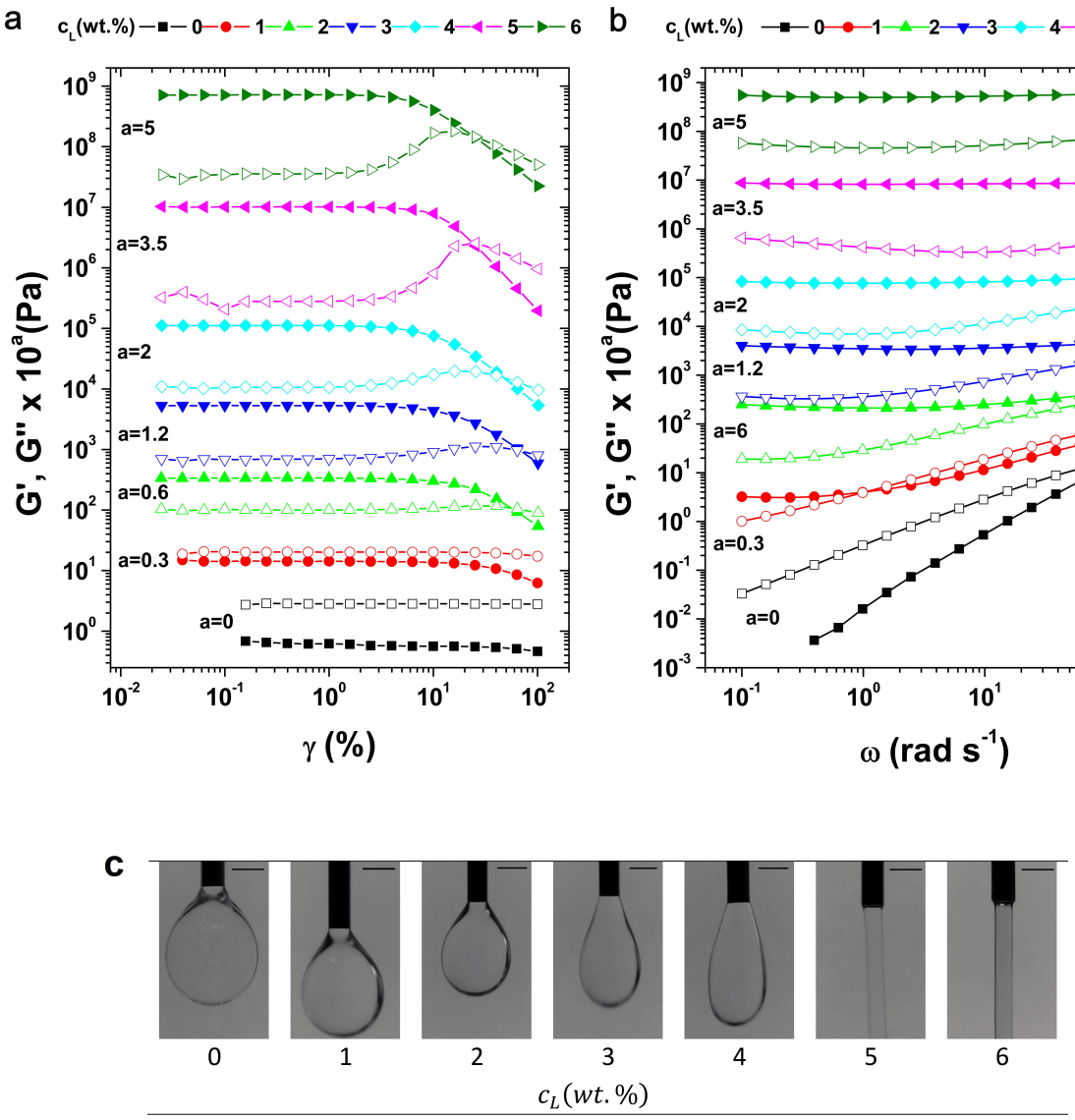

Fig. 4.5: Storage modulus (G') (solid symbols) and loss modulus (G'') (open symbols) as a function of the: (a) strain (γ) and (b) angular frequency (ω). Data are vertically shifted to avoid overlapping (c_L is the Laponite concentration and the alginate concentration is $1\ wt.\%$), (c) optical microscopy images showing the extrusion of a mixture containing $1\ wt.\%$ of alginate and different Laponite concentrations. The scale bar represents $1\ mm$.

$10\,rad\,s^{-1}$, the alginate solution behaves as liquid-like. This behavior is also experienced by the mixture containing $1\ wt.\%$ of Laponite. Contrariwise, Laponite concentrations above $2\ wt.\%$ behave as solid-like, which would be associated with the physical gelation generated between the Laponite platelets and the alginate chains. For these mixtures, the flow point is clearly observed. This point guarantees the flow initiation during the printing process, which is associated with the transition from the solid-like to liquid-like behavior at the crossover strain. Furthermore, in Fig. 4.5b are shown the frequency sweep results. It is corroborated that the alginate

sample behaves mainly as liquid-like. Nonetheless, a crossover point defines a transition to the solid-like behavior. This could be associated with the longer alginate chains, which cannot completely disentangle at high frequencies (Yu *et al.*, 2014). For the sample containing $1\ wt.\%$ of Laponite, a solid-like behavior is observed at small frequencies. On the other hand, the samples above $2\ wt.\%$ of Laponite behave as solid-like in all the range analyzed. These samples apparently have suitable properties for 3D extrusion-based printing. Then, the filament formation during extrusion was also evaluated to guarantee that the material could be dispensed in layers. As observed in Fig. 4.5c, a continuous filament is only formed above the $5\ wt.\%$ of Laponite concentration.

Next, the Laponite concentration was fixed at $6\ wt.\%$ and the viscosity profile was analyzed for different alginate concentrations. The viscosity curves are shown in Fig. 4.6a. As observed, the viscosity increases when alginate is added, nonetheless, higher concentrations of alginate partially hinder the rheology modifier effect of Laponite due to electrostatic interactions (Dávila & d'Ávila, 2017). The zeta potential shown in Fig. 4.6b is one of the factors that define the rheological properties and the stability of dispersions. For Laponite, the zeta potential is around $-38.9\ mV$. In the presence of alginate, the negative magnitude of the zeta potential increases, this would be associated with the presence of anionic charges and the alginate adsorption. Above an alginate concentration of $1.5\ wt.\%$, the negative magnitude of the zeta potential decreases, suggesting a reduction in the stability of the dispersion. This fact corroborates the decrease in the low shear rate viscosity. As reported by Yang *et al.* (2017) the viscosity of a mixture containing Laponite is significantly affected by the changes in the ionic strength. The viscosity curves fitted well with the Ostwald-de Waele viscosity model, which is given by

$$\eta(\dot{\gamma}) = m\dot{\gamma}^{n-1} \tag{4.2}$$

where m is the consistency index and n the power-law index; m is associated with magnitude of the viscosity and n defines the viscosity behavior: (i) shear-thickening if $n > 1$, (ii) Newtonian if $n = 1$ or (iii) shear-thinning if $n < 1$ (Morrison, 2001). In Table 4.1 is observed that n increases with the alginate concentration for all the cases. Nevertheless, the consistency index reaches a maximum with $1.5\ wt.\%$ of alginate and then decreases significantly.

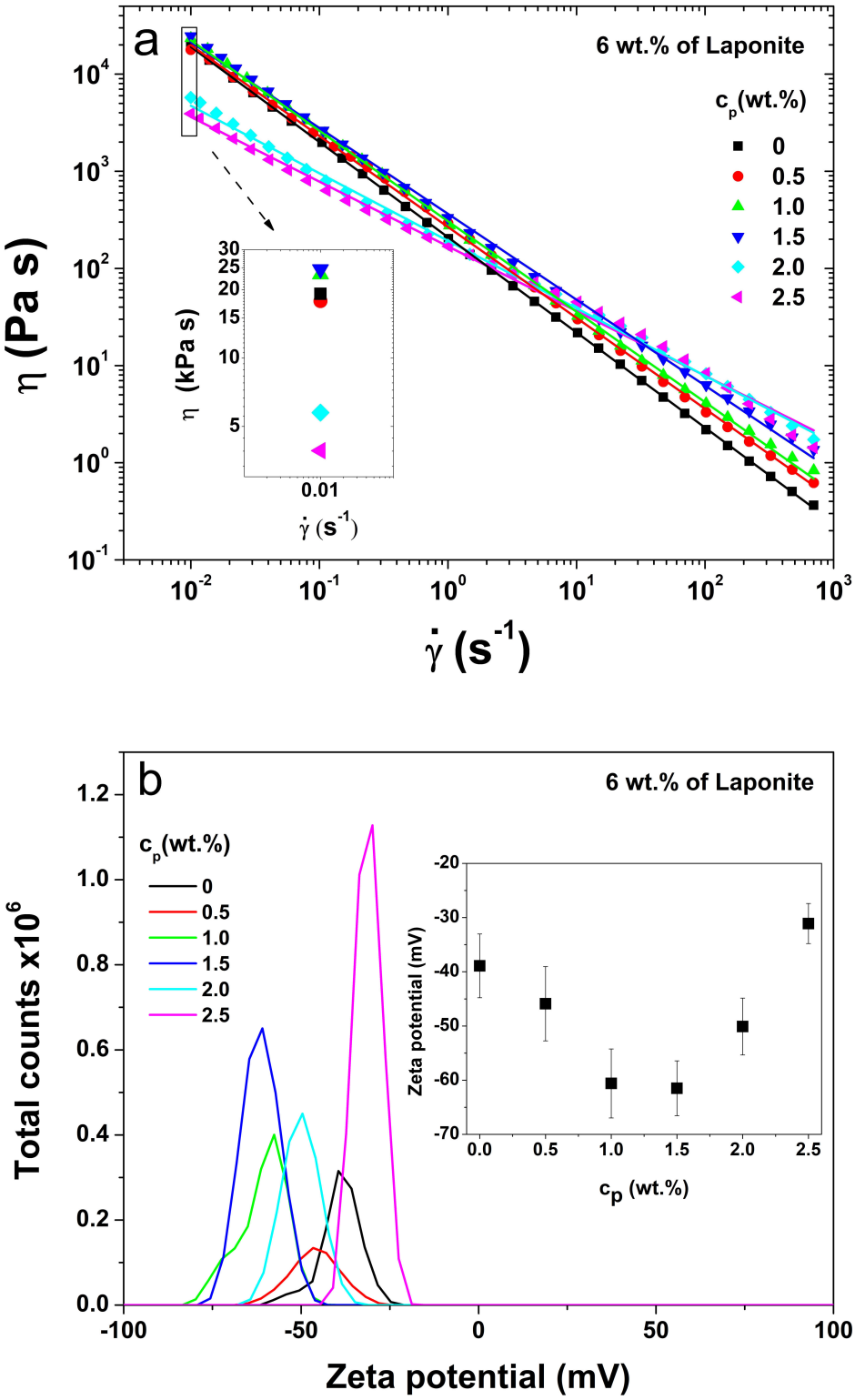

Fig. 4.6: (a) Viscosity (η) as a function of the shear rate $(\dot{\gamma})$ for Laponite/alginate mixtures (c_p is the alginate concentration) and (b) zeta potential; the inset plot depicts the zeta potential as a function of the alginate concentration.

Table. 4.1: Ostwald-de Waele viscosity model fitting parameters ("A" represents the alginate concentration).

Sample	$m\ (Pa\ s^n)$	$n\ (-)$	R^2
0A	209.31 ± 15.44	0.020 ± 0.0024	0.9999
0.5A	267.50 ± 11.44	0.064 ± 0.0002	0.9996
1.0A	305.85 ± 11.55	0.069 ± 0.0020	0.9995
1.5A	364.97 ± 7.80	0.116 ± 0.0017	0.9990
2.0A	192.78 ± 10.14	0.305 ± 0.0250	0.9982
2.5A	168.69 ± 13.96	0.334 ± 0.0270	0.9949

The composition for the optimal ink was defined as $6\ wt.\%$ of Laponite and $1\ wt.\%$ of alginate, in which m and n ensure an appropriate viscosity to dispense the material. Up to this alginate concentration mixing the components did not present difficulties. In the case of concentrations above $1\ wt.\%$ of alginate, a longer time in the vortex stirrer was required to solubilize it completely. Throughout the literature, it has been reported suitable consistency and power-law indexes for different inks and bio-inks. Bakarich *et al.* (2013) reported consistency indexes in the range from 20 to $150\ Pa\ s^n$ and power-law indexes between 0.32 and 0.45 for alginate-acrylamide inks, where ethylene glycol was used as a rheology modifier. In another study, the same research group fabricated 3D printed fiber reinforced hydrogel composites using an Epoxy based UV curable adhesive (Emax 904 Gel-SC), an alginate-ethylene glycol ink as support and an alginate-acrylamide ink. Consistency indexes of 41, 50 and $80\ Pa\,s^n$ and power-law indexes of 0.44, 0.38 and 0.37 were reported for the Emax, the support ink and the alginate-acrylamide ink respectively (Bakarich *et al.*, 2014). Peak *et al.* (2017) defined an optimal ink containing PEG ($10\%\ wt./vol$) and Laponite ($4\%\ wt./vol$). The consistency and the power-law indexes are $60\ Pa\ s^n$ and 0.2 respectively. In contrast, our optimal ink has a higher consistency index of approximately $306\ Pa\ s^n$ and a power-law index of 0.069, which defines a strong shear-thinning profile.

The results for the viscosity recovery test are presented in Fig. 4.7. It can be observed that the ink needs a short time to recover the initial structure. When the material flows through the nozzle tip, Laponite platelets and alginate chains tend to become oriented in the flow direction.

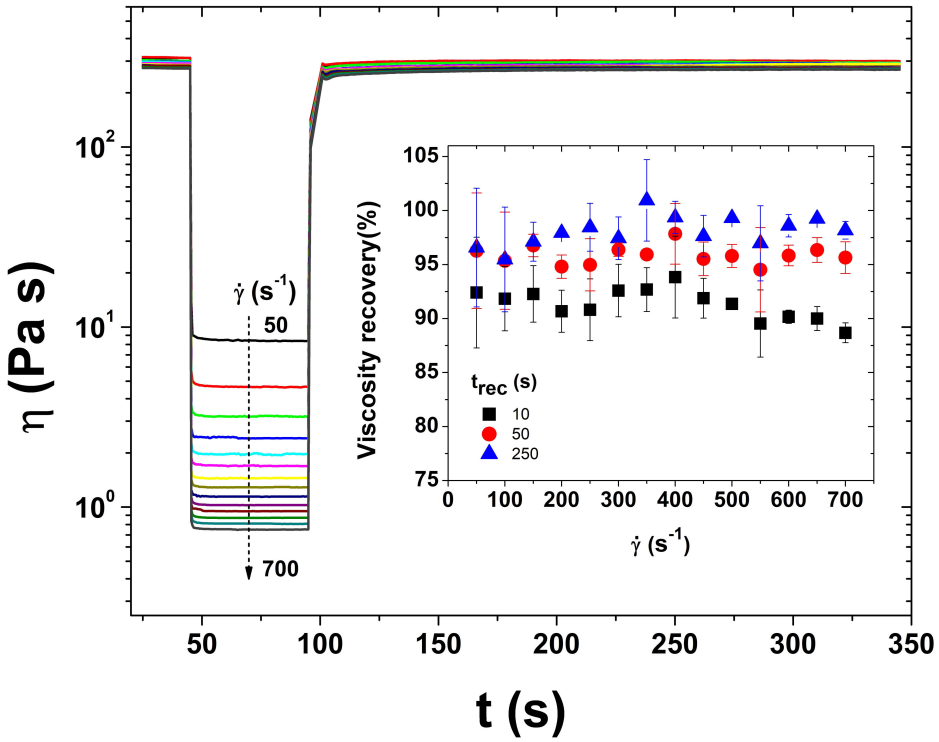

Fig. 4.7: Viscosity (η) as a function of the time (t) for the recovery test. The shear rate $(\dot{\gamma})$ increases from 50 to 700 s^{-1}. The inset plot depicts the viscosity recovery percentage (η_{rec}) as a function of the shear rate.

Then, the viscosity decreases and stays constant in the load interval. When the high shear load is removed, the viscosity recovery occurs almost instantaneously, which would be associated with the regeneration of the house of cards structure and the elastic energy stored by the alginate chains. According to our findings, the viscosity recovery has no dependence on the shear rate undergone during the process. Statistical significance was determined by one-way ANOVA $(p < 0.05)$. The viscosity recovery is around 90% after $10\ s$. This capability to quickly rebuild the structure is ideal to increase the stability of the printed object, what in turn improves the printing quality. After $250\ s$ the viscosity recovery is in the range between 95 and 100%. Peak *et al.* (2017) reported that an initial viscosity recovery of 80% is significant for 3D printing.

4.3.2 3D extrusion-based printing

According to the power-law generalized Newtonian fluid, the velocity profile along a tube (nozzle tip) is defined by (Morrison, 2001)

$$v_z\left(r\right) = R^{\frac{1}{n}+1}\left(\frac{\Delta p}{2mL}\right)^{\frac{1}{n}}\left(\frac{n}{n+1}\right)\left[1-\left(\frac{r}{R}\right)^{\frac{1}{n}+1}\right] \tag{4.3}$$

where Δp is the is the pressure difference between the inlet and outlet of the nozzle tip (extrusion pressure), r is the radial coordinate and R and L the nozzle tip radius and length respectively. The flow rate is given by (Morrison, 2001)

$$Q = \left(\frac{\Delta pR}{2mL}\right)^{\frac{1}{n}}\left(\frac{n\pi R^3}{1+3n}\right) \tag{4.4}$$

and the wall shear rate (Macosko, 1994)

$$\left.\frac{\mathrm{d}v_z}{\mathrm{d}r}\right|_R = \dot{\gamma}_w = \frac{4Q}{\pi R^3}\left(\frac{3}{4}+\frac{1}{4n}\right) \tag{4.5}$$

The nozzle tip diameter influences over the shear rate. For higher nozzle tip diameters, the wall shear rate decreases while the printing viscosity increases. On the other hand, small nozzle tip diameters require a higher pressure to dispense the material. With a high length nozzle tip, the material has more time to align in the flow direction, which benefits the material dispensing. As shown in Fig. 4.8a, the extrusion velocity profile inside the nozzle tip is flat, which is directly associated with the strong shear-thinning behavior of the ink. In Fig. 4.8b is observed that the wall shear rate increases significantly as a function of the piston speed. Hence, the printing viscosity decreases and the material can be readily dispensed. Then, the extrusion and printing speeds directly influence over the material deposition. In Fig. 4.8c is illustrated the filament width obtained after measurements of printed samples under different conditions. The ratio between the extrusion and the printing speeds should be appropriated to deposit the material continuously. For a low extrusion speed and a high printing speed, the material will be stretched, and the width of the deposited line will be lower. In some cases, the material deposition could be interrupted. Contrariwise, for high extrusion speeds and small printing speeds, the filament width will be higher. Therefore, taking into account the mass conservation, it is desirable that the extrusion speed must be higher than the printing speed.

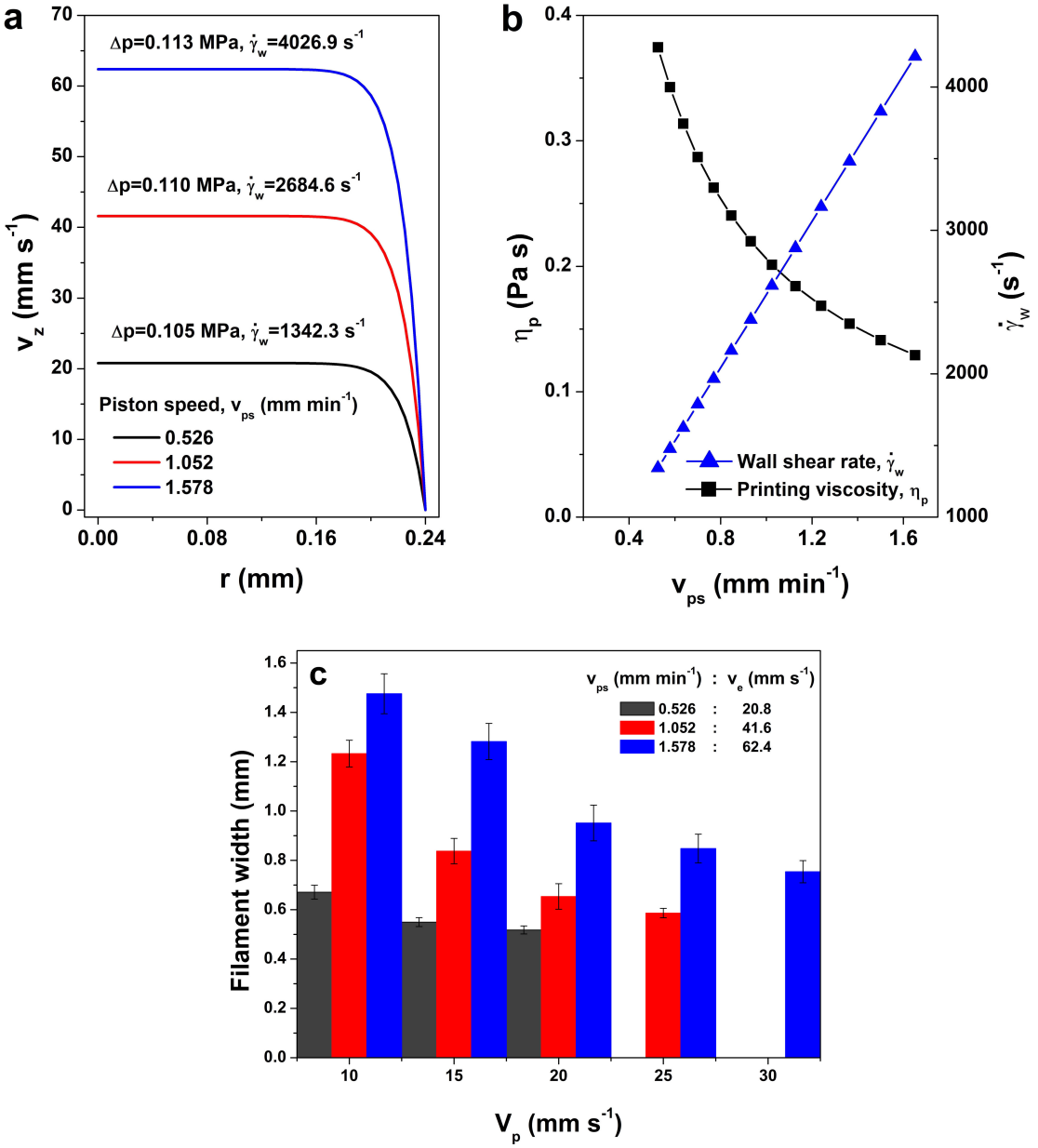

Fig. 4.8: Printing parameters for the optimal ink: (a) extrusion velocity profile inside the nozzle tip, (b) printing viscosity (η_p) and wall shear rate $(\dot{\gamma}_w)$ as a function of the piston speed (v_{ps}) and (c) filament width as a function of the printing speed (v_p) for different extrusion speeds (v_e).

Afterward, printing tests were performed with different Laponite concentrations. As shown in Fig. 4.9(a,b), it was possible to correctly dispense the material with a Laponite concentration of at least $5\ wt.\%$. With $3\ wt.\%$ of Laponite the printed structure collapsed and after the first layers it was no longer possible to dispense the material continuously. The shape fidelity increased as a function of the Laponite concentration. Then, scaffolds were printed with the optimal ink using different numbers of layers. As illustrated in Fig. 4.9(c-g), the material

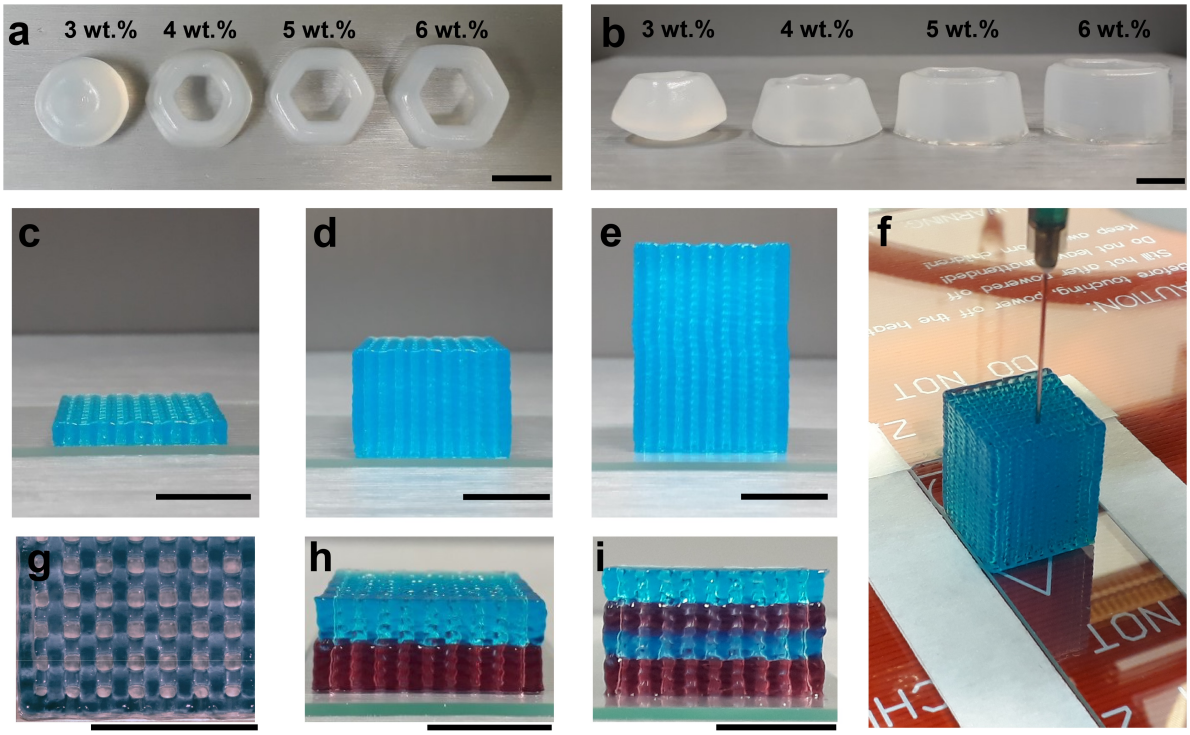

Fig. 4.9: Printed samples: (a,b) influence of the Laponite concentration over the printability, (c) 10 layers scaffold, (d) 50 layers scaffold, (e) 100 layers scaffold, (f) sample during the printing process, (g) scaffold superior view, (h) 30 layers scaffold using two extruders, each extruder printed 15 layers in two intervals, (i) 40 layers scaffold, each extruder print 10 layers in four intervals. Food coloring was used to identify the extruder 1 (blue) and the extruder 2 (red). Scale bars represent 10 mm.

was continuously dispensed. Once deposited in the platform, the viscosity recovery and the solid-like behavior guarantee the printing stability. In these tests was used an extrusion speed of 41.6 $mm\,s^{-1}$, a printing speed of 15 $mm\,s^{-1}$ and a layer height 0.24 mm. A video file showing the fabrication of a 100 layers scaffold is available online (electronic supplementary material, https://doi.org/10.1007/s00170-018-2876-y). Subsequently, dual extrusion was performed. As observed in Fig. 4.9(h,i), the material was correctly dispensed. The firmware calibration and configuration works properly after modified. The dual extrusion expands the applications for the use of different materials, which includes the use of a support material.

4.3.3 Hydrogels crosslinking: chemical structure and swelling behavior

In Fig. 4.10 it is observed the FTIR spectra of the powder raw materials and the dried samples of single and double network hydrogels. For the sodium alginate, it is shown the cha-

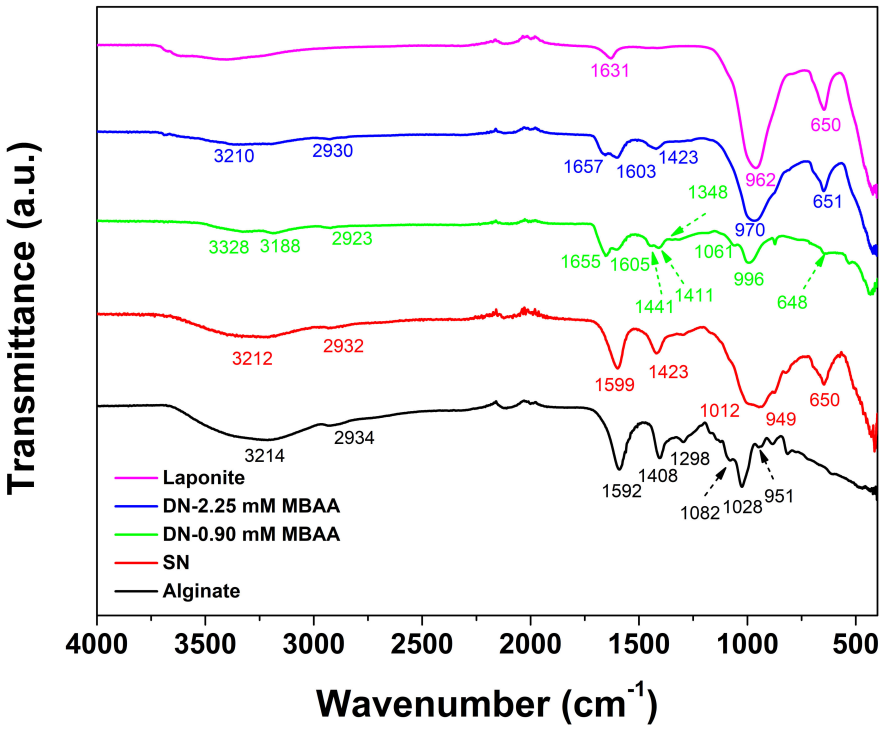

Fig. 4.10: FTIR spectra of alginate, Laponite, and the dried SN and DN hydrogels.

racteristic peaks for this material. The band between 3600 and 3200 cm^{-1} is associated with the stretching vibration of $O-H$ bonds of alginate. At 2934 cm^{-1}, a peak attributed to the overlapping symmetric and asymmetric stretching vibration of $C-H$ aliphatic chains is observed. At 1592 cm^{-1} and 1408 cm^{-1} peaks associated to the symmetric and asymmetric stretching vibration of the $C-O$ bond of COO^{-} can be observed (Li *et al.*, 2008a). At 1298 and 951 cm^{-1}, peaks corresponding to the $C-O$ stretching are observed (Kanti *et al.*, 2004; Mahmoodi, 2013). The peaks at 1082 and 1028 cm^{-1} correspond to the stretching vibrations of the $C-O$ bond of the glycosidic linkage (Voo *et al.*, 2015). In the spectra for the Laponite/alginate dried hydrogel, the peaks of sodium alginate were shifted from 1592 to 1599 cm^{-1} and from 1408 to 1423 cm^{-1} due to the ionic crosslinking with Ca^{2+} ions and the formation of the egg-box structure (Voo *et al.*, 2015). At 1012 cm^{-1} it is observed a peak related to the $Si-O$ stretching of Laponite (Du *et al.*, 2015; Jun *et al.*, 2015). Moreover, the peak corresponding to the $C-O$ stretching of alginate was shifted from 951 to 949 cm^{-1}. The peak at 650 cm^{-1} correspond to the vibration of the $Mg-O$ bond of Laponite (Ghadiri *et al.*, 2013b; Sudha *et al.*, 2011). In the DN hydrogels, it is clearly observed the presence of the first network components. Moreover, in the range from 3400 to 3200 cm^{-1}, peaks associated with the stretching vibration of $N-H$ are observed.

Around $1655\ cm^{-1}$ it can be observed the stretching of the $C = O$ group of the AAm unit (Li *et al.*, 2008b). At approximately $1605\ cm^{-1}$ it is observed the $N - H$ bending vibration of the amide group. The peaks between 1441 and $1411\ cm^{-1}$ would be associated to $C - H$ bending (Şolpan *et al.*, 2008). The peak at $1348\ cm^{-1}$ corresponds to the $C - N$ stretching (Lim *et al.*, 2016). For Laponite it is observed a peak at $1631\ cm^{-1}$ associated to the $H - OH$ bending. At $962\ cm^{-1}$ a peak related to the $Si - O$ stretching and at $650\ cm^{-1}$ the $Mg - O$ vibration (Cai *et al.*, 2016).

The swelling behavior of hydrogels is associated with the crosslinking density (Zhang *et al.*, 2014). The swelling kinetics could be well described by a pseudo-second-order model based on the swelling capacity on solid phase (Li *et al.*, 2017),

$$\frac{t}{Q_t} = \frac{1}{k_2 Q_e^2} + \frac{1}{Q_e} t \tag{4.6}$$

where Q_e is the swelling ratio at the equilibrium and k_2 the rate constant of sorption. Moreover, r_0 is the initial rate of swelling, defined as Q_t/t when $t \to 0$,

$$r_0 = k_2 Q_e^2 \tag{4.7}$$

As shown in Table 4.2 and Fig. 4.11 the swelling ratio at equilibrium is greater for the DN hydrogels. In an initial stage, the group DN-$2.25\ mM$ MBAA presented a faster rate of water absorption, which is reflected in the initial rate of swelling. Nevertheless, after $8\ h$ the group DN-$0.09\ mM$ MBAA starts to present a higher swelling ratio, which would be associated with their lower crosslinking density. On the other hand, for the SN hydrogels it is observed a limited capacity of absorbing water. The swelling ratio is significantly lower than the DN hydrogels. In these latter, the presence of poly(acrylamide), which is highly hydrophilic improves considerably the water absorption.

Table. 4.2: Swelling kinetics parameters.

Sample	$r_0\ (h^{-1})$	$k_2\ (h^{-1})$	$Q_e\ (g\ g^{-1})$	R^2
SN	0.9795	0.811	1.099	0.9837
DN-0.09 mM MBAA	1.2625	0.004938	15.99	0.9952
DN-2.25 mM MBAA	1.3379	0.006381	14.48	0.9900

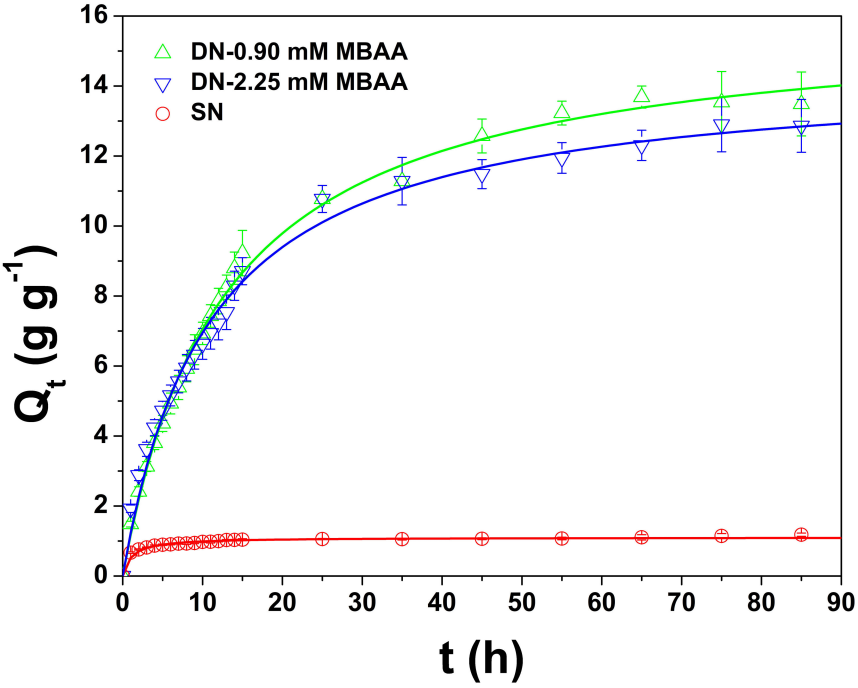

Fig. 4.11: Swelling ratio of single and double network hydrogels in deionized water.

4.3.4 Hydrogels mechanical properties

The mechanical properties of the hydrogels were evaluated by frequency sweep and compression tests. Hydrogels have a viscoelastic behavior defined by the storage (G') and the loss moduli (G''). In Fig. 4.12a it is observed that $G' > G''$ for all cases, which is related with a solid-like behavior. Before the ionic crosslinking, the Laponite/alginate samples behave as a soft gel. The physical gelation generated by the interactions between alginate chains and Laponite platelets allows maintaining the shape after printing. Nonetheless, these interactions are weak and can be easily broken by applying mechanical forces. When the samples are soaked in

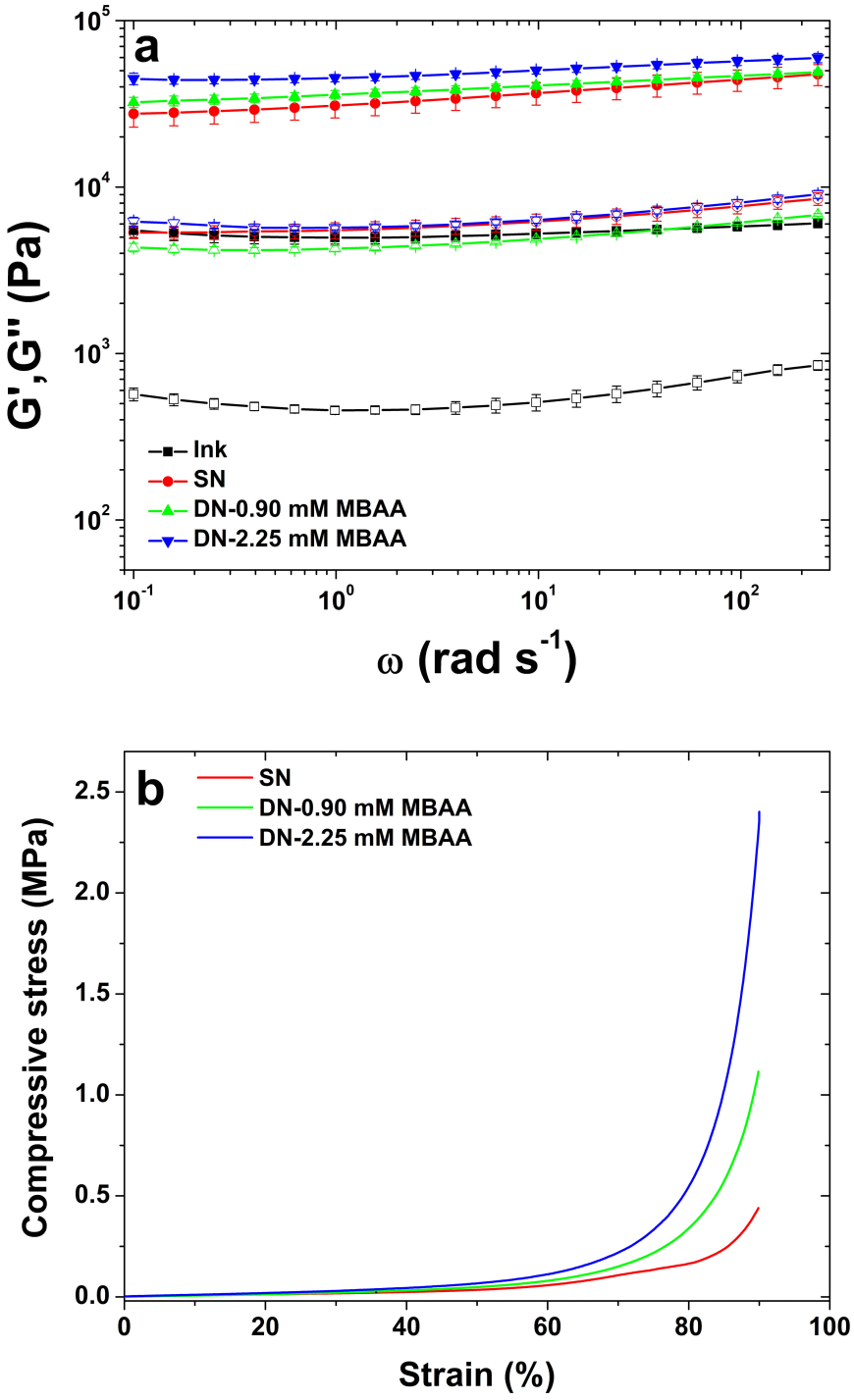

Fig. 4.12: (a) Storage modulus (G') (solid symbols) and loss modulus (G'') (open symbols) as a function of the angular frequency (ω) and (b) compression stress–strain curves.

an aqueous $CaCl_2$ solution, calcium ions diffuse inside the material and crosslink the G blocks of alginate. Junctions are formed between adjacent chains, and an egg-box structure defines a three-dimensional network (Liu *et al.*, 2016). Therefore, G' and G'' increased significantly and the mechanical stability was improved. When the second network is added, an interpenetrating network is formed. The covalent crosslinking generates a chemical hydrogel. As observed, a

higher amount of MBAA is associated with better mechanical properties due to the increase of the crosslinking density. This fact is also observed in Fig. 4.12b. The compressive stress at a strain of 90% increases from $0.44 \pm 0.05\ MPa$ to $1.08 \pm 0.07\ MPa$ for a $0.90\ mM$ MBAA second network. Furthermore, using a $2.25\ mM$ MBAA second network increases the compressive stress to $2.41 \pm 0.28\ MPa$.

The formation of the egg-box structure compacts the alginate network due to the presence of calcium ions, when a compressive load is applied, the crosslinked zones of alginate are unzipped, which contributes to the energy dissipation mechanism (Yang *et al.*, 2013). The ionic interactions are a physical crosslinking and are commonly used to obtain the reversible crosslinking mechanism (Zhao, 2014). To stabilize the deformation, the poly(acrylamide) network was added. Therefore, in the DN hydrogel, each network contributes to dissipate the mechanical energy (alginate) and maintain high elasticity (PAAm). The SN hydrogels presented a permanent deformation after the compression test. On the other hand, the DN network hydrogels have the ability to recover the shape when the compression force is removed.

4.4 Summary

The rheological studies performed in Laponite/alginate mixtures allowed to analyze their viscosity profiles and define an optimal ink for 3D extrusion-based printing. Evaluate the printability is of high importance to set the process parameters and to correctly dispense the material. The Laponite and alginate concentrations have significant influence over the shear-thinning behavior and the printability of the ink. The flow initiation, the fast viscosity recovery after a high shear rate and the solid-like behavior guarantee that the ink is capable of being dispensed and subsequently retain the shape of the printed object. These set of rheological properties analyzed together with the filament formation test allow evaluating the printability. Then, the modular 3D extrusion-based printing head was tested, and single (SN) and double network (DN) hydrogels were successfully crosslinked after the printing process. The chemical structure analyzed by FTIR revealed the ionic crosslinking of alginate and the covalent crosslinking of poly(acrylamide), which together form an interpenetrated network. This fact is reflected in the enhanced mechanical properties evaluated by the frequency sweep test and the compression

test. Finally, future perspectives are oriented to apply the methodology here reported to bio-inks or other biocompatible soft materials to print scaffolds or substitutes for tissue engineering applications with good printing fidelity. Moreover, the system Laponite/alginate could be further studied as the basis to obtain bio-inks.

5 CONCLUSIONS

This work has shown that rheological characterizations constitute a powerful tool to analyze inks for 3D printing. Initially, alginate aqueous solutions were studied. As observed, the anionic behavior was in good agreement with the scaling laws reported in the literature. Then, when the rheology modifier was added, the electrostatic interactions generated with the polymer chains significantly influenced the rheological behavior as a function of the concentration. Alginate could be adsorbed in the positively charged rims of Laponite. In this way, the inks were planned since their initial conception. Transitions from solid-like to liquid-like behaviors were observed and reported, which enabled the appropriate definition of the composition of the inks.

After the initial findings of the rheological behavior of the system Laponite/alginate, different concentrations were evaluated, targeting an optimal ink concentration. Then, taking into account the characteristics of the 3D extrusion-based process, the ink evaluation was realized based on three stages: (i) rest and flow initiation, (ii) high shear rate in the nozzle tip walls, and (iii) retain the shape at rest. This proposal was evaluated by steady-state shear tests, viscosity recovery tests, amplitude sweep, and frequency sweep tests (SAOS). The filament formation was assessed using an optical microscope, and the printability, using different concentrations in the 3D printer. As a result of the consolidation of all these characterizations, a protocol to develop inks for 3D printing was established. All mixtures evaluated exhibited a pronounced shear-thinning behavior. Nonetheless, higher alginate concentrations partially hindered the rheology modifier effect of Laponite. The Ostwald-de Waele viscosity model described well the viscosity curves of the samples. Moreover, it was reported that after a high shear rate, the viscosity is rapidly recovered. This recovery has no dependence on the shear rate undergone during the process.

Jointly with the inks evaluation, was developed a 3D extrusion-based printing head compatible with an open source, RepRap 3D printer. This device is in the technical field of accessories for molding and printing of three-dimensional objects. Specifically, it is a syringe head for the deposition of gels and hydrogels by extrusion generated by a piston system. This printing head was planned as a modular device, where more syringes can be added according to the re-

quirements of the application. The main advantages of the system are the low number of parts, which can be fabricated by Fused Deposition Modeling (FDM) or other additive manufacturing processes. It uses disposable syringes to store the material; they also serve as structural support, reducing the weight and size. The loading of the gel/hydrogel into the syringe is also simplified. As tested, it works correctly in the 3DCloner Lab printer, which operates with the Marlin firmware and RAMPS1.4/Arduino electronics. The open source firmware was modified to work with two extruders. Hence, the system was considered innovative and was patented with the process number BR 10 2017 025903 0 of the National Institute of Industrial Property (INPI-Brazil).

After 3D printing, the materials were capable of retaining the shape before the crosslinking process. Next, they were ionically crosslinked to obtain single network (SN) hydrogels. Furthermore, a two-step method that combines ionic and covalent crosslinking was performed to obtain double network (DN) hydrogels. The results reflect that the mechanical properties were significantly enhanced when an interpenetrating network is formed. In summary, the contributions presented in this thesis constitute a set of tools for the 3D extrusion-based process, from planning to the crosslinking of hydrogels.

Future works can be oriented to:

- Evaluate the behavior of other formulations and rheological modifiers.
- Print complex shapes using support materials; including thermoreversible and granular materials.
- Obtain multi-material 3D printed objects to create a properties gradient.
- Test bio-inks to fabricate scaffolds and perform *in vitro* and *in vivo* studies.
- Print cell-laden artificial tissues and substitutes.
- Use the dual extrusion printing head to print biocompatible inks and deposit cells in specific regions.

References

AALAIE, J. Rheological behavior of polyacrylamide/laponite nanoparticle suspensions in electrolyte media. **Journal of Macromolecular Science, Part B**, v. 51, n. 6, 1139–1147, 2012.

AHLFELD, T.; CIDONIO, G.; KILIAN, D.; DUIN, S.; AKKINENI, A.; DAWSON, J.; YANG, S.; LODE, A.; OREFFO, R. & GELINSKY, M. Development of a clay based bioink for 3D cell printing for skeletal application. **Biofabrication**, v. 9, n. 3, 034103, 2017.

ALLEGRO. **DMOS microstepping driver with translator and overcurrent protection**. Allegro MicroSystems, 5 2018. Rev. 6.

AUGST, A.D.; KONG, H.J. & MOONEY, D.J. Alginate hydrogels as biomaterials. **Macromolecular Bioscience**, v. 6, n. 8, 623–633, 2006.

BAKARICH, S.E.; GORKIN III, R.; IN HET PANHUIS, M. & SPINKS, G.M. Three-dimensional printing fiber reinforced hydrogel composites. **ACS Applied Materials & Interfaces**, v. 6, n. 18, 15998–16006, 2014.

BAKARICH, S.E.; PANHUIS, M.I.H.; BEIRNE, S.; WALLACE, G.G. & SPINKS, G.M. Extrusion printing of ionic–covalent entanglement hydrogels with high toughness. **Journal of Materials Chemistry B**, v. 1, n. 38, 4939–4946, 2013.

BARBUCCI, R. **Hydrogels: Biological properties and applications**. Springer Science & Business Media, 2009.

BARRY, R.A.; SHEPHERD, R.F.; HANSON, J.N.; NUZZO, R.G.; WILTZIUS, P. & LEWIS,

J.A. Direct-write assembly of 3D hydrogel scaffolds for guided cell growth. **Advanced Materials**, v. 21, n. 23, 2407–2410, 2009.

BHATTACHARJEE, T.; ZEHNDER, S.M.; ROWE, K.G.; JAIN, S.; NIXON, R.M.; SAWYER, W.G. & ANGELINI, T.E. Writing in the granular gel medium. **Science Advances**, v. 1, n. 8, e1500655, 2015.

BOERE, K.W.; BLOKZIJL, M.M.; VISSER, J.; LINSSEN, J.E.A.; MALDA, J.; HENNINK, W.E. & VERMONDEN, T. Biofabrication of reinforced 3D-scaffolds using two-component hydrogels. **Journal of Materials Chemistry B**, v. 3, n. 46, 9067–9078, 2015.

BRAUN, D.D. & ROSEN, M.R. **Rheology modifiers handbook: practical use and application**. Elsevier, 2013.

BRETAS, R.E.S. & D'ÁVILA, M.A. **Reologia de polímeros fundidos**. São Carlos, Ed UFSCAR, 2005.

CAI, W.R.; ZHANG, G.Y.; SONG, T.; ZHANG, X.J. & SHAN, D. Cobalt hexacyanoferrate electrodeposited on electrode with the assistance of laponite: The enhanced electrochemical sensing of captopril. **Electrochimica Acta**, v. 198, 32–39, 2016.

CARREAU, P.J. Rheological equations from molecular network theories. **Transactions of the Society of Rheology**, v. 16, n. 1, 99–127, 1972.

CHIA, H.N. & WU, B.M. Recent advances in 3D printing of biomaterials. **Journal of biological engineering**, v. 9, n. 1, 4, 2015.

CHUNG, J.H.; NAFICY, S.; YUE, Z.; KAPSA, R.; QUIGLEY, A.; MOULTON, S.E. & WALLACE, G.G. Bio-ink properties and printability for extrusion printing living cells. **Biomaterials Science**, v. 1, n. 7, 763–773, 2013.

COLBY, R.H. Structure and linear viscoelasticity of flexible polymer solutions: comparison of polyelectrolyte and neutral polymer solutions. **Rheologica Acta**, v. 49, n. 5, 425–442, 2010.

CONNER, B.P.; MANOGHARAN, G.P.; MARTOF, A.N.; RODOMSKY, L.M.; RODOMSKY, C.M.; JORDAN, D.C. & LIMPEROS, J.W. Making sense of 3-D printing: Creating a map of additive manufacturing products and services. **Additive Manufacturing**, v. 1, 64–76, 2014.

CROSS, M.M. Rheology of non-newtonian fluids: A new flow equation for pseudoplastic systems. **Journal of Colloid Science**, v. 20, n. 5, 417–437, 1965.

CUMMINS, H.Z. Liquid, glass, gel: The phases of colloidal laponite. **Journal of Non-Crystalline Solids**, v. 353, n. 41-43, 3891–3905, 2007.

DARNELL, M.C.; SUN, J.Y.; MEHTA, M.; JOHNSON, C.; ARANY, P.R.; SUO, Z. & MOONEY, D.J. Performance and biocompatibility of extremely tough alginate/polyacrylamide hydrogels. **Biomaterials**, v. 34, n. 33, 8042–8048, 2013.

DÁVILA, J.L. & D'ÁVILA, M.A. Laponite as a rheology modifier of alginate solutions: Physical gelation and aging evolution. **Carbohydrate Polymers**, v. 157, 1–8, 2017.

DÁVILA, J.L. & D'ÁVILA, M.A. Rheological evaluation of Laponite/alginate inks for 3D extrusion-based printing. **The International Journal of Advanced Manufacturing Technology**, Nov 2018.

DÁVILA, J.L.; FREITAS, M.S.; NETO, P.I.; SILVEIRA, Z.C.; SILVA, J.V.L. & D'ÁVILA, M.A. Software to generate 3-D continuous printing paths for the fabrication of tissue engineering scaffolds. **The International Journal of Advanced Manufacturing Technology**, v. 84, n. 5, 1671–1677, 2016.

DÁVILA, J.L.; NETO, P.I.; SILVA, J.V.L. & D'ÁVILA, M.A. Sistema modular para impressão 3D de géis. Dec 2017. BR 10 2017 025903 0.

DOU, S. & COLBY, R.H. Charge density effects in salt-free polyelectrolyte solution rheology. **Journal of Polymer Science Part B: Polymer Physics**, v. 44, n. 14, 2001–2013, 2006.

DU, J.; ZHU, J.; WU, R.; XU, S.; TAN, Y. & WANG, J. A facile approach to prepare strong poly(acrylic acid)/laponite® ionic nanocomposite hydrogels at high clay concentrations. **RSC Advances**, v. 5, n. 74, 60152–60160, 2015.

DUAN, B.; HOCKADAY, L.A.; KANG, K.H. & BUTCHER, J.T. 3D bioprinting of heterogeneous aortic valve conduits with alginate/gelatin hydrogels. **Journal of Biomedical Materials Research Part A**, v. 101, n. 5, 1255–1264, 2013.

DULLAERT, K. & MEWIS, J. A model system for thixotropy studies. **Rheologica Acta**, v. 45, n. 1, 23–32, 2005.

ECHALIER, C.; LEVATO, R.; MATEOS-TIMONEDA, M.A.; CASTANO, O.; DÉJEAN, S.; GARRIC, X.; PINESE, C.; NOËL, D.; ENGEL, E.; MARTINEZ, J. *et al.* Modular bioink for 3D printing of biocompatible hydrogels: sol–gel polymerization of hybrid peptides and polymers. **RSC Advances**, v. 7, n. 20, 12231–12235, 2017.

ERTESVåG, H. & VALLA, S. Biosynthesis and applications of alginates. **Polymer Degradation and Stability**, v. 59, n. 1-3, 85–91, 1998.

EVANS, B. **Practical 3D printers: The science and art of 3D printing**. Apress, 2012.

FARRÉS, I.F. & NORTON, I. Formation kinetics and rheology of alginate fluid gels produced by in-situ calcium release. **Food Hydrocolloids**, v. 40, 76–84, 2014.

FERNÁNDEZ, E.; LÓPEZ, D.; LÓPEZ-CABARCOS, E. & MIJANGOS, C. Viscoelastic and swelling properties of glucose oxidase loaded polyacrylamide hydrogels and the evaluation of their properties as glucose sensors. **Polymer**, v. 46, n. 7, 2211–2217, 2005.

FU, S.; THACKER, A.; SPERGER, D.M.; BONI, R.L.; BUCKNER, I.S.; VELANKAR, S.; MUNSON, E.J. & BLOCK, L.H. Relevance of rheological properties of sodium alginate in solution to calcium alginate gel properties. **AAPS PharmSciTech**, v. 12, n. 2, 453–460, 2011.

GACESA, P. Alginates. **Carbohydrate Polymers**, v. 8, n. 3, 161–182, 1988.

GHADIRI, M.; CHRZANOWSKI, W.; LEE, W.; FATHI, A.; DEHGHANI, F. & ROHANIZADEH, R. Physico-chemical, mechanical and cytotoxicity characterizations of Laponite®/alginate nanocomposite. **Applied Clay Science**, v. 85, 64–73, 2013a.

GHADIRI, M.; HAU, H.; CHRZANOWSKI, W.; AGUS, H. & ROHANIZADEH, R. Laponite clay as a carrier for in situ delivery of tetracycline. **RSC Advances**, v. 3, n. 43, 20193–20201, 2013b.

GLASS, J.E.; SCHULZ, D.N. & ZUKOSKI, C. Polymers as rheology modifiers: an overview. ACS Publications, 1991.

GORRET, N.; RENARD, C.; FAMELART, M.; MAUBOIS, J. & DOUBLIER, J. Rheological characterization of the EPS produced by P. acidi-propionici on milk microfiltrate. **Carbohydrate Polymers**, v. 51, n. 2, 149–158, 2003.

GULREZ, S.K.; AL-ASSAF, S. & PHILLIPS, G.O. Hydrogels: methods of preparation, characterisation and applications. In **Progress in molecular and environmental bioengineering-from analysis and modeling to technology applications**. InTech, 2011.

GUPTA, P.; VERMANI, K. & GARG, S. Hydrogels: from controlled release to pH-responsive drug delivery. **Drug discovery today**, v. 7, n. 10, 569–579, 2002.

GUVENDIREN, M.; LU, H.D. & BURDICK, J.A. Shear-thinning hydrogels for biomedical applications. **Soft matter**, v. 8, n. 2, 260–272, 2012.

HABIB, A.; SATHISH, V.; MALLIK, S. & KHODA, B. 3D printability of alginate-carboxymethyl cellulose hydrogel. **Materials**, v. 11, n. 3, 454, 2018.

HABIBI, Y.; LUCIA, L.A. & ROJAS, O.J. Cellulose nanocrystals: chemistry, self-assembly, and applications. **Chemical reviews**, v. 110, n. 6, 3479–3500, 2010.

HE, Y.; YANG, F.; ZHAO, H.; GAO, Q.; XIA, B. & FU, J. Research on the printability of hydrogels in 3D bioprinting. **Scientific Reports**, v. 6, 29977, 2016.

HIGHLEY, C.B.; RODELL, C.B. & BURDICK, J.A. Direct 3d printing of shear-thinning hydrogels into self-healing hydrogels. **Advanced Materials**, v. 27, n. 34, 5075–5079, 2015.

HINTON, T.J.; JALLERAT, Q.; PALCHESKO, R.N.; PARK, J.H.; GRODZICKI, M.S.; SHUE, H.J.; RAMADAN, M.H.; HUDSON, A.R. & FEINBERG, A.W. Three-dimensional printing of complex biological structures by freeform reversible embedding of suspended hydrogels. **Science Advances**, v. 1, n. 9, e1500758, 2015.

HOFFMAN, A.S. Hydrogels for biomedical applications. **Advanced drug delivery reviews**, v. 64, 18–23, 2012.

HONG, S.; SYCKS, D.; CHAN, H.F.; LIN, S.; LOPEZ, G.P.; GUILAK, F.; LEONG, K.W. & ZHAO, X. 3D printing of highly stretchable and tough hydrogels into complex, cellularized structures. **Advanced Materials**, v. 27, n. 27, 4035–4040, 2015.

JATAV, S. & JOSHI, Y.M. Rheological signatures of gelation and effect of shear melting on aging colloidal suspension. **Journal of Rheology**, v. 58, n. 5, 1535–1554, 2014.

JOSHI, Y.M.; REDDY, G.R.K.; KULKARNI, A.L.; KUMAR, N. & CHHABRA, R.P. Rheological behaviour of aqueous suspensions of laponite: New insights into the ageing phenomena. In **Proceedings of the Royal Society of London A: Mathematical, Physical and Engineering Sciences**, v. 464, pp. 469–489. The Royal Society, 2008.

JUN, C.S.; SIM, B. & CHOI, H.J. Fabrication of electric-stimuli responsive polyaniline/laponite composite and its viscoelastic and dielectric characteristics. **Colloids and Surfaces A: Physicochemical and Engineering Aspects**, v. 482, 670–677, 2015.

KAASTRUP, K. & SIKES, H. Using photo-initiated polymerization reactions to detect molecular recognition. **Chemical Society Reviews**, v. 45, n. 3, 532–545, 2016.

KANTI, P.; SRIGOWRI, K.; MADHURI, J.; SMITHA, B. & SRIDHAR, S. Dehydration of ethanol through blend membranes of chitosan and sodium alginate by pervaporation. **Separation and Purification Technology**, v. 40, n. 3, 259–266, 2004.

KIRCHMAJER, D.M.; GORKIN III, R. *et al.* An overview of the suitability of hydrogel-forming polymers for extrusion-based 3D-printing. **Journal of Materials Chemistry B**, v. 3, n. 20, 4105–4117, 2015.

KUMAR, S.; ASWAL, V.K. & HARIKRISHNAN, G. Polymer concentration regulated aging in aqueous laponite suspensions. **Rheologica Acta**, v. 55, n. 5, 411–421, 2016.

KUO, C.K. & MA, P.X. Ionically crosslinked alginate hydrogels as scaffolds for tissue engineering: Part 1. structure, gelation rate and mechanical properties. **Biomaterials**, v. 22, n. 6, 511–521, 2001.

LABANDA, J. & LLORENS, J. Effect of aging time on the rheology of laponite dispersions. **Colloids and Surfaces A: Physicochemical and Engineering Aspects**, v. 329, n. 1, 1–6, 2008.

LARSEN, B.E.; BJøRNSTAD, J.; PETTERSEN, E.O.; TøNNESEN, H.H. & MELVIK, J.E. Rheological characterization of an injectable alginate gel system. **BMC biotechnology**, v. 15, n. 1, 1, 2015.

LEWIS, J.A. & GRATSON, G.M. Direct writing in three dimensions. **Materials today**, v. 7, n. 7-8, 32–39, 2004.

LI, P.; DAI, Y.N.; ZHANG, J.P.; WANG, A.Q. & WEI, Q. Chitosan-alginate nanoparticles as a novel drug delivery system for nifedipine. **International Journal of Biomedical Science: IJBS**, v. 4, n. 3, 221, 2008a.

LI, P.; SIDDARAMAIAH; KIM, N.H.; HEO, S.B. & LEE, J.H. Novel PAAM/laponite clay nanocomposite hydrogels with improved cationic dye adsorption behavior. **Composites Part B: Engineering**, v. 39, n. 5, 756–763, 2008b.

LI, Z.; HE, G.; HUA, J.; WU, M.; GUO, W.; GONG, J.; ZHANG, J. & QIAO, C. Preparation of γ-PGA hydrogels and swelling behaviors in salt solutions with different ionic valence numbers. **RSC Advances**, v. 7, n. 18, 11085–11093, 2017.

LIM, B.C.; SINGU, B.S.; HONG, S.E.; NA, Y.H. & YOON, K.R. Synthesis and characterization nanocomposite of polyacrylamide-rGO-Ag-PEDOT/PSS hydrogels by photo polymerization method. **Polymers for Advanced Technologies**, v. 27, n. 3, 366–373, 2016.

LIU, D.; CHEN, X.; YUE, Y.; CHEN, M. & WU, Q. Structure and rheology of nanocrystalline cellulose. **Carbohydrate Polymers**, v. 84, n. 1, 316–322, 2011.

LIU, S.; LI, H.; TANG, B.; BI, S. & LI, L. Scaling law and microstructure of alginate hydrogel. **Carbohydrate Polymers**, v. 135, 101–109, 2016.

LIU, X. & BHATIA, S.R. Laponite® and laponite®-PEO hydrogels with enhanced elasticity in phosphate-buffered saline. **Polymers for Advanced Technologies**, v. 26, n. 7, 874–879, 2015.

LIU, X.; QIAN, L.; SHU, T. & TONG, Z. Rheology characterization of sol–gel transition in aqueous alginate solutions induced by calcium cations through in situ release. **Polymer**, v. 44, n. 2, 407–412, 2003.

LU, P.J. & WEITZ, D.A. Colloidal particles: crystals, glasses, and gels. **Annu. Rev. Condens. Matter Phys.**, v. 4, n. 1, 217–233, 2013.

MACOSKO, C.W. **Rheology: principles, measurements, and applications**. Wiley-VCH, 1994.

MAHMOODI, N.M. Magnetic ferrite nanoparticle–alginate composite: Synthesis, characterization and binary system dye removal. **Journal of the Taiwan Institute of Chemical Engineers**, v. 44, n. 2, 322–330, 2013.

MALDA, J.; VISSER, J.; MELCHELS, F.P.; JÜNGST, T.; HENNINK, W.E.; DHERT, W.J.; GROLL, J. & HUTMACHER, D.W. 25th anniversary article: engineering hydrogels for biofabrication. **Advanced Materials**, v. 25, n. 36, 5011–5028, 2013.

MALONE, E. & LIPSON, H. Fab@home: the personal desktop fabricator kit. **Rapid Prototyping Journal**, v. 13, n. 4, 245–255, 2007.

MARKSTEDT, K.; MANTAS, A.; TOURNIER, I.; MARTIÍNEZ ÁVILA, H.; HÄGG, D. & GATENHOLM, P. 3D bioprinting human chondrocytes with nanocellulose–alginate bioink for cartilage tissue engineering applications. **Biomacromolecules**, v. 16, n. 5, 1489–1496, 2015.

MEWIS, J. & WAGNER, N.J. **Colloidal suspension rheology**. Cambridge University Press, 2012.

MEZGER, T.G. **The rheology handbook: for users of rotational and oscillatory rheometers**. Vincentz Network GmbH & Co KG, 2006.

MISCHKE, C.R. & SHIGLEY, J.E. **Standard handbook of machine design**. McGraw-Hill, 1996.

MONGONDRY, P.; TASSIN, J.F. & NICOLAI, T. Revised state diagram of laponite dispersions. **Journal of Colloid and Interface Science**, v. 283, n. 2, 397–405, 2005.

MORARIU, S.; BERCEA, M. & SACARESCU, L. Tailoring of clay/poly (ethylene oxide) hy-

drogel properties by chitosan incorporation. **Industrial & Engineering Chemistry Research**, v. 53, n. 35, 13690–13698, 2014.

MORRISON, F.A. **Understanding rheology**. Oxford University Press, 2001.

MUELLER, B. Additive manufacturing technologies–rapid prototyping to direct digital manufacturing. **Assembly Automation**, v. 32, n. 2, 2012.

MURPHY, R.; WALSH, D.P.; HAMILTON, C.A.; CRYAN, S.A.; IN HET PANHUIS, M. & HEISE, A. Degradable 3D-printed hydrogels based on star-shaped copolypeptides. **Biomacromolecules**, 2018.

NONOYAMA, T. & GONG, J.P. Double-network hydrogel and its potential biomedical application: A review. **Proceedings of the Institution of Mechanical Engineers, Part H: Journal of Engineering in Medicine**, v. 229, n. 12, 853–863, 2015.

OUYANG, L.; HIGHLEY, C.B.; RODELL, C.B.; SUN, W. & BURDICK, J.A. 3D printing of shear-thinning hyaluronic acid hydrogels with secondary cross-linking. **ACS Biomaterials Science & Engineering**, v. 2, n. 10, 1743–1751, 2016.

ÖZKAN, M.; HASHMI, S.G.; HALME, J.; KARAKOÇ, A.; SARIKKA, T.; PALTAKARI, J. & LUND, P.D. Inkjet-printed platinum counter electrodes for dye-sensitized solar cells. **Organic Electronics**, v. 44, 159–167, 2017.

PAPAJOVÁ, E.; BUJDOŠ, M.; CHORVÁT, D.; STACH, M. & LACíK, I. Method for preparation of planar alginate hydrogels by external gelling using an aerosol of gelling solution. **Carbohydrate Polymers**, v. 90, n. 1, 472–482, 2012.

PAXTON, N.; SMOLAN, W.; BÖCK, T.; MELCHELS, F.; GROLL, J. & JUNGST, T. Proposal to assess printability of bioinks for extrusion-based bioprinting and evaluation of rheological properties governing bioprintability. **Biofabrication**, v. 9, n. 4, 044107, 2017.

PAYET, L.; PONTON, A.; GROSSIORD, J.L. & AGNELY, F. Structural and rheological properties of chitosan semi-interpenetrated networks. **The European Physical Journal E**, v. 32, n. 2, 109–118, 2010.

PEAK, C.W.; STEIN, J.; GOLD, K.A. & GAHARWAR, A.K. Nanoengineered colloidal inks for 3D bioprinting. **Langmuir**, v. 34, n. 3, 917–925, 2017.

PEPPAS, N.A. **Biomedical applications of hydrogels handbook**. Springer Science & Business Media, 2010.

PERCIVAL, E. The polysaccharides of green, red and brown seaweeds: their basic structure, biosynthesis and function. **British Phycological Journal**, v. 14, n. 2, 103–117, 1979.

PERKINS, R.; BRACE, R. & MATIJEVIĆ, E. Colloid and surface properties of clay suspensions. I. laponite cp. **Journal of Colloid and Interface Science**, v. 48, n. 3, 417–426, 1974.

RADHAKRISHNAN, J.; SUBRAMANIAN, A.; KRISHNAN, U.M. & SETHURAMAN, S. Injectable and 3D bioprinted polysaccharide hydrogels: from cartilage to osteochondral tissue engineering. **Biomacromolecules**, v. 18, n. 1, 1–26, 2016.

REZENDE, R.A.; BÁRTOLO, P.J.; MENDES, A. & MACIEL FILHO, R. Rheological behavior of alginate solutions for biomanufacturing. **Journal of Applied Polymer Science**, v. 113, n. 6, 3866–3871, 2009.

RODRíGUEZ-RIVERO, C.; HILLIOU, L.; DEL VALLE, E.M.M. & GALÁN, M.A. Rheological characterization of commercial highly viscous alginate solutions in shear and extensional flows. **Rheologica Acta**, v. 53, n. 7, 559–570, 2014.

ROGER, S.; SANG, Y.Y.C.; BEE, A.; PERZYNSKI, R.; DI MEGLIO, J.M. & PONTON, A. Structural and multi-scale rheophysical investigation of diphasic magneto-sensitive materials based on biopolymers. **The European Physical Journal E**, v. 38, n. 8, 1–13, 2015.

RUSSO, R.; MALINCONICO, M. & SANTAGATA, G. Effect of cross-linking with calcium ions on the physical properties of alginate films. **Biomacromolecules**, v. 8, n. 10, 3193–3197, 2007.

RUZICKA, B. & ZACCARELLI, E. A fresh look at the laponite phase diagram. **Soft Matter**, v. 7, n. 4, 1268–1286, 2011.

SCHMIEG, B.; SCHIMEK, A. & FRANZREB, M. Development and performance of a 3D-printable poly (ethylene glycol) diacrylate hydrogel suitable for enzyme entrapment and long-term biocatalytic applications. **Engineering in Life Sciences**, v. 18, n. 9, 659–667, 2018.

SCHUURMAN, W.; LEVETT, P.A.; POT, M.W.; VAN WEEREN, P.R.; DHERT, W.J.; HUTMACHER, D.W.; MELCHELS, F.P.; KLEIN, T.J. & MALDA, J. Gelatin-methacrylamide hydrogels as potential biomaterials for fabrication of tissue-engineered cartilage constructs. **Macromolecular bioscience**, v. 13, n. 5, 551–561, 2013.

SELEN, F.; CAN, V. & TEMEL, G. Preparation of photodegradable polyacrylamide hydrogels via micellar copolymerization and determination of their phototunable elasticity and swelling behaviors. **RSC Advances**, v. 6, n. 38, 31692–31697, 2016.

SEMWAL, V.; SHRIVASTAV, A.M.; VERMA, R. & GUPTA, B.D. Surface plasmon resonance based fiber optic ethanol sensor using layers of silver/silicon/hydrogel entrapped with ADH/-NAD. **Sensors and Actuators B: Chemical**, v. 230, 485–492, 2016.

SHAHIN, A. & JOSHI, Y.M. Irreversible aging dynamics and generic phase behavior of aqueous suspensions of laponite. **Langmuir**, v. 26, n. 6, 4219–4225, 2010.

SHEN, M.; LI, L.; SUN, Y.; XU, J.; GUO, X. & PRUD'HOMME, R.K. Rheology and adhesion of poly(acrylic acid)/laponite nanocomposite hydrogels as biocompatible adhesives. **Langmuir**, v. 30, n. 6, 1636–1642, 2014.

SHIMOJO, A.A.M.; PIRES, A.M.B.; LICHY, R.; RODRIGUES, A.A. & SANTANA, M.H.A. The crosslinking degree controls the mechanical, rheological, and swelling properties of hyaluronic acid microparticles. **Journal of Biomedical Materials Research Part A**, v. 103, n. 2, 730–737, 2015.

SHIN, H.; OLSEN, B.D. & KHADEMHOSSEINI, A. The mechanical properties and cytotoxicity of cell-laden double-network hydrogels based on photocrosslinkable gelatin and gellan gum biomacromolecules. **Biomaterials**, v. 33, n. 11, 3143–3152, 2012.

SHIN, S.; PARK, S.; PARK, M.; JEONG, E.; NA, K.; YOUN, H.J. & HYUN, J. Cellulose nanofibers for the enhancement of printability of low viscosity gelatin derivatives. **BioResources**, v. 12, n. 2, 2941–2954, 2017.

SIQUEIRA, G.; KOKKINIS, D.; LIBANORI, R.; HAUSMANN, M.K.; GLADMAN, A.S.; NEELS, A.; TINGAUT, P.; ZIMMERMANN, T.; LEWIS, J.A. & STUDART, A.R. Cellulose nanocrystal inks for 3D printing of textured cellular architectures. **Advanced Functional Materials**, v. 27, n. 12, 2017.

ŞOLPAN, D.; TORUN, M. & GÜVEN, O. The usability of (sodium alginate/acrylamide) semi-interpenetrating polymer networks on removal of some textile dyes. **Journal of Applied Polymer Science**, v. 108, n. 6, 3787–3795, 2008.

SUDHA, J.D.; PICH, A.; REENA, V.L.; SIVAKALA, S. & ADLER, H.J.P. Water-dispersible multifunctional polyaniline-laponite-keggin iron nanocomposites through a template approach. **Journal of Materials Chemistry**, v. 21, n. 41, 16642–16650, 2011.

SUN, W.; WANG, T.; WANG, C.; LIU, X. & TONG, Z. Scaling of the dynamic response of hectorite clay suspensions containing poly (ethylene glycol) along the universal route of aging. **Soft Matter**, v. 9, n. 27, 6263–6269, 2013.

SUN, W.; YANG, Y.; WANG, T.; HUANG, H.; LIU, X. & TONG, Z. Effect of adsorbed poly (ethylene glycol) on the gelation evolution of laponite suspensions: Aging time-polymer

concentration superposition. **Journal of Colloid and Interface Science**, v. 376, n. 1, 76–82, 2012.

TAWARI, S.L.; KOCH, D.L. & COHEN, C. Electrical double-layer effects on the brownian diffusivity and aggregation rate of laponite clay particles. **Journal of Colloid and Interface Science**, v. 240, n. 1, 54–66, 2001.

THOMPSON, D.W. & BUTTERWORTH, J.T. The nature of laponite and its aqueous dispersions. **Journal of Colloid and Interface Science**, v. 151, n. 1, 236–243, 1992.

THU, B.; BRUHEIM, P.; ESPEVIK, T.; SMIDSRøD, O.; SOON-SHIONG, P. & SKJåK-BRæK, G. Alginate polycation microcapsules: I. interaction between alginate and polycation. **Biomaterials**, v. 17, n. 10, 1031–1040, 1996.

ULLAH, F.; OTHMAN, M.B.H.; JAVED, F.; AHMAD, Z. & AKIL, H.M. Classification, processing and application of hydrogels: A review. **Materials Science and Engineering: C**, v. 57, 414–433, 2015.

ISO/ASTM 52900. Additive manufacturing-General principles-terminology. Standard, International Organization for Standardization/ American Society for Testing and Materials, 2015.

VENKATESAN, J.; BHATNAGAR, I.; MANIVASAGAN, P.; KANG, K.H. & KIM, S.K. Alginate composites for bone tissue engineering: a review. **International journal of Biological Macromolecules**, v. 72, 269–281, 2015.

VOO, W.P.; LEE, B.B.; IDRIS, A.; ISLAM, A.; TEY, B.T. & CHAN, E.S. Production of ultra-high concentration calcium alginate beads with prolonged dissolution profile. **RSC Advances**, v. 5, n. 46, 36687–36695, 2015.

WIJNEN, B.; ANZALONE, G.C.; HASELHUHN, A.S.; SANDERS, P.G. & PEARCE, J.M. Free and open-source control software for 3-D motion and processing. **Journal of Open Rese-**

arch Software, v. 4, n. 1, 2016.

WILLENBACHER, N. Unusual thixotropic properties of aqueous dispersions of laponite RD. **Journal of Colloid and Interface Science**, v. 182, n. 2, 501–510, 1996.

WINTER, H.H. & CHAMBON, F. Analysis of linear viscoelasticity of a crosslinking polymer at the gel point. **Journal of Rheology**, v. 30, n. 2, 367–382, 1986.

XAVIER, J.R.; THAKUR, T.; DESAI, P.; JAISWAL, M.K.; SEARS, N.; COSGRIFF-HERNANDEZ, E.; KAUNAS, R. & GAHARWAR, A.K. Bioactive nanoengineered hydrogels for bone tissue engineering: a growth-factor-free approach. **ACS Nano**, v. 9, n. 3, 3109–3118, 2015.

YANG, C.H.; WANG, M.X.; HAIDER, H.; YANG, J.H.; SUN, J.Y.; CHEN, Y.M.; ZHOU, J. & SUO, Z. Strengthening alginate/polyacrylamide hydrogels using various multivalent cations. **ACS Applied Aaterials & Interfaces**, v. 5, n. 21, 10418–10422, 2013.

YANG, F.; TADEPALLI, V. & WILEY, B.J. 3D printing of a double network hydrogel with a compression strength and elastic modulus greater than those of cartilage. **ACS Biomaterials Science & Engineering**, v. 3, n. 5, 863–869, 2017.

YASUDA, K.; ARMSTRONG, R. & COHEN, R. Shear flow properties of concentrated solutions of linear and star branched polystyrenes. **Rheologica Acta**, v. 20, n. 2, 163–178, 1981.

YU, F.; ZHANG, F.; LUAN, T.; ZHANG, Z. & ZHANG, H. Rheological studies of hyaluronan solutions based on the scaling law and constitutive models. **Polymer**, v. 55, n. 1, 295–301, 2014.

ZHANG, H.; ZHAI, D. & HE, Y. Graphene oxide/polyacrylamide/carboxymethyl cellulose sodium nanocomposite hydrogel with enhanced mechanical strength: preparation, characterization and the swelling behavior. **RSC Advances**, v. 4, n. 84, 44600–44609, 2014.

ZHAO, X. Multi-scale multi-mechanism design of tough hydrogels: building dissipation into stretchy networks. **Soft Matter**, v. 10, n. 5, 672–687, 2014.

ZILBERMAN, M. **Active implants and scaffolds for tissue regeneration**. Springer, 2011.

ZULIAN, L.; RUZICKA, B. & RUOCCO, G. Influence of an adsorbing polymer on the aging dynamics of laponite clay suspensions. **Philosophical Magazine**, v. 88, n. 33-35, 4213–4221, 2008.

ANNEX A – List of publications

Articles:

DÁVILA, J.L. & D'ÁVILA, M.A. Laponite as a rheology modifier of alginate solutions: Physical gelation and aging evolution. **Carbohydrate Polymers**, v. 157, 1–8, 2017.

DÁVILA, J.L. & D'ÁVILA, M.A. Rheological evaluation of Laponite/alginate inks for 3D extrusion-based printing. **The International Journal of Advanced Manufacturing Technology**, Nov 2018.

Patent:

DÁVILA, J.L.; NETO, P.I.; SILVA, J.V.L. & D'ÁVILA, M.A. Sistema modular para impressão 3D de géis. Dec 2017. BR 10 2017 025903 0.

Abstracts, posters, and oral presentations:

DÁVILA, J.L.; MANZINI, B.M.; DUARTE, A.S.S.; LUZO, A.C.M. & D'ÁVILA, M.A. 3D Extrusion-based printing of Laponite/alginate-PAAm hydrogels. **XVII Brazilian MRS Meeting**, Natal-Brazil, 2018, poster.

DÁVILA, J.L.; NETO, P.I.; SILVA, J.V.L. & D'ÁVILA, M.A. Modular system for 3D extrusion-based printing of gels and hydrogels. **XVII Brazilian MRS Meeting**, Natal-Brazil, 2018, poster.

DÁVILA, J.L. & D'ÁVILA, M.A. Rheological characterization of Laponite/alginate inks for additive manufacturing applications. **International Conference on Biofabrication**, Beijing-China, 2017, oral presentation.

DÁVILA, J.L. & D'ÁVILA, M.A. Rheological characterization of Laponite/alginate inks for

additive manufacturing applications. 14^{th} **Brazilian Polymer Conference**, Águas de Lindóia-Brazil, 2017, oral presentation.

DÁVILA, J.L. & D'ÁVILA, M.A. Laponite/alginate inks for additive manufacturing. **Frontiers in Polymer Science**, Seville-Spain, 2017, poster.

DÁVILA, J.L. & D'ÁVILA, M.A. Three dimensional printing of Laponite/alginate hydrogels. **XVI Brazilian MRS Meeting**, Gramado-Brazil, 2017, poster.

APPENDIX A – Aging curves

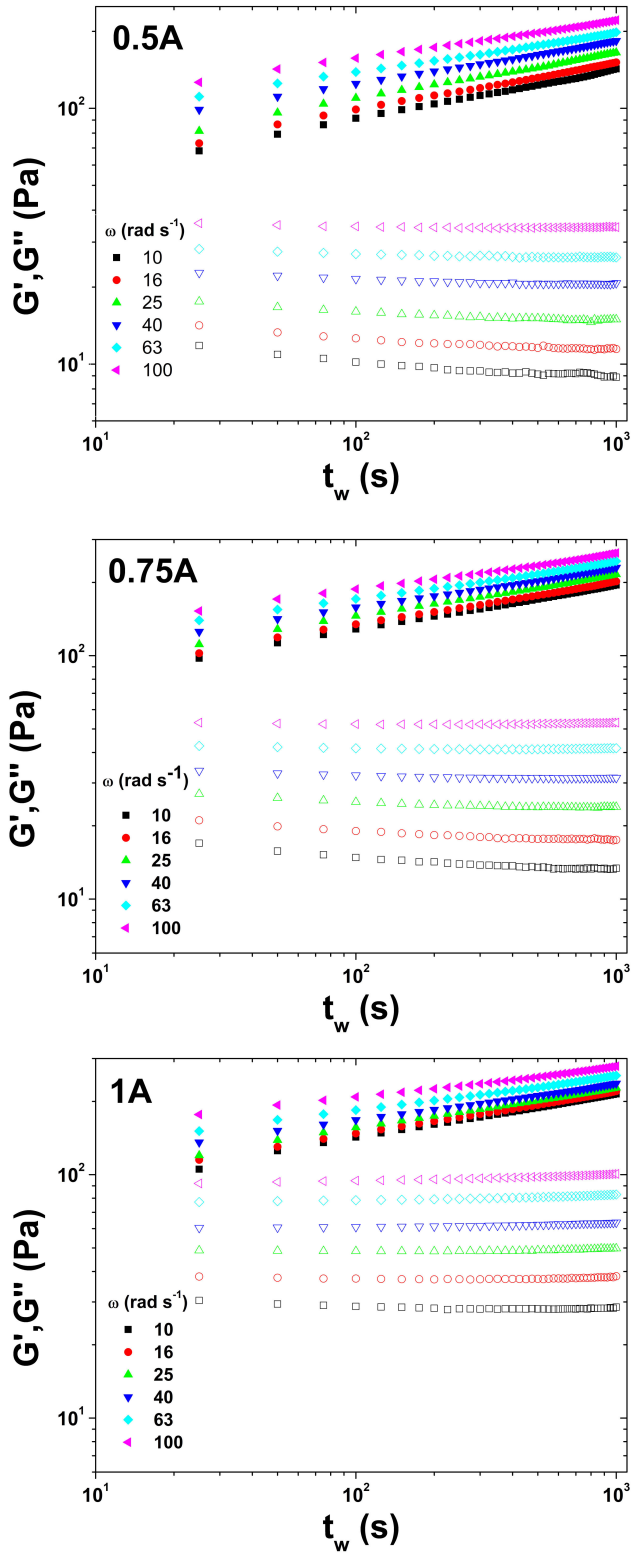

Fig. A.1: Aging evolution: dependence of G' (solid symbols) and G'' (open symbols) on the waiting time (t_w) for frequencies in the range of 10 to 100 $rad\ s^{-1}$ for the compositions 0.5, 0.75 and 1 wt.$\%$ alginate and 2 wt.$\%$ Laponite.

APPENDIX B – Printing head extrusion force

The extrusion force was obtained using a TA.XTplus Texture Analyser with a $500\ N$ load cell. Piston speeds of 0.526, 1.052 and $1.578\ mm\ min^{-1}$ were tested using a disposable syringe of $20\ ml$ and a 22G nozzle tip of $25\ mm$ in length. These latter were purchased from Injex, Brazil. All tests were triplicated using the optimal ink concentration. In Fig. B.1 are observed the obtained results.

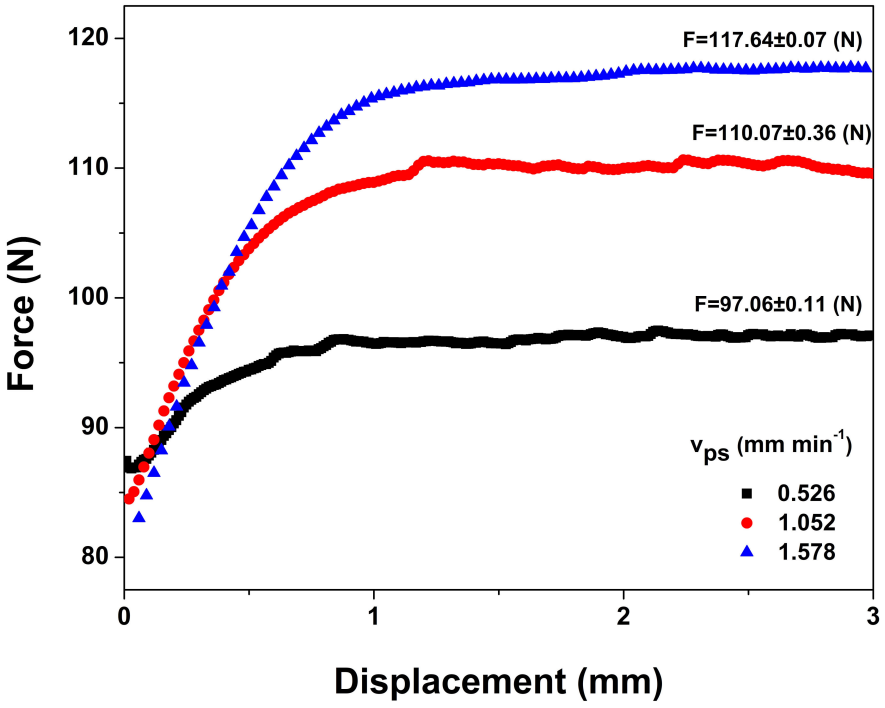

Fig. B.1: Extrusion force for different piston speeds (v_{ps}).

Then, for the printing head design, the linear actuator was selected taking into account its maximum load force, which was calculated using the power screw equations (Mischke & Shigley, 1996):

$$F = \frac{2T_R}{d_m}\left(\frac{\pi d_m \beta - \mu_t L_T}{\pi \mu_t d_m + L_T \beta}\right) \tag{B.1a}$$

$$d_m = d - \frac{p}{2} \tag{B.1b}$$

$$L_T = p\ n_s \tag{B.1c}$$

$$tan\left(\lambda_L\right) = \frac{L_T}{\pi d_m} \tag{B.1d}$$

$$tan\left(\alpha_m\right) = tan\left(\alpha_F\right) cos\left(\lambda_L\right) \tag{B.1e}$$

$$\beta = cos\left(\alpha_m\right) \tag{B.1f}$$

where T_R is the raising torque, d_m and d the mean and the nominal diameters of the threaded shaft respectively, L_T the thread lead, p the thread pitch, n_s the number of thread starts, λ_L the lead angle, α_F and α_m the flank and the normalized flank angles respectively, β the thread geometry parameter, and μ_t the coefficient of thread friction. The data from the linear actuator and its threaded shaft is shown below:

$$T_R = 0.21\ N\,m \quad d = 5\ mm \quad n_s = 2 \quad p = 1\ mm \quad \alpha_F = 4.046° \quad \mu_t = 0.16,$$

then, the maximum load force is:

$$F = 302.2\ N,$$

which ensures that the material can be extruded through the nozzle tip.